2016

Polymer based microscale and nanoscale technologies for optical and biomedical application

Rabin Dhakal
Iowa State University

Polymer based microscale and nanoscale technologies for optical and biomedical application

by

Rabin Dhakal

A dissertation submitted to the graduate faculty

in partial fulfillment of the requirements for the degree of

DOCTOR OF PHILOSOPHY

Major: Electrical Engineering

Program of Study Committee:
Jaeyoun Kim, Major Professor
Rana Biswas
Liang Dong
Meng Lu
Jiming Song

Iowa State University

Ames, Iowa

2016

DEDICATION

To my family,

Thank you for the support, patience and encouragement in this long journey of doctoral study

TABLE OF CONTENTS

ACKNOWLEDGMENTS

First, I would like to express my deepest gratitude to my major professor, Dr. Jaeyoun Kim for his invaluable guidance and constructive feedback through out the course of this research. His exceptional expertise, brilliant insight and advice kept me guided in the right direction during my PhD degree. He patiently taught me the skills to identify the key challenges in the problems we took and showed me direction to solve them. I especially would like to appreciate the way he gave me great freedom while solving my research challenges. I greatly appreciate our collaborator and my committee member Dr. Rana Biswas for wonderful mentorship. I enjoyed and learned a lot form the weekly joint meeting sessions we had for the last two years of my study. I was especially motivated by his brilliance and enthusiasm on the research subject. Similarly I would like to thank my committee members, Dr. Liang Dong, Dr. Meng Lu and Dr. Jiming Song for their guidance and support throughout the course of this research.

In addition, I would also like to thank my collaborator and lab mate Akshit Peer for the help in joint projects we did in patterning biopolymers and drug delivery and for the insightful discussions we often had regarding the projects or even science in general. Similarly, I want to express my gratitude to our previous lab mates at plasmonics and micro-photonics lab Yifen Liu, Jewon Lee and Jungwook Paek for teaching me various techniques and equipment use in our lab. My sincere Thanks to Ann Perera and Lucas Showman for their help in HPLC systems, Warren Straszheim for his help in SEM and Eeshita Manna and Qiang Li for their help in AFM measurements.

Last but not the least I want to thank my wife Sanju Timilsina for the support she gave me in this long journey. I really appreciate my mother in law Indira Timalsena for helping to take great care of our newborn daughter Annapurna and made our life easier in the final year of my study. I would also like to thank my parents Tek Nath Dhakal and Binita Dhakal for their never-ending support, love and encouragement throughout my life.

ABSTRACT

Polymer based micro and nano systems has emerged as a mainstream research in recent times with advent of bio-inspired design of opto-MEMS as wells as bio-MEMS. Polymers have wide range of material characteristics ranging for elastic to brittle nature, optically transparent as well as biocompatible and biodegradable and therefore finds various applications in optics and biomedicine. I tackled four different technological challenges in this research work using novel biomimetic design and biopolymers as listed below.

First, I designed wide acceptance angle thin and flat miniaturized solar concentrator by mimicking the wide acceptance angle found in compound eye of insects. I integrated microlens, conic spacer and lightguide to concentrate and redirect sunlight into small area where PV cells can be installed. My design can have total concentration of up to ~40 for acceptance angle of 15°.

Second, I designed and fabricated automated light control switch using opto-thermo MEMS. I used IR part of solar spectrum to change the volume of paraffin inside micro-chamber and actuate the cantilever switch. The switch when activated frustrates the TIR guided light in the lightguide and controls the illumination level. I obtained rms value of illumination change to be 0.012 for input change of 0.018.

Third, I developed rapid, inexpensive, reproducible method to make nanoscale patterns in PLLA films using replica-molding techniques. I produced very high fidelity replication of PLLA using double replication from master polycarbonate to PDMS mold and from PDMS mold to PLLA film by drop casting process. The surface characteristics of the nano-patterned film changed drastically form hydrophilic to hydrophobic due to patterning. I

also investigated the drug coating process in this film for its use in controlled drug release platform.

Finally, I used the drug coated and nano-patterned PLLA film for its potential application in biodegradable coronary stents. I fabricated the stents by rolling the PLLA films into the tubular form. The controlled drug release was studied by releasing the control and patterned PLLA surface into phosphate buffer saline. I used advanced high performance liquid chromatography coupled with mass spectrometer to measure the amount of drug released as a function of time. The nano-patterned surface has up to 20% slower drug release rate in comparison to the flat surface.

CHAPTER 1

INTRODUCTION

Background

One of the most pivotal discoveries that brought revolution in electrical engineering is the invention of transistor in 1947 at Bell labs, which quickly ensued rapid boom in development of microelectronics. Soon microelectronics research spun off to countless new technologies and changes the way we engineer solutions to the problems faced my mankind. Micro technology such as micro-electro-mechanical-system (MEMS) is a technology primarily developed based on microelectronics devices.

The early development of MEMS technology starts with the discovery of piezoelectric effect in Silicon, which leads to development of micro-sized strain gauge [1]. Soon after this, Richard Feynman challenged the scientific community to explore the realm of miniaturization in his famous talk to American Physical Society in 1959 “There’s plenty of room at the Bottom” [2]. This vision to manipulate and control things on a small scale continues to be source of inspiration in the field of micro and nano technology and some remarkable MEMS processes and products have been developed. In 1964, Harvert Nathanson from Westinghouse made resonant gate transistor as the earliest demonstration of micro electrostatic actuator using surface micromachining techniques [3]. The development of bulk micromachining by anisotropic etching of silicon in 1970’s leads to development of diaphragm pressure sensor by Kurt Peterson from IBM research [4] and inkjet nozzle by HP [5]. By 1980s Karlsruhe Nuclear Research Center in Germany developed LIGA process [6] and Toshiba Research and Development Center in Japan develops silicon wafer direct bonding method [7] beginning the era of manufacturing

high aspect ratio microstructures. This led to invention of atomic force microscope (AFM) in 1986 at IBM, rotary electrostatic side drive motors in 1988 at UC Berkley followed by lateral comb drive in 1989 at Sandia National Lab. Soon, first commercial surface micro-machined accelerometer was produced by Analog Devices.

Micro-opto-electro-mechanical system starts to appear by 1990s with development of deformable grating light modulator by Solgaard in 1992 [8], first digital mirror display (DMD) based on digital light process was demonstrated by Texas Instruments in 1994 and optical network switch by Lucent in 1999 [9]. Scientists start to combine MEMS with emerging biotechnology from early 2000s with potential application in drug delivery system, insulin pumps, lab-on-a-chip (LOC) and microfluidics. Since then, there is enormous research interests in opto and bio MEMS in academia and industry.

Research Motivations

Microfabrication in early days was performed mostly on silicon substrate due to well-established semiconductor industry. Increasing share of novel sensor and actuator systems for new optical and biomedical application requires material properties other than silicon and/or metals. Recently polymers have emerged as the materials of choice for microfabrication because advances in organic chemistry and fabrication technology. Polymers have several desirable properties for opto and bio engineering applications. For example, many polymers are optically transparent, they have low mass density compared to silicon and they have wide range of mechanical properties from brittle to elastic. In addition to this some polymers are biocompatible and biodegradable, they exhibit chemical/biological inertness and polymer surface can be readily functionalized to modify the surface properties making them suitable for biomedical applications

[10]. Further, polymers can be used in mass replication technology by soft lithography methods including hot embossing, replica molding, transfer molding and casting to produce micro-scale and nano-scale platform structures. Several different polymers with specific properties are available to make different microstructures. For example, polyethylene (PE) and polypropylene (PP) are used in various tubing and joint replacement, polytetrafluroethylene (PTFE) in vascular graft, polydimethylsiloxane (PDMS) and poly lactic acid (PLA) for various implants and templates in MEMS and bio systems.

Biomimetic MEMS design

Scientists and engineers have often been fascinated by the nature for its optimal way of evolutionary development and often take them as an inspiration in engineering solution to problems [11]. For example, researchers have developed dry adhesive nanostructures my mimicking Gecko's foot [12, 13] and super hydrophobic structures by mimicking the lotus leaf [14, 15] as shown in Fig. 1.1 (a) and (b) respectively. Also, biomimetic sensors quickly gained lot of attentions due to surge of integrated sensors in consumer electronics and other high tech devices. Figure 1.2 from Strible *et al.'s* 2009 paper [16] enumerates the summary of the biological systems imitated in sensing application.

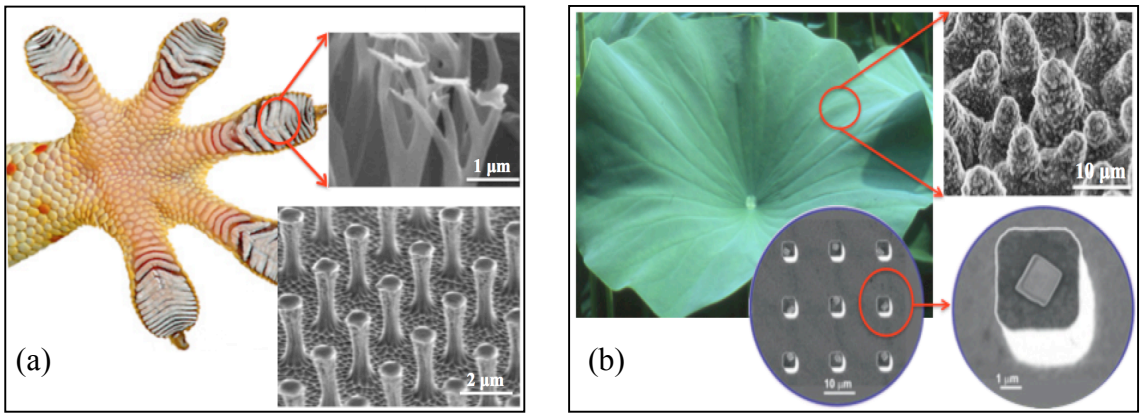

Fig. 1.1 Biomimetic Microstructures (a) Left: image of gecko foot, top right: SEM image showing gecko foot hair (from ref. [13]), bottom right: SEM image of polyamide micro-pillars structure for re-attachable dry adhesive inspired from gecko foot hair (from ref. [12]). (b) Left: image of super-hydrophobic lotus leaf, top right: SEM image of upper epidermis of lotus leaf shows distinctive hierarchical structure consisting of papillae hairs, bottom (from ref. [14]): SEM image showing hierarchical nano posts on top of micro pillars of silicon to make super hydrophobic surface (from ref. [15]).

Biologically inspired artificial compound eye is one of the most fascinating topics and has potential application in wide range of optical systems. The natural compound eye found in many insects can be mimicked to offer new paradigm for constructing miniaturized optical system for Omni-directional detection, fast motion detection or wide field-of-view [17]. The realization of these biomimetic structures using soft polymers like PDMS requires active research in some unconventional design, fabrication process and integration of microwires, micropillars, cantilevers and microlens into MEMS device.

Acoustic	Optical
Cochlear amplifier	Artificial ommatidia array
Cochlear speech recognition system	Vision-based magnetic compass
Dolphin based sonar receiver	
Binaural dolphin echolocation system	Mechanical
Micro echolocation system	Artificial halters
Binaural bat echolocation system	Artificial muscle spindle
	Artificial meissner corpuscles
Chemical	Artificial lateral line system
Artificial human tongue	Artificial arthropod hair cell
Artificial chemical recognition sites	Artificial cricket filiform hair array
Piezoelectric artificial human nose	Campaniform sensillum strain sensor
Conducting polymer artificial human nose	Carbon microcoil tactile sensors
Chemo-fluorescent artificial human nose	Electroactive polymer muscle
	Micromachined campaniform sensillum strain sensor
Electric	Artificial posture monitoring
Artificial electrolocation device	Artificial crustacean antenna
Fly based vision system	
Fly based, hexagonal oriented vision system	
Fly based, non-camera motion detection system	Thermal
Artificial bilayer lipid membrane	Photo-mechanical IR Sensor
Primate eye based vision system	ThermalSkin
Human eye based vision system	
Artificial muscle monitoring	

Fig. 1.2 Summary of Biomimetic research to make micro devices and sensors (from ref. [16])

BioMEMS

BioMEMS are the specific class of micro devices or systems used in biological applications. This includes many areas of research such as biomaterials, Lab-on-a-Chip (LOC), drug delivery devices, DNA microarrays and bio MEMS packaging [18]. It can be integration of several microstructures or devices, which can be shrunk down to micron or even submicron scale, to achieve complex function within single device. The major advantage of these systems over current diagnostics or implantable biotechnology is short operation time cycle, small sample volumes and reduction or elimination of human involvement in sample processing [19-20].

Researches have developed the biomaterials with controlled topography and surface chemistry to control the position, growth of cell and subsequent functions like adhesion,

orientation, migration, differentiation, proliferation and protein synthesis [21]. For example, migration of leukocytes mediates phagocytic and immune responses, migration of fibroblasts, vascular endothelial cells, and osteoblasts contributes to wound healing and tissue regeneration and tumor cell migration is essential to metastasis [22]. Similarly tissue growing and engineering its shape with 3D scaffold will help replace painful transplant and/or auto graft procedure. Two such examples are presented in Figure 1.3, (a) shows the 3D scaffold prepared by direct printing for bone tissue culture [23] and (b) shows the cell growth and motility in a cross-patterned surface using soft lithography [21].

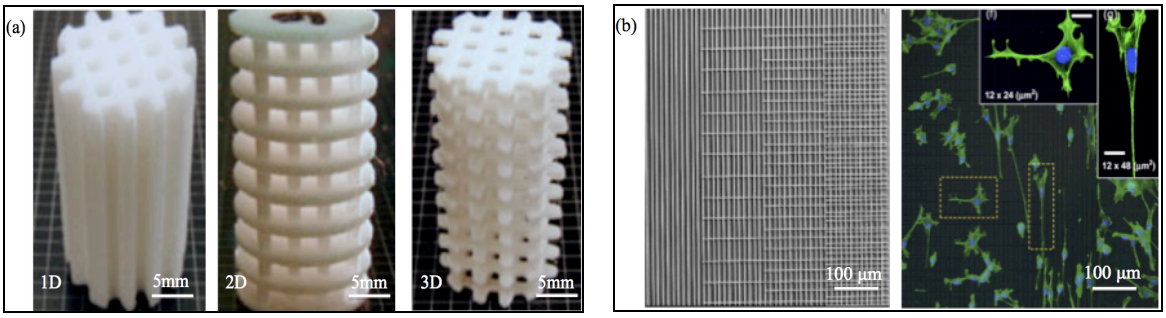

Fig. 1.3 Examples for patterns in biopolymers. (a) Images of 3D printed poly (carp lactone) scaffolds with 1D, 2D and 3D channels to be used for scaffold in bone tissue culture (from Ref. [23]). (b) Left: SEM image of cross-patterned polymer with pitch of 12 *µm* and Right: Fluorescence microscope image of NIH3T3 cells migration with along the ridges (from Ref. [21]).

One interesting topics in this regard is using biomaterials and bioMEMS for drug delivery system. Drug delivery is introduction of therapeutic substance into the human body by various anatomical routes by either be targeted release to particular tissues and/or disease or systematic release. In either case it is important to understand in detail the process to obtain optimal therapeutic efficacy and limit side effects. Several drug delivery microsystems have been

studied such as bio capsules made by binding porous biopolymer with the drug [24], micro needles for transdermal drug delivery to reduce pain in direct injection [25] and implantable microsystems with drug storage and delivery mechanism like micro-pump [26]. One of main focus area of drug delivery microsystem is in drug eluting stents (DES). Patients with coronary heart disease are treated with technique called coronary angioplasty whereby arteries are opened using balloon inflation. Stents (scaffolds) are placed on the artery to provide mechanical framework and prevent its narrowing (stenosis) [27]. The major concerns of the metallic or plastic stents are that they might induce varying degree of thrombogenesis (blood clotting), fibrosis (formation of excess fibrous tissue) and hyperplasia (cell proliferation). Also, restenosis usually occur within 3-6 months after coronary intervention [28-30]. This limit the clinical need for stent after that time making biodegradable stents an ideal alternative [31].

Immunosuppressant drugs can be loaded with the biodegradable polymer to avoid fibrosis and hyperplasia. The realization of biodegradable drug eluting stents with controlled drug release kinetics needs active research in the field of micro scale and nano scale patterning of the Food and Drug Administration (FDA) approved biopolymers like poly-L-lactic acid (PLLA), loading predetermined amount of drugs in the polymer micro/nano structures and the release mechanisms.

Problem Statements and Challenges

The first challenge we take is to mimic one of the nature's compact and complex designs such as compound eye of an insect for wide field of view optical design. The particular problem where wide field of view is required is solar concentrator [32]. The variation in solar path is shown in Fig. 1.4(a) [33]. The variation in daily path (elevation) is due to earth's rotation around

its axis and the seasonal variation (azimuth) is due to the inclination of earth's axis to its elliptical plane. This necessitates continuous compensation of the solar motion, in both azimuthal and elevation directions, for efficient solar concentrations and typically met by solar trackers. Figure 1.4(b) shows the solar elevation and azimuth angles for Washington DC where, at least 45° of acceptance angle is required to cover seasonal and 3 hours of daily solar path [34].

Since the integration of the PV conversion into everyday life, there has been focus to miniaturize the concentrators and integrate it with the household items with mainstream effort in the thin and flat solar concentrators (TFSCs). In TFSCs, sunlight impinging normally on their upper surface is condensed and launched into lateral propagation along a lightguide using light redirection elements (LRE) towards the edge where PV cells are installed. Primary focus of the TFSCs is the design of these LREs and has two important challenges. First, challenge is that they must not compromise with the thinness or flatness of the concentrator and the second challenge is that they must interact minimally with the light rays already redirected to reduce leakage. Several different solutions have been proposed based of gratings [35], holograms [36] and reflectors [37-39]. All of these existing schemes, however, are not well suited for wide-angle operations. For example, the TFSC by Karp *et al*. exhibits an acceptance angle of ±0.38° [38]. Achieving wide acceptance angle with static structures, while maintaining the thinness and flatness of the concentrator needs innovative design effort. Therefore the research objective to tackle this challenge is to employ the LRE design by mimicking ommatadia of the insect's compound eye for wide acceptance angle.

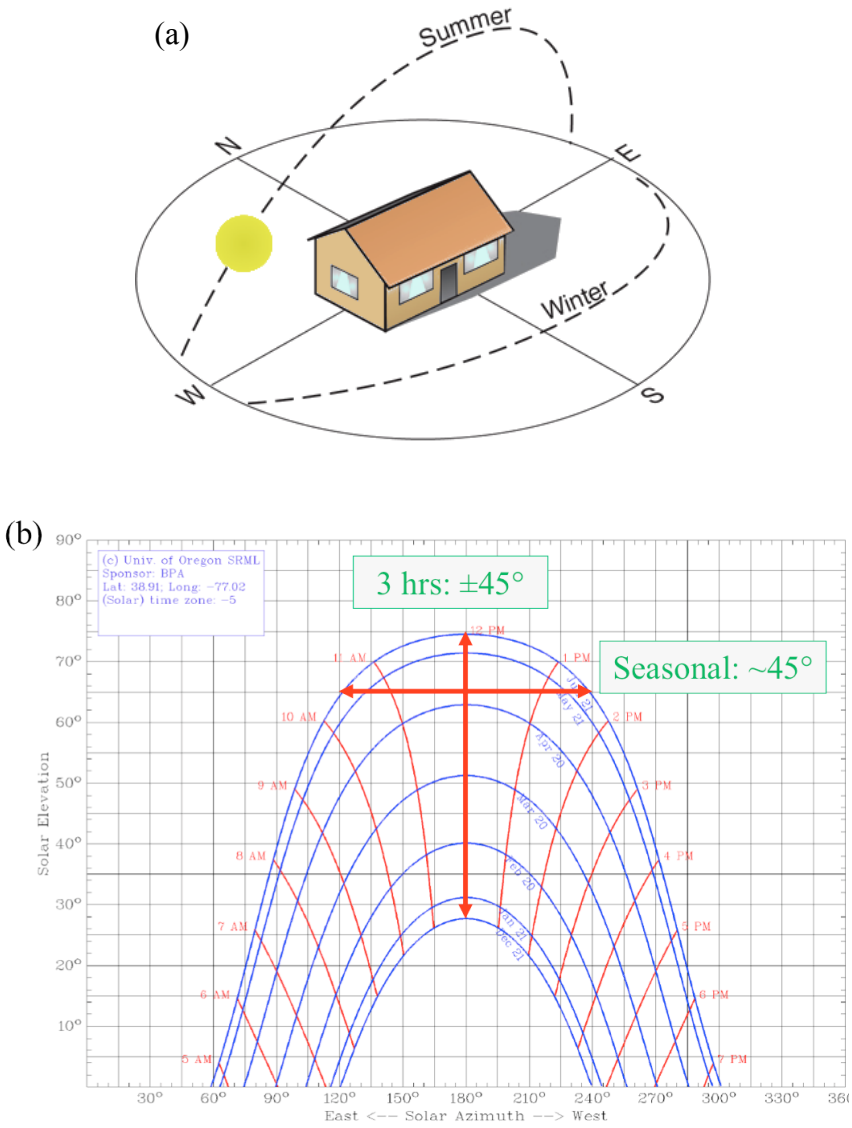

Fig. 1.4 (a) Daily and seasonal solar path (from Ref. [33]) and (b) Solar Chart of Washington DC (from Ref. [34])

As an extension to the TFSCs design we propose to deliver sunlight directly to the indoor lamp fixtures to improve the lighting efficiency. Lighting is the major area of electricity consumption in both residential and commercial sectors [40]. Indoor lighting is the main target

of renewable energy technologies, especially those based on solar power. Current solar-powered indoor lighting, however, is a two-step process in which sunlight is first converted into electricity through the photovoltaic effect and then converted back into light for illumination. With each conversion step less than 20% efficient, the overall conversion efficiency is inherently low at ~4% [41]. The solution to this particular challenge to increase overall efficiency is to deliver sunlight directly to the overhead lamp fixtures. Several such schemes based on lens/mirror combinations [42] and optical fibers [43] have already been demonstrated.

Making the solar indoor lighting comfortable to human eyes, however, requires additional processes since the light level must be kept constant and uniform through active control. A number of light control schemes have been developed over the past few years using several actuation mechanisms [44-46]. All of these existing actuators require externally supplied control and power for their operations. Eliminating such requirements can greatly facilitate the deployment and maintenance of the actuators and the light controller based on them but reports on such autonomous, self-powered light control schemes have been scarce to date. The research objective is to use the IR portion of the sunlight to actuate the phase change material to operate a MEMS switch.

Surface patterning of biodegradable PLLA to modify its surface structure is particularly important for using it as a template to cell growth or drug eluting stents (DESs) [47]. DES reduces the risk of re-blockage after angioplasty but the problem is that, it also triggers the platelet adhesion and activation of coagulation cascade to cause thrombosis. Various factors, such drug carrier polymer, drug elution profile and type of drug, affect the thrombosis. Two major challenges associated with drug carrier polymer are in-stent restenosis and late-stage thrombosis. Similarly, two major challenges associated with drug elution profile is that the drug

coating should have maximal drug loading capacity and minimum thickens such that it do not interfere with the performance of stent and the coating should be tailored to release the drug with optimal kinetics, such that drug concentration in the affected tissue are at efficacious but not toxic levels for a beneficial amount of time [48]. Nano texturing of the DESs has the potential to met these challenges and there are only few studies till date.

Several different approaches are available to pattern biodegradable polymers including lithography, pulsed laser, x-ray, e-beam, self-assembly, colloidal assembly, electrostatic assembly and nano-imprint. We investigate nano-imprint lithography (NIL) and drop casting of PLLA films to produce periodic nano-holes and nano-cones and optimize the coating process of the patterned surface using immunosuppressant drug sirolimus. We will finally investigate in vitro the drug release mechanism in phosphate buffer saline medium.

Organization of Dissertation

The dissertation has total of six chapters, including this chapter 1 introduction.

Chapter 2 illustrates the design of thin and flat solar concentrator using the inspiration from the compound eye of an insect. Compound eyes have extremely wide field of view and consists of many vision units called ommatidium, composed of lens and lightguide. A spacer optically connects the lens-lightguide pair. We designed bio-inspired solar concentrator composed of similar microlenses-lightguide pairs to collect the incoming solar radiation and flat bottom lightguide to redirect collected lightguide to solar cells mounting.

Chapter 3 is and extension work of chapter 2 whereby we designed and fabricated automatic light level controller switch using opto-thermo-mechanical MEMS design. We used

part of the solar radiation to heat the phase change material, paraffin wax and use the volume increase to produce actuation stroke for MEMS operation.

Chapter 4 illustrates novel, rapid fabrication method for nano-scale patterns in biodegradable polymers like PLLA. We used transfer-molding techniques like drop casting and nano imprinting to produce high fidelity pattern transfer form the PDMS master pattern into these biopolymers. These nanoscale periodic patterns have potential application for various biomedical platform technologies including cell growth and drug delivery. For potential application in drug delivery we developed the coating method of the FDA approved immunosuppressant drug, sirolimus.

Chapter 5 illustrates the application of nano-patterned PLLA in drug eluting stents. We can easily the patterned PLLA film into tubular structure to make it stents. We investigated the change in drug release profile as a function of time due to diffusion induced process. We have discovered that even though nano-patterning the drug release rate slows down due to incomplete wetting of the film increases the total available functional area.

Chapter 6 is the summary of the research work I have presented in this dissertation along with future insights.

References

[1] C. S. Smith, "Piezoresistive effect in germanium and silicon," *Phys. Rev.*, **94**, 1, 42-49 (1954).

[2] R. P. Feynman, "There's plenty of room at the bottom", *J. of Microelectromechanical systems*, **1**, 1, 60-66 (1992).

[3] H. C. Nathanson and R. A. Wickstrom, "A resonant-gate silicon surface transistor with high Q bandpass properties", *Appl. Phys. Lett.*, **7**, 4, 84-86 (1965).

[4] K. E. Petersen, " Silicon as a mechanical material," *Proceedings of IEEE*, **70**, 5, 420-457 (1982).

[5] E. Bassous, H. H. Taub and L. Kuhn, "Ink jet printing nozzle arrays etched in silicon," *Appl. Phys. Lett.*, **31**, 2, 135-137 (1977).

[6] E. W. Becker, W. Ehrfeld, D. Munchmeyer, H. Betz, A. Heuberger, S. Pongratz, W. Glashauser, H. J. Michel and V. R. Siemens, "Production of separation nozzle systems for uranium enrichment by combination of X-ray lithography and galvanoplastics," *Naturwissenschaften*, **69**, 520-523 (1982).

[7] M. Shimbo. K. Furukawa, K. Fukuda, and K. Tanzawa, "Silicon to silicon direct bonding method," *J. of Appl. Phys.*, **60**, 8, 2987-2989 (1986).

[8] O. Solgaard, F. S. A. Sandejas and D. M. Bloom, "Deformable grating optical modulator," *Opt. Lett.*, **17**, 9, 688-690 (1992).

[9] W. Piyawattanametha and Z. Qiu, "Optical MEMS," *Microelectromechanical Systems and Devices*, Dr. Azul Islam (Ed.) (2012)

[10] B. J. Kim and E. Men, "Review of polymer mems micromachining," J. of *Micromech. and Microeng.*, **26**, 013001-013022 (2016).

[11] J. F. V. Vincent, "Biomimetics – a review," *Proc. IMechE,* **223**, 919-939 (2009).

[12] A. K. Geim, S. V. Dubonas, I. V. Grigorieva, K. S. Nososelov, A. A. Zhukov and S. Y. Shapoval, "Microfabricated adhesive mimicking gecko foot hair," *Nature Materials*, **2**, 461-463 (2003).

[13] H. E. Jeong and K. Y. Suh, "Nanohairs and nanotubes: Efficient structural elements for gecko-inspired artificial dry adhesives," *Nano Today*, **4**, 4, 335-346 (2009)

[14] H. J. Ensikat, P. D. Kuru, C. Neinhuis and W. Barthlott, "Superhydrophobicity in perfection: the outstanding properties of the lotus leaf," *Beilstein J. Nanotechnol,.* **2**, 152-161 (2011).

[15] Y. Tian and L. Jiang, “Design of bioinspired, smart, multiscale interfacial materials with superwettability,” *MRS Bulletin*, **40**, 155-165 (2015).

[16] J. K. Stroble, R. B. Stone, S. E. Watkins,"An overview of biomimetic sensor technology", *Sens. Rev,*. **29**, 2, 112-119 (2009).

[17] J. Kim, K. H. Jeong, and L. P. Lee, “Artifical ommatidia by self-aligned microlenses and waveguides,” Opt. Lett,. **30**, 5-7 (2005).

[18] S. S. Saliterman, *Fundamentals of bioMEMS and Medical Microdevices*, Bellingham, WA: SPIE-The International Society for Optical Engineering (2005).

[19] A. C. R. Grayson, R. S. Shawgo, A. M. Johnson, N. T. Flynn, L. I. Yawen, M. J. Cima, and R. Langer, "A BioMEMS review: MEMS technology for physiologically integrated devices," *Proceedings of the IEEE*, **92**, 6-21 (2004).

[20] W. Wang and S. A. Soper, *BioMEMS: Technologies and Applications*, NY: CRC Press (2006).

[21] H. Jeon, H. Hidai, D. J. Hwang, K. E. Healy and C. P. Grigoropoulos, “Effect of micronscale cross patterns on fibroblast migration,” *Biomaterials*, **31**, 4286-4295 (2010).

[22] D. A. Lauffenburger, A. F. Horwitz, “Cell migration: a physically integrated molecular process,” *Cell*, **84**, 3, 359-369 (1996).

[23] A. Bandyopadhyay, S. Bose and S. Das, “3D printing of biomaterials,” *MRS Bulletin*, **40**, 108-115 (2015).

[24] T. A. Desai, "Micromachined therapeutic delivery systems: from concept to clinic," *Biomedical Instrumentation Based on Micro- and Nanotechnology*, *Proc. of SPIE*, **4265**, 26-35, (2001).

[25] D. V. McAllister, M. G. Allen, and M. R. Prausnitz, "Microfabricated Microneedles for Gene and Drug Delivery," *Annual Review of Biomedical Engineering*, **2**, 289-313 (2000).

[26] Z. S. Razzacki, T. K. Prasanna, M. Yang, V. M. Ugaz, and M. A. Burns, "Integrated microsystems for controlled drug delivery," *Advanced Drug Delivery Reviews*, **56**, 185-198 (2004).

[27] U. Sigwar, J. Puel, V. Mirkovitch, et al., “Intravascular stents to prevent occlusion and restenosis after transluminal angioplasty,” *N. Engl. J. Med.,* **316**, 701-706 (1987).

[28] P. W. Serruys, P. de Jaegere, F. Kiemeneij, et al., “A comparison of balloon-expandable-stent implantation with balloon angioplasty in patients with coronary artery disease”, *N. Engl. J. Med*., **331**, 489-495 (1994).

[29] P. W. Serruys, H. E. Luijten, K. J. Beatt, et al., "Incidence of restenosis after successful coronary angioplasty: a time-related phenomenon: a quanti- tative angiographic study in 342 consecutive patients at 1, 2, 3, and 4 months," *Circulation*, **77**, 361-371 (1988).

[30] T. Kimura, H. Yokoi, Y. Nakagaw, et al., "Three- year follow-up after implantation of metallic coronary-artery stents," *N Engl J Med*., **334**, 561-566 (1996).

[31] H. Tamai, K. Igaki, T. Tsuji, et al., "A biodegradable poly-*l*-lactic acid coronary stent in porcine coronary artery," *J. Interv. Cardiol*., **12**, 443-450 **(**1999).

[32] R. Winston, J. C. Minano, W. T. Welford, and P. Benitez, *Nonimaging Optics* (Academic, 2004).

[33] [Online] Available: http://nachi.org/images2012/sun-path.jpg

[34] Univ. of Oregon, Solar Radiation Monitoring Laboratory, Sun Path Chart Program, [Online] Available: http://solardat.uoregon.edu/SunChartProgram.html

[35] T. Tamir and S. T. Peng, "Analysis and design of grating couplers," *Appl. Phys. A.*, **14**, 235–254 (1977).

[36] R. K. Kostuk and G. Rosenberg, "Analysis and design of holographic solar concentrators," *Proc. SPIE*, **7043**, 70430I (2008).

[37] J. H. Karp and J. E. Ford, "Planar micro-optic solar concentration using multiple imaging lenses into a common slab waveguide," *Proc. SPIE*, **7407**, 7407–7411 (2009).

[38] J. H. Karp, E. J. Tremblay, and J. E. Ford, "Planar micro-optic solar concentrator," *Opt. Express*, **18**, 1122-1133 (2010).

[39] B. L. Unger, "Dimpled Planar Lightguide Solar Concentrators," Ph.D. dissertation, The Institute of Optics, University of Rochester, Rochester, NY (2010).

[40] [Online] Available: http://www.eia.gov/tools/faqs/faq.cfm?id=99&t=3

[41] J. D. Muhs, "Hybrid solar lighting doubles the efficiency and affordability of solar energy in commercial buildings," *CADDET Energy Efficiency Newsletters*, 6-9 (2000).

[42] L. M. Fraas, W. R. Pyle and P. R. Ryason, "Concentrated and piped sunlight for indoor illumination," *Appl. Opt.*, **22**, 578-582 (1983).

[43] M. A. Dugway and R. M Edgar , "Lighting with sunlight using sun tracking concentrators," *Applied Optics*, **16**, 1444 (1977).

[44] W. Song and D. Psaltis, "Pneumatically tunable optofluidic 2 × 2 switch for reconfigurable optical circuit, " *Lab Chip*, **11**, 2397-2402 (2011).

[45] W. Song and D. Psaltis , “Electrically tunable optofluidic light switch for reconfigurable solar lighting, “ *Lab Chip*, **13**, 2708-2713 (2013).

[46] H. E. Hong, C. S. Chen, K. L. Fang, S. Y. Yang and J. J. Chieh, “Tunable optical switch using magnetic fluids,” *Appl. Phys. Lett.*, **85**, 23, 5592-5594 (2004).

[47] S. Shi, X. H. Wang, G. Guo, M. Fan, M. J. Huang and Z. Y. Qian, “Preparation and characterization of microporous poly (D, L-lactic acid) film for tissue engineering scaffold,” *Int. J Nanomedicine*, **5**, 1049-1055 (2010).

[48] K. K. Jain, "Drug Delivery System," in *Methods in Molecular Biology*, vol. 437, J. M. Walker, Ed. Totowa, NJ: Humana Press, 2008

CHAPTER 2

BIO-INSPIRED THIN AND FLAT SOLAR CONCENTRATOR FOR EFFICIENT WIDE ACCEPTANCE ANGLE LIGHT COLLECTION

Modified from paper published in Applied Optics

Rabin Dhakal, Jewon Lee and Jaeyoun Kim

Abstract

We present a novel thin and flat solar concentrator design, inspired by the structure and optical functionality of the ommatidium in the compound eye of insects. By combining a microlens with a curved light guide, rather than the conventionally employed dielectric or metallic reflectors, we could simultaneously achieve low-loss light redirection and wide acceptance angle without compromising the overall thinness or flatness of the concentrator. Through design optimizations, we could achieve optical concentration factors up to 39 and acceptance angle up to 15° while maintaining the thickness of the concentrator under 1.1 *cm* for a length of 20 *cm*. We also showed that the optical concentration factor could be further increased to 81 through tapering of the geometry.

Introduction

The number of photovoltaic (PV) cells required to cover a unit area is critical to the cost-effectiveness of solar energy conversion. To reduce this, various schemes have been developed to condense the sunlight collected from a large area into a small destination region installed with PV cells [1,2]. Conventionally, the effort to develop such solar concentrators has been focused on large-scale systems for big solar farms [3]. The recent trend to incorporate PV conversion into

everyday life leads to a focus on miniaturized concentrators that can be integrated with household and house-building items, although at the expense of lowered collection efficiency levels.

Concentrators in the form of thin and flat plates constitute the mainstream of efforts to date. Such thin and flat solar concentrators (TFSCs) condense sunlight impinging normally on their broad upper surface, first by changing its propagation direction by ~90° and then launching it into lateral propagation along the plate, toward the edge where the PV cells are installed [3,4]. As shown in Fig. 2.1(a), the plate body functions as a light guide, enabled by total internal reflection (TIR). Essential to this TFSC scheme is the optical element that redirects the vertically incident sunlight into lateral propagation. In fact, realization of this light redirection element (LRE) has been the primary focus in the development of TFSCs. A number of different schemes, based on gratings [5], holograms [6], and reflectors [7], have been demonstrated. The LREs must satisfy the following requirements:

(1) They must not compromise the thinness or flatness of the concentrator. This requirement is challenging since the redirection angle for ensuring the TIR-guided lateral propagation is often close to 90°.

(2) They must interact minimally with the light rays that are already redirected and under TIR-guided lateral propagation. To those, the LREs merely function as the defects in the light guide that will spoil the TIR and induce light leakages.

In many existing LRE schemes, these two challenges have been tackled in combination, as shown in Fig. 2.1(b) [7–9]. The sunlight impinging on the plate's upper face first encounters an array of micro- lenses, which focus the light onto a matching array of LREs on the lower face. Owing to the focusing, the LREs can be much smaller than the microlens, allowing the LRE

array to occupy only a small fraction of the plate's lower face area. This greatly reduces the LREs' chances to interact with the already redirected, laterally propagating light rays. The short focal length of the microlens also ensures a narrow separation between the upper and lower faces, which leads to thin concentrator designs.

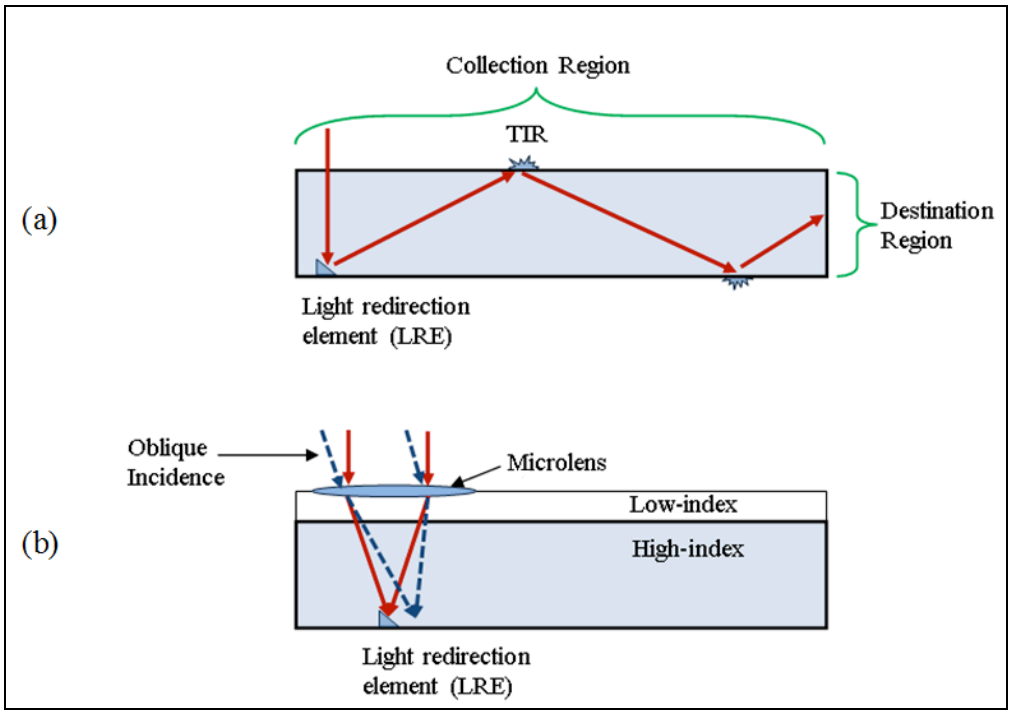

Fig. 2.1 (a) The operational principle of conventional TFSCs. (b) The microlens–LRE pairing scheme adopted in conventional TFSCs. This can reduce the fraction of the bottom surface area taken up by the LREs, but narrows the acceptance angle.

Existing LREs include the metallic reflector-based scheme demonstrated by Karp and co-workers [7,8] and the asymmetric pyramidal element-based scheme by Unger [9]. The scheme by Karp et al. uses 120° apex symmetric prisms to tilt the normally incident light. These prism couplers were molded to the base plate using a self-aligned fabrication technique [8]. The LRE

used in the concentrator by Unger is an asymmetric reflector, designed specifically to minimize the interaction with light that is already launched into the lateral propagation [9].

One additional feature strongly desired for the solar concentrator is a wide acceptance angle. The variation in the solar path [10] necessitates continuous compensation of the solar motion, in both azimuthal and elevation directions, for efficient solar concentration. This has been typically handled with the help of solar trackers. With LREs capable of redirecting sunlight impinging with a wide range of incidence angles, we can reduce this dependence on the solar trackers. Existing microlens-reflector-coupled schemes, however, are not well suited for wide-angle operations. Due to the small size of the LRE, light impinging with a nonzero incidence angle will focus onto a point not covered by the LRE, as depicted in Fig. 2.1(b), leading to a failure in redirection and a narrow acceptance angle. For example, the TFSC by Karp et al. exhibits an acceptance angle of 0.38° [11]. It is possible to increase the acceptance angle with the help of mechanical tracking, as has been done by Hallas et al., and to increase the acceptance angle of the design of Karp et al., to 18° in both directions [12]. They used a mechanical micro tracker to move the position of the plate waveguide with respect to the lens, such that light is impinged on the LRE for nonzero incidence angles. Achieving a wide acceptance angle with static structures while maintaining the thinness and flatness of the concentrator has been considered a great challenge.

Proposal for a Bio-Inspired TFSC Design

In this work, we present a new LRE scheme capable of redirecting light rays impinging with a wide range of incidence angles while minimizing the disruption to already redirected light. The enabling factor is the use of a biologically inspired light manipulation scheme. This

widens the acceptance angle in one direction and allows the coverage of a large fraction of the sun's daily motion, leaving only the seasonal movement to be actively tracked. Figure 2.2(a) shows the proposed LRE design in a cross-sectional view. Similar to previously reported schemes, the micro- lens functions as the light collection element. Our design, however, couples the collected light into a thin, curved light guide that gradually redirects the light into lateral propagation, in contrast to the abrupt redirection employed in conventional, reflector-based LRE schemes. The source of inspiration for such pairing of a light-collecting microlens and a light guide is from the structure of the biological ommatidium, the vision unit of an insect's compound eye [13–15].

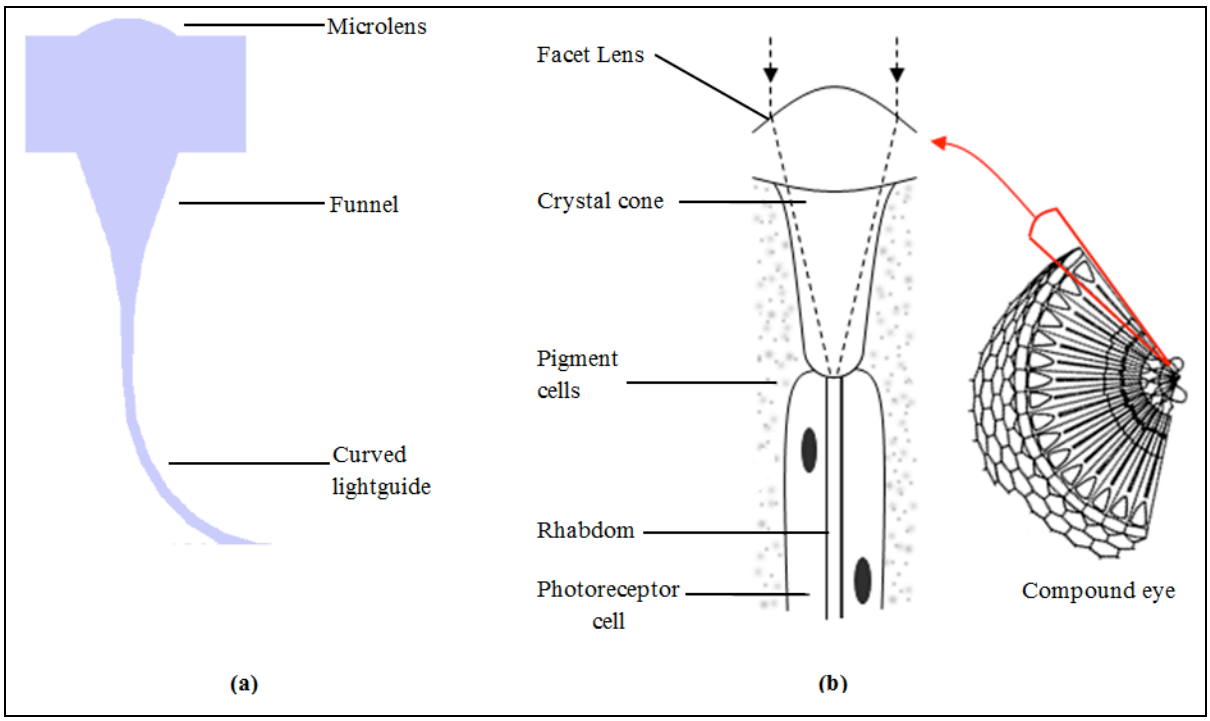

Fig. 2.2 (a) The proposed LRE in a cross-sectional view. (b) Diagrams of a compound eye and an ommatidium, its vision unit (Compound eye diagram courtesy of Biodidac Project).

As shown in Fig. 2.2(b), the compound eye comprises a large number of ommatidia to achieve an extremely wide field-of-view in a small form-factor [16]. Each ommatidium consists of a facet lens, which collects and focuses light, and a cylindrical rod, called a rhabdom, which functions as a light guide. These two structures form an optically coupled lens–waveguide pair. The conic spacer between them precisely positions the upper facet of rhabdom at the focal spot of the lens. The light coupled into the rhabdom is detected by the photoreceptors [13–16].

The similarity between the ommatidium and our scheme, however, stops at this basic concept level. To function as pixels in an imaging array, the ommatidium takes a cylindrically symmetric form, realized by rotating the profile in Fig. 2.2(b) about its center axis. As a pixel element, the ommatidial structure is optimized to minimize the acceptance angle, which makes them unsuitable for wide-angle light collection [17,18]. To widen the acceptance angle, we extruded the basic profile in Fig. 2.2(a), as shown in Fig. 2.3(a). Attaching a rectangular plate, which functions as the bottom light guide, then completes the realization of TFSC.

In this device geometry, the oblique incidence can be decomposed into two components, one in the y–z plane and the other in the x–z plane. In the former, depicted in Fig. 2.3(b), the obliquely waveguided as it slides down the curved light guide for smooth redirection and, eventually, reaches the edge of the bottom plate light guide, as evidenced by the ray traces super-imposed on Fig. 2.3(b). On the other hand, the obliquely incident light rays in the x–z plane suffer from optical aberrations, as shown in Fig 2.3(c). The tolerance due to this provides funnel-shaped light collection geometry.

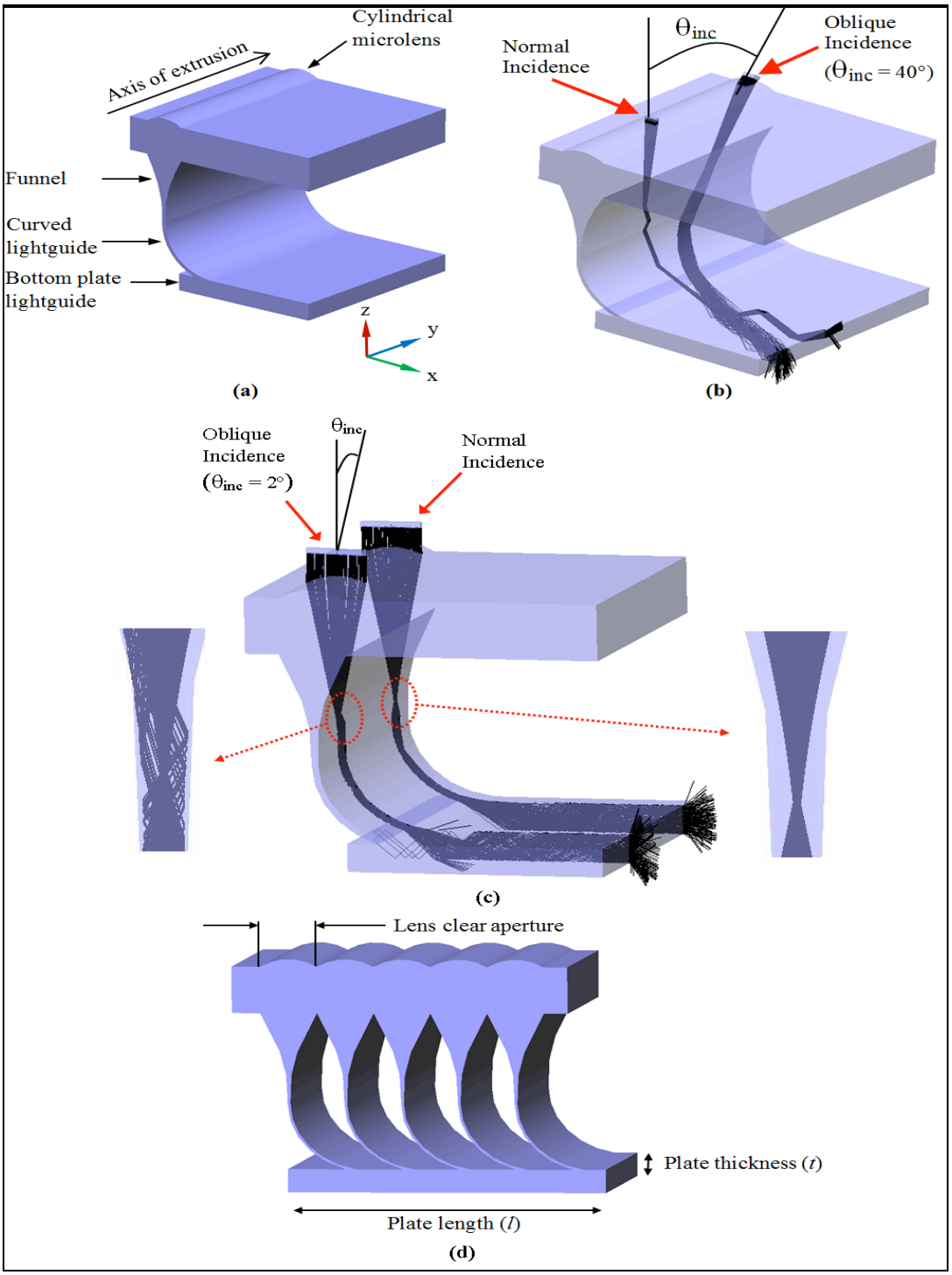

Fig. 2.3 (a) A schematic diagram of the proposed LRE, realized by extruding the cross-sectional geometry in Fig. 2.2(a) along the y-axis. Both (b) and (c) are ray-tracing results, superimposed to show the tolerance of the proposed LRE to the oblique incidence in the y–z plane and the x–z plane, respectively. (d) A schematic diagram showing a TFSC comprising multiple unit-cells.

Basic Settings for Design and Evaluation

We utilized the ray tracing capability of *LightTools*^{TM} to design the TFSC and optimize its light concentration performance and acceptance angle. The light source was solar spectrum corresponding to the blackbody temperature of 5800°K spanning 360~830 nm range. To construct the TFSC structure, we first designed the basic profile in 2D and extruded it in the *y*-direction. The unit structure was then repeated along the *x*-direction to form a long TFSC. Figure 2.3(d) shows one example comprising five unit-cells. We assumed that the entire structure was built with a polymer (n = 1.426) and surrounded by air. The corresponding critical angle was 44.53°. The transmission property of the polymer was same as that of BK7 glass [19]. Figure 2.4 shows the internal transmittance of 2.5 *cm* thick polymer along with the normalized spectral intensity of the solar radiation.

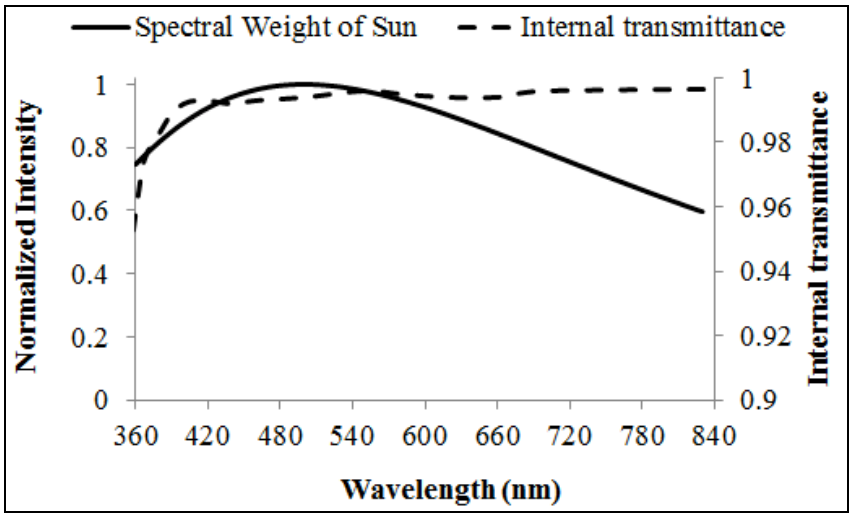

Fig. 2.4 Spectral weight of the solar radiation corresponding to blackbody temperature of 5800°K and transmittance of 2.5 cm thick polymer.

The performance of the TFSC was quantified by the following three figures of merit. The geometrical concentration ratio C_{GEO} is the ratio between the area of light collection region and that of the destination region. In our TFSC geometry, it is equivalent to the ratio between the lens clear aperture CA multiplied by the number of unit-cells N and the thickness of the bottom plate t as specified in Eq. 2.1. The optical collection efficiency η is the ratio between the power retrieved at the destination region and the power entering the collection region as specified in Eq. 2.2. This ratio is always less than unity due to Fresnel reflection, material absorption, and light leakage at the junction which will be explained below. Since C_{GEO} increases with N while η decreases with it, we set their product as the overall figure of merit and named it the total optical concentration factor C_{TOT}. As shown in Eq. 2.3, C_{TOT} is also equivalent to the ratio between the intensity at the destination region and that at the collection region. The acceptance angle is defined as the η drops to 90% of its maximum value plotted as a function θ_{inc}. To summarize,

$$C_{GEO} \equiv \frac{Area\ of\ light\ collection\ region}{Area\ of\ the\ destination\ region} = \frac{CA \times the\ number\ of\ unit\ cells}{t} \tag{2.1}$$

$$\eta \equiv \frac{Power\ obtained\ at\ the\ destination\ region}{Power\ entering\ the\ collection\ region} \tag{2.2}$$

$$C_{TOT} = C_{GEO} \times \eta \equiv \frac{Intensity\ at\ the\ destination\ region}{Intensity\ at\ the\ collection\ region} \tag{2.3}$$

At this point, comparison with an existing structure can re-emphasize our design and optimization goals. Our design concentrates the light incident on a plane to a focal line. The maximum C_{GEO} attainable for such a line concentrator is determined by its acceptance half-angle θ and refractive index of the surrounding medium n as [1]:

$$C_{GEO-\max} = \frac{n}{\sin\theta} \tag{2.4}$$

Ideally, θ is limited by the finite size of the sun's disk subtending an angle of ±0.26° which, in air, leads to $C_{GEO\text{-}max} \sim 216$. Achieving the upper limit thus depends on law of non-imaging optics. However, the sun occupies large portion of sky over the year and requires highly accurate tracking for high concentrator systems. In practice, C_{GEO} is traded with the acceptance angle. For example, current parabolic trough designs exhibit $C_{GEO} \sim 75$ and $\eta \sim 0.77$ with its acceptance angle increased to ~±0.7° [20]. Each row of the parabolic trough, however, functions individually. Our TFSC design focuses on increasing the acceptance angle at the expense of C_{GEO} and the tries to compensate it by improving the efficiency of adding up the outputs from multiple rows.

TFSC Optimization Process and Results

We optimized our design in two steps. In the first step, we focused on optimizing one LRE unit-cell so that its light redirection efficiency and acceptance angle can be maximized in the two mutually orthogonal incidence planes, *i.e.*, the *x*-*z* and *y*-*z* planes specified in Fig. 2.3(a). Throughout the optimization process, we tried to keep the overall height of the unit-cell under ~1 cm.

In the second step, we configured full TFSCs by assembling multiple LREs and optimized their arrangements to achieve minimal propagation loss and maximal C_{TOT}. As stated above, adding unit-cells increases C_{GEO} but also degrades the lightguiding performance of the bottom plate. Light leakage, shown in Fig. 2.5, is the main cause. As shown in the insets of Fig. 2.5, the curved lightguide forms an angled junction with the bottom plate. Rays impinging on

these junctions will see their incidence angle decreased by the amount of lightguide-plate angle as depicted in the inset **A** of Fig. 2.5. If this new incidence angle is below the critical angle, the light will leak at the junction as shown in the inset **B**. Even if the angle was above the critical angle at the junction itself, there still is the possibility that the subsequent reflection at the bottom face of the plate is at an angle too steep for TIR, eventually resulting in a leakage as depicted in the inset **C**. Minimization of the junction's detrimental impact was the focus of the second step.

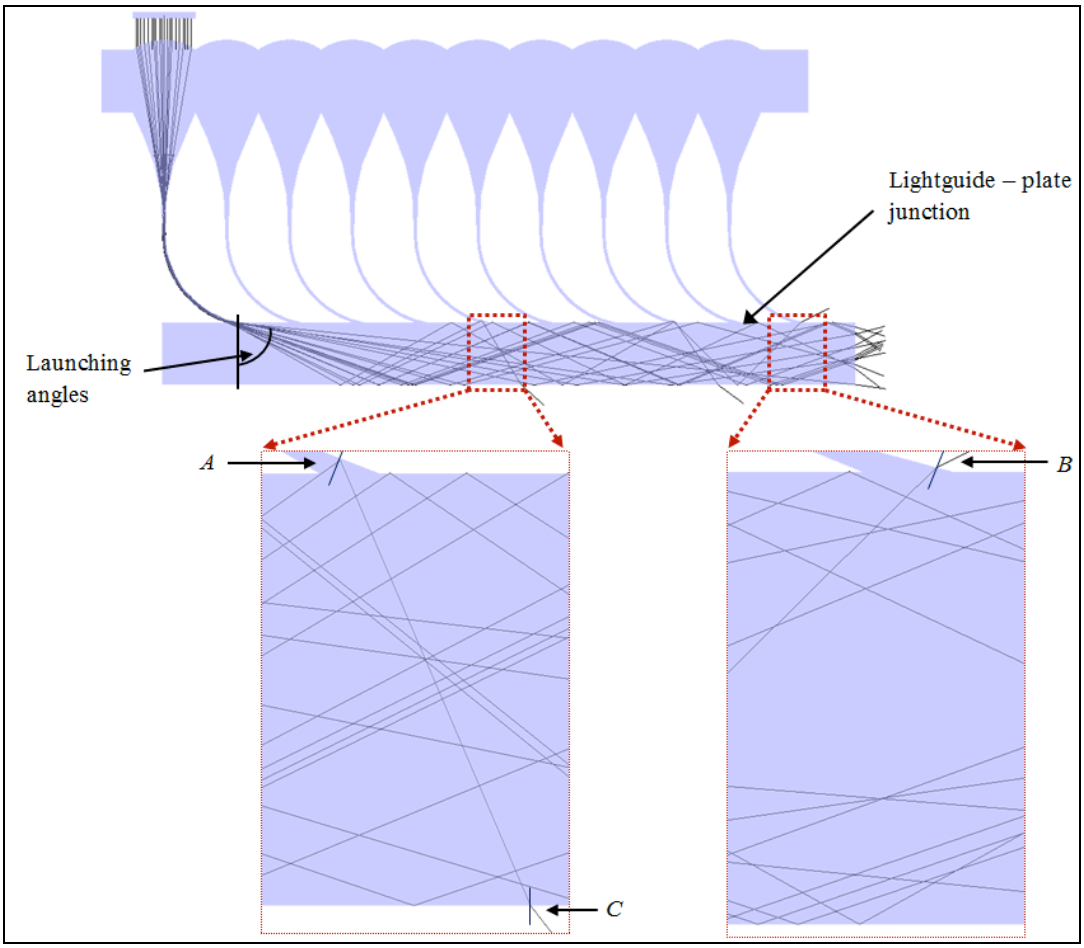

Fig. 2.5 Mechanisms of light leakage near the junction of two lightguides. Magnified views at **A** and **B** show the decrease in the incidence angle and the consequential light leakage at the junction. In some cases, the light will leak at the subsequent reflection as shown in **C**.

Unit cell optimization

The LRE unit-cell's acceptance angle and light redirection efficiency must be optimized in both the *x*-*z* and *y*-*z* planes specified in Fig. 2.3(a). We carried out the former first. In the *x*-*z* plane, as shown in Figs. 2.6(a) and (b), the microlens must be able to handle both normally and obliquely incident rays. For the former, the thickness and curvature of the lightguide are to be chosen carefully so that the focused rays can be completely redirected and launched into the bottom plate at an angle greater than the critical angle. From repeated simulations, we learned that the main parameters determining the LRE's performance for the normally incident rays are the *F*-number and clear aperture (*CA*) of the microlens. On the other hand, the obliquely incident rays won't be focused exactly at the entrance of the curved lightguide. Instead, they will converge near the junction between the funnel and the curved lightguide and some of them may hit the side of the funnel in the process as shown in Fig. 2.3(c). The LRE unit-cell needs to redirect these obliquely incident rays into the lightguide as well. Again from iterative simulations, we learned that the funnel's angle of flaring (shown in Fig. 2.6(b)) and its shape play important roles in the process.

Table 2.1 Design parameters for LRE with different F-numbers

F-number	Clear Aperture [mm]	Lightguide Thickness [mm]	Curvature of Lightguide [mm]	Funnel Angle	Acceptance Angle	
					x-*z* plane	*y*-*z* plane
F/1.25	4	0.3	3.2	77.3°	±0.76°	±26.2°
F/1.70	3	0.2	3.2	60°	±0.77°	±27.4°
F/2.55	2	0.1	2.95	42.1°	±0.78°	±28.1°
F/4.00	1.28	0.1	2.95	27.7°	±0.78°	±27.9°

Table 1 summarizes the result of the LRE unit-cell optimization. We started out with microlenses with four different values of *F*-number and optimized the LRE by adjusting the values of *CA*, the angle and shape of the funnel, and the curved lightguide parameters. Among them, the LRE with a *F*/2.55 lens with 2 mm *CA* exhibited the best performance when the thickness and curvature of the curved lightguide were set to 0.1 mm and 2.95 mm, respectively. We designed the funnel with the hyperbolic curvature by connecting the funnel opening (Point **A** in Fig. 2.6(a)) with the topmost point of the lightguide (Point **B** in Fig. 2.6(a)) using the double-point spline function of *Solid Works*™. The asymptotic lines at the funnel openings functioned as the guides to set the funnel angle as shown in Fig. 2.6(b). The optimized funnel angle was 42.1° and the angle of the asymptotes was 111.05°.

Figures 2.6(c) and 2.6(d) show the computed η for the LRE with the *F*/2.55 lens as a function of the incidence angle in the two planes of incidence. In the *x*-*z* plane, the microlens-lightguide paired LRE exhibited ±0.78° of acceptance angle. This value is slightly greater than those observed in existing microlens-reflector pair-based LREs [7-9], thanks to the existence of the funnel structure in between. On the other hand, the acceptance angle in the *y*-*z* plane reached ±28.1°, confirming the 2D-extruded LRE's high level of tolerance to oblique incidence. As shown in Fig. 2.3(b), the oblique rays in the *y*-*z* plane will eventually hit the side of the LRE in the *x*-*z* plane and be reflected back. For complete lightguiding and concentration, the reflection must be in the range of TIR. Figure 2.6(e) shows the computed incidence angle at the side of the LRE as a function of the ray's original incident angle in the *y*-*z* plane. The graph shows that TIR is maintained for initial incidence angles up to 80°, indicating that the sides won't cause light leaks.

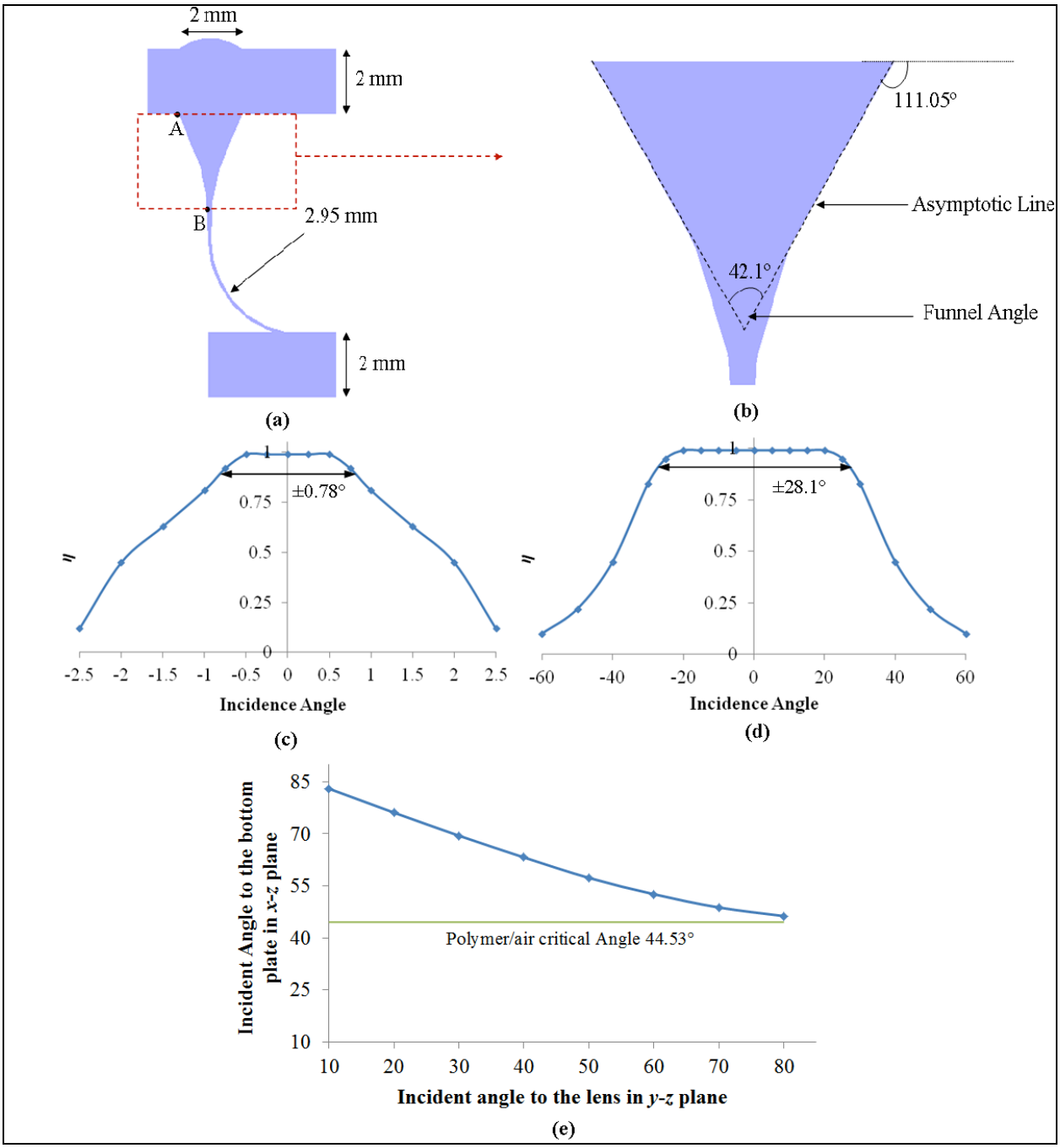

Fig. 2.6. (a) LRE unit-cell with F/2.55 lens. (b) Funnel design for the F/2.55 unit-cell. (c) And (d) are the computed η of the F/2.55 unit-cell as a function of the incidence angle in x-z and y-z planes, respectively. (e) Effect of Incidence angle to the lens in y-z plane on the incident angle to the side of the bottom plate in x-z plane.

Multiple cells: rectangular geometry

With the basic LRE unit-cell designs optimized, we proceeded to the design and optimization of the multi-cell TFSC structures. Multi-cell TFSCs were realized by juxtaposing multiple LRE unit-cells. Two mechanisms mainly affected the level of attainable C_{TOT}. On the one hand, C_{GEO} increases linearly with N, the number of unit-cells. On the other hand, the level of η inevitably decreases with increasing N because the light collected at areas far away from the destination region, *i.e.*, the edge, has to propagate a long distance and suffers from cumulative light leak loss at the junctions.

To improve η and C_{TOT}, the total area in the upper surface of the bottom plate taken up to form junctions with the tail parts of the curved lightguide must be minimized. From the simulations, we learned that the area of a junction and its numbers are primarily governed by the *F*-number and *CA* of the microlens. Care must be taken in determining the two parameters. While microlenses with lower *F*-numbers and wider *CA* can certainly reduce the number of LREs required to achieve a certain C_{GEO}, they also lead to thicker lightguides and wider junction areas. We utilized the four microlenses in Table 1 to find the optimum point.

Figure 2.7(a) shows the impact of the microlens' *F*-number on η in multi-cell TFSCs comprising different number of LREs under normal illumination. While η remains unchanged for $N = 1$, it exhibited a definite peak at ~*F*/2.55 for all other multi-cell TFSCs, which can be clearly attributed to the change in the total junction area. Our simulations showed that when the *F*/2.55 lens was adopted, the junctions would take less than 20% of the area of the bottom plate's upper surface. The junction area increases to 28.1% and 31.4% for *F*/1.25 and *F*/1.7 lenses, respectively, due to the increase in the size and curvature of the curved lightguide. In the case of

F/4.0 lens, the fraction of the junction area increases again to 32.9 % since the number of unit-cells required for the same C_{GEO} itself got increased in this design. Given the results of unit-cell and multi-cell optimization results, we set the *F*/2.55, 2 mm-*CA* microlens as the basis for further multi-cell TFSC design and optimization.

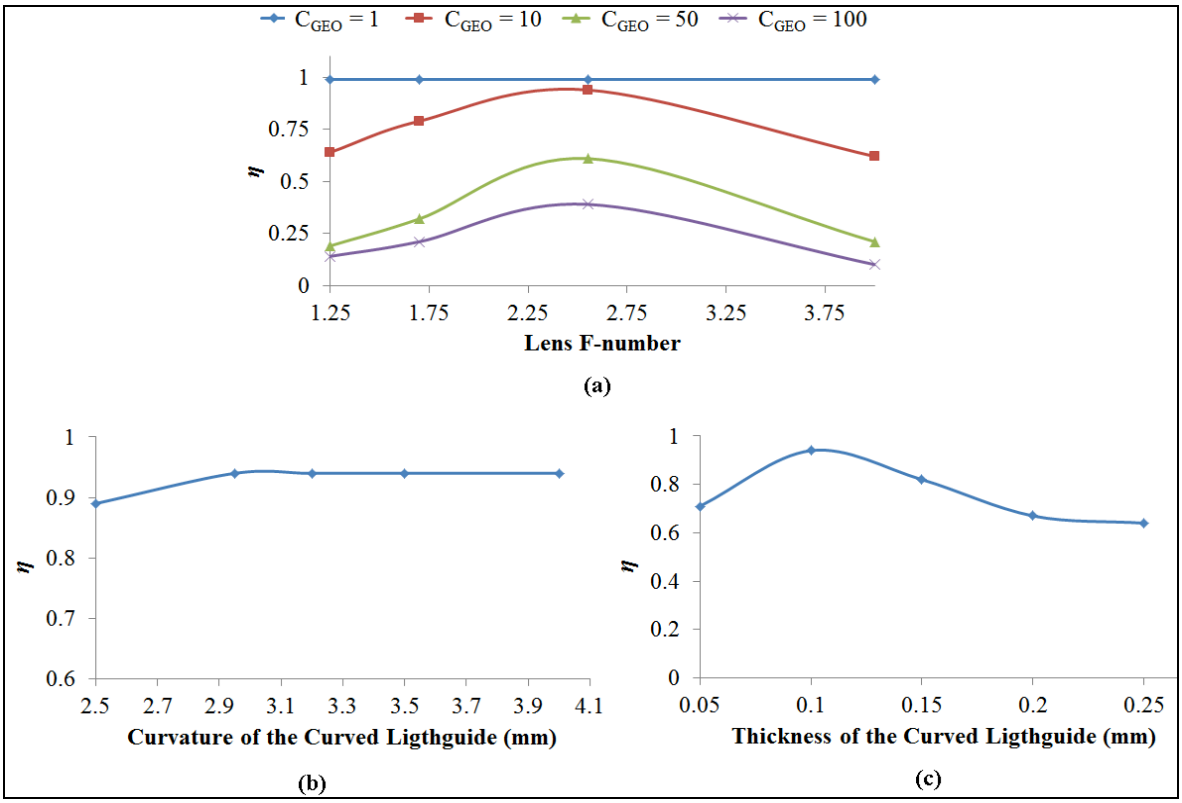

Fig. 2.7 (a) The effect of the *F*-number on η *for* different C_{GEO} and (b), The effect of the lightguide's curvature on the η values of a $N = 10$ system. (c) The effect of the thickness of the lightguide on the η values of a $N = 10$ system. In both (b) and (c), each LRE employed a *F*/2.55 lens and a lightguide with 2.95 mm curvature and 0.1 mm thickness.

Figure 2.7(b) shows the impact of the lightguide's curvature on η of a $N = 10$ system. Clearly, η reached its maximum value as the curvature approached 2.95 mm and then stayed constant. Figure 2.7(c) shows the impact of the thickness of the curved lightguide on η of a $N =$

10 system. Initially, as the lightguide thickness increased from 0.05 mm to 0.1 mm, the η value increased as well to reach its peak of 0.94, owing to improved coupling and guiding. Beyond the point, however, the detrimental impact of the light leakage at the junction areas became stronger than the positive impacts, resulting in a decrease in η with increasing lightguide thickness. In accordance with the simulation results described above, we set our model LRE with a *F*/2.55, 2mm-*CA* lens paired with a 0.1 mm-thick lightguide with 2.95 mm curvature. The shape of the funnel was already described above. The overall height of the LRE remained under 1.1 ~ 1.21 cm.

For further design and optimizations, we constructed large-scale multi-cell TFSCs by assembling the LRE unit-cells optimized above. Figure 2.8(a) shows a $N = 100$ TFSC as an example. Figures 2.8(b) and 2.8(c) show its η values as functions of the incidence angle in the *x*-*z* and *y*-*z* planes. For comparison, *N* was gradually increased from 1 to 10, 50 and 100. The corresponding C_{GEO} for these structures are 10, 50 and 100 as well, respectively. The curves clearly show that both η and the acceptance angle decrease as the unit-cell count *N* increases. For example, the peak η value attainable with normally impinging sunlight decreases from 100% to ~60% and ~40% as *N* increases to 50 and 100. The light leak at the junctions as shown in Fig. 2.5 constitutes the majority of the loss. Simulation results suggests that ~90% and ~86% of the total loss are due to light leaks at the junction for N = 50 and 100 system respectively. For the longest TFSC with $N = 100$, *i.e.*, 20 cm in length, the acceptance angle remains within to $\pm 0.5^{\circ}$ in *x*-*z* plane and within $\pm 15^{\circ}$ in the *y*-*z* plane. Also the values of η remain above 50% of the peak value (FWHM angle) for incidence angle up to $\pm 1.3^{\circ}$ in *x*-*z* plane and within $\pm 32^{\circ}$ in the *y*-*z* plane.

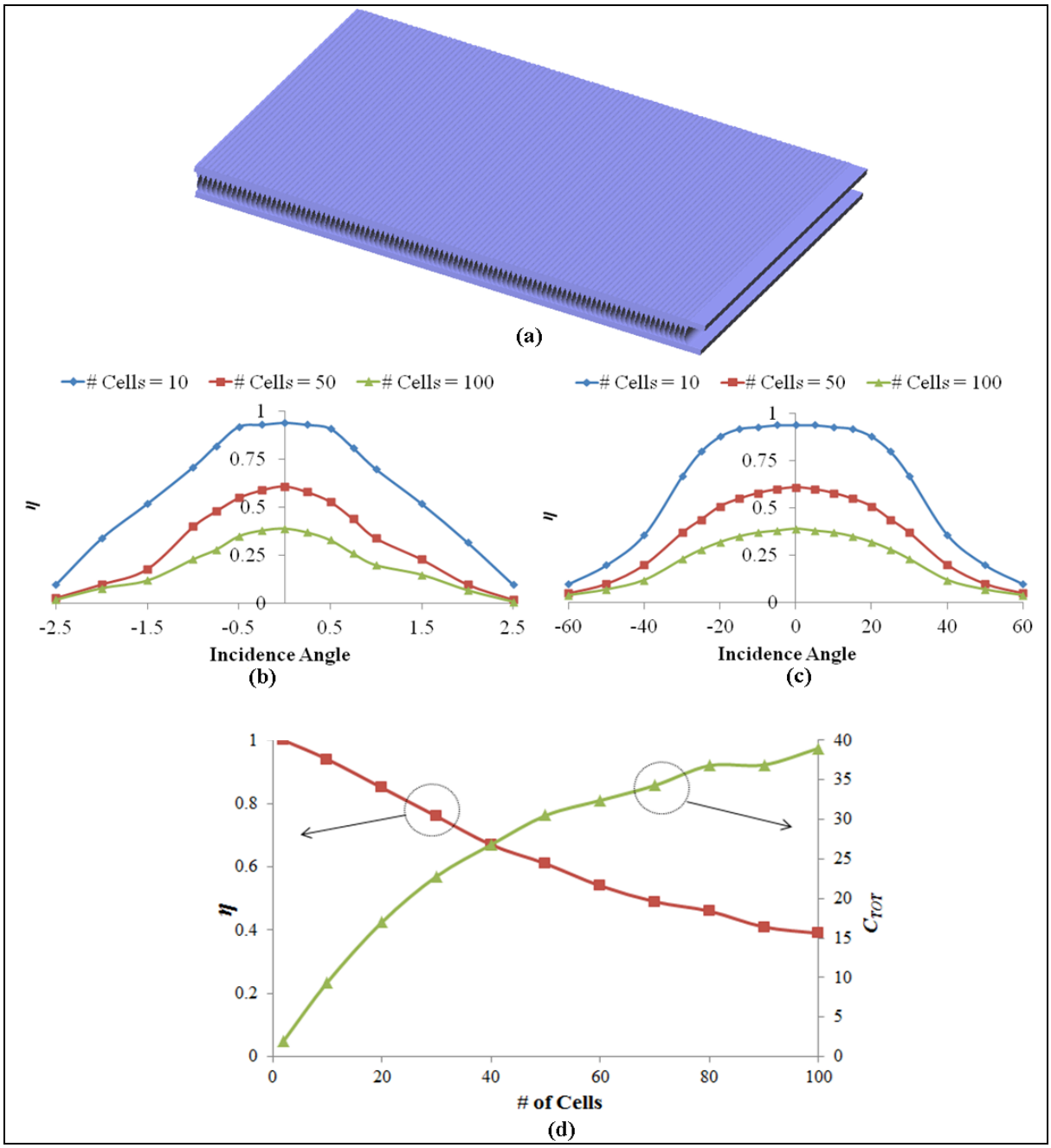

Fig. 2.8 (a) A multi-cell TFSC design comprising 100 unit-cells. (b) And (c) show the simulated η plotted as a function of the incidence angle in the (b) *x-z* and (c) *y-z* planes of Fig. 2.3(a). (d) The simulated η and C_{TOT} plotted as a function of the number of the unit-cell N for the case of normal incidence.

The values are lower than those obtained from a single unit-cell above. The FWHM angle in the *y*-*z* plane, however, is still wide enough to cover approximately 80 (at the summer solstice) to 240 (at the winter solstice) minutes of daily solar cycle around noon in Washington, D.C. throughout the year [10], provided that the TFSC is mounted on a slow tracking system which compensates the seasonal change in the solar elevation angle. Even in the case of dual-axis solar tracking, the wide acceptance angle will help relax the precision required for tracking and reduce the cost for its implementation.

It was stated previously that an increase in N causes two competing effects on C_{TOT}, *i.e.*, the increase in C_{GEO} and the decrease in η. To quantify the change in their relative impact with increasing TFSC length, we obtained η and C_{TOT} as functions of N from the simulations and superimposed them in Fig. 2.8(d). Normal incidence is assumed. The two curves clearly show that in our TFSC geometry, the increase in C_{GEO} with N is strong enough to compensate for the degradation in η at least up to $N = 100$. Up to $N = \sim 30$, the C_{TOT} value keeps increasing linearly with N. Beyond the point, the slope of the C_{TOT} curve decreases but the overall value keeps increasing in proportion to $N^{½}$. This indicates that the light collected and launched by the LRE unit-cell optimized above can sustain itself through the propagation along a 100 unit-cells.

The solar power at the end facet for the $N = 100$ concentrator increases to 7.92 W from the 0.2 W without concentrator for direct AM 1.5 illumination at the peak. The average η becomes 20% for FWHM angle of ±32°, resulting in 4 W of average power at the receiving end. At this rate, Si-based solar cells with 20% module efficiency can produce 0.8 W of average output power. In addition, our simulations also showed that metalizing the edges of the bottom

plate lightguide, *i.e.*, the *x*-*z* plane, can further enhance η by ~2% and widen the acceptance angle by ±0.1°.

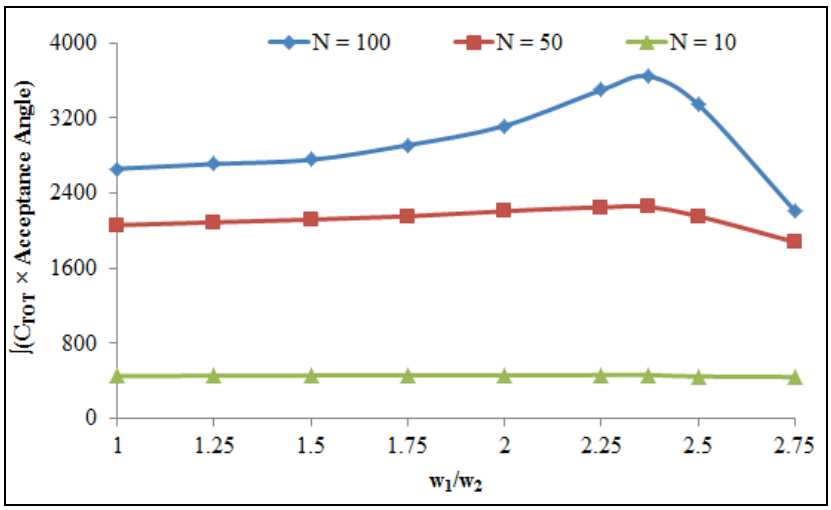

Fig. 2.9 Total area under the C_{TOT} –acceptance angle plot maximizes when the ratio of the widths of the plate is at around 2.37 for the 100 unit-cell system

Multiple cells: tapered geometry

C_{GEO} can be further increased by tapering the bottom plate lightguide. Tapering has been adopted to the TFSC by Karp et al. [8]. C_{GEO} of such design becomes:

$$C_{GEO,TAPERED} = \frac{A_{In}}{A_{Out}} = \frac{l \times (w_1 + w_2)/2}{w_2 \times t} \tag{2.5}$$

where, l is the length of concentrator, w_1 and w_2 are the two widths of the concentrator and t is the thickness of the plate. We optimized the tapering angle of the TFSC structure by integrating total area under C_{TOT}– Acceptance angle curve as shown in Fig 2.9. The maximum energy is obtained when the ratio of the widths of the plate is around 2.37.

Figure 2.10(a) shows the optimized design using tapered bottom plate lightguide for N = 100. The design parameters l, w_1, w_2, and t are 200, 100, 42.2, and 2.0 mm, respectively. C_{GEO} of this structure is 237, which is 2.37 times higher than that of the plain rectangular TFSC shown in Fig. 2.8(a). Figures 2.10(b) and 2.10(c) show the simulated η of the tapered TFSC as a function of the incidence angle on the x-z and y-z planes, respectively. The acceptance angle along these two plains for the tapered design is close to ±0.48° and ±9° and the FWHM angle along these two plains is close to ±1.1° and ±23°. Figure 2.10(d) shows the change in η and C_{TOT} as a function of N. The maximum C_{TOT} of this tapered TFSC increases to 81. It is more than double the C_{TOT} value attainable with the rectangular TFSC in the previous subsection. The total power at the output aperture for AM1.5 system is 6.84 W, which is almost comparable to rectangular TFSC even though the area of output aperture reduced by more than half.

While the increase came at the expense of the acceptance angle, the present FWHM angle (±23°) is still sufficient for covering approximately 60 (at the summer solstice) to 180 (at the winter solstice) minutes of daily solar cycle around noon in Washington, D.C. throughout the year [10], provided that the TFSC is mounted on a slow tracking system compensating the changes in the solar elevation angle. Even for dual-axis tracking, the wide acceptance angle will help lowering the required control precision and reduce the cost for solar tracking.

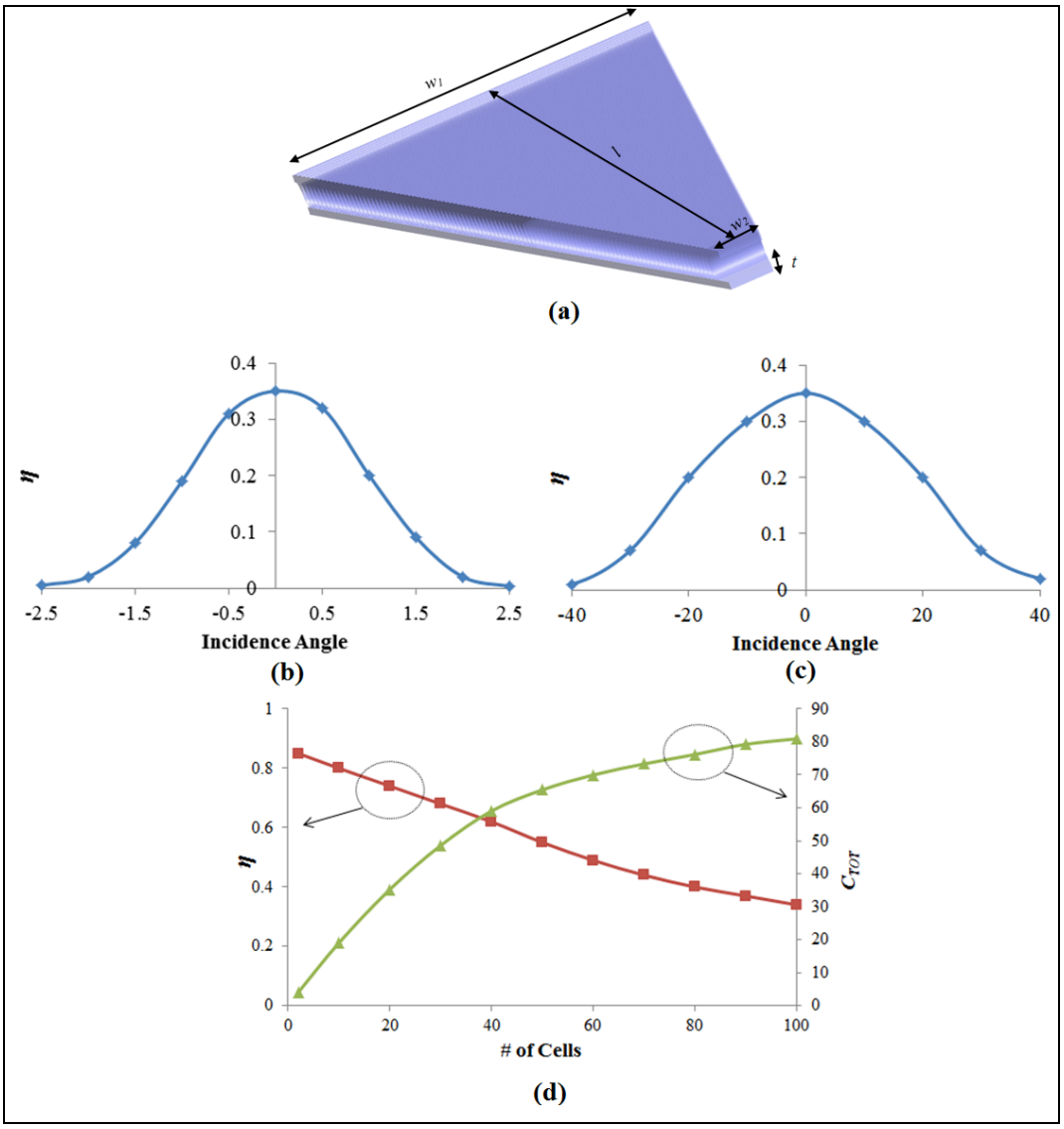

Fig. 2.10 (a) A 100-cell tapered TFSC. (b) And (c) show the simulated η plotted as a function of the incidence angle in the (b) *x*-*z* and (c) *y*-*z* planes of Fig. 2.3(a). (d) η and C_{TOT} as functions of the number of the unit-cells.

Discussion

In our work, performed under the assumption of realization with a polymeric material, the bio-inspired light redirection scheme enabled the design of a 20 cm-long, 1.1 cm-thick TFSC its with acceptance angle as wide as ±15° and FWHM angle of ±32° which is sufficient to cover

80~240 minutes of daily solar movement around noon year round in Washington, D.C., provided that the seasonal solar elevation changes were compensated for by an active tracking system. The total optical concentration factor of the TFSC, which considers both the ratio between the collection and reception areas and the optical loss arising from the concentration process, was computed to be 39. We also showed that the total optical concentration factor can be further increased to 81, at a slight penalty in the acceptance angle (6° on each side), by axially tapering the overall shape of the TFSC. These results are summarized in Table 2.2.

Table 2.2: Summary of the present TFSC's light collection performance

		Rectangular	**Tapered**
Acceptance Angle	*x-z*	±0.5°	±0.48°
	y-z	±15°	±9°
C_{GEO}		100	237
C_{TOT}		39	81

The remaining task is the prototype level fabrication of the proposed structure. Building two-layer structures connected by multiple lightguides with sub-millimeter thickness is challenging technically. Recent progresses in polymer-based micro fabrication, especially those relying on lost-wax molding [21,22], will be of great utility in the physical realization. The author's previous fabrication and AFM-based characterization results showed that surface roughness was in the range of 3.2±0.8 nm. The corresponding propagation loss was < ~3.5 dB/cm which is low enough to cover the sub-cm propagation required for the proposed structure. Improving this with methods that can offer greater surface quality, such as the non-contact, direct drawing [23] remains as a future work.

Conclusion

We present a novel thin and flat solar concentrator design. In conventional thin and flat concentrators relying mainly on microlens-reflector pairs for light redirection, it was challenging to improve the acceptance angle and the concentration factor simultaneously. We have overcome the conflict using a new light redirection scheme based on the pairing of a microlens and a lightguide, which was structurally inspired by the ommatidium of the insect's compound eye. By bending the lightguide gradually, we could smoothly convert the vertically impinging light into a laterally propagating ray. Then we minimized the interaction between the redirection elements and the light rays that are already redirected in order to reduce the light leakage loss. One of our optimized designs, in the form of a 20 cm-long, 1.1 cm-thick rectangular plate comprising 100 unit-cells, exhibited an acceptance angle of $\pm 15^{\circ}$ along with the optical concentration factor of 39. The factor can be increased to 81 through tapering of the geometry, at the expense of reduced acceptance angle ($\pm 9^{\circ}$).

Acknowledgment

This work was supported by National Science Foundation through ECCS-1147413.

References

[1] R. Winston, J. C. Minano, W. T. Welford, and P. Benitez, Nonimaging Optics (Academic, 2004).

[2] J. Chaves, Introduction to Nonimaging Optics (CRC, 2008).

[3] R. M. Swanson, "The promise of concentrators," *Prog. in Photovoltaics.*, **8**, 93-111 (2000).

[4] R. Winston and J. M. Gordon, "Planar concentrators near the étendue limit," *Opt. Lett.*, **30**, 2617–2619 (2005).

[5] T. Tamir and S. T. Peng, "Analysis and design of grating couplers," *Appl. Phys. A.*, **14**, 235–254 (1977).

[6] R. K. Kostuk and G. Rosenberg, "Analysis and design of holographic solar concentrators," *Proc. SPIE*, **7043**, 70430I (2008).

[7] J. H. Karp and J. E. Ford, "Planar micro-optic solar concentration using multiple imaging lenses into a common slab waveguide," *Proc. SPIE* **7407**, 7407–7411 (2009).

[8] J. H. Karp, E. J. Tremblay, and J. E. Ford, "Planar micro-optic solar concentrator," *Opt. Express*, **18**, 1122-1133 (2010).

[9] B. L. Unger, "Dimpled Planar Lightguide Solar Concentrators," Ph.D. dissertation, The Institute of Optics, University of Rochester, Rochester, NY (2010).

[10] Univ. of Oregon, Solar Radiation Monitoring Laboratory, Sun Path Chart Program, [Online] Available: http://solardat.uoregon.edu/SunChartProgram.html

[11] J. H. Karp, E. J. Tremblay, J. M. Hallas, and J. E. Ford, "Orthogonal and secondary concentration in planar micro-optic solar collectors," *Opt. Express*, **19**, A673–A685 (2011).

[12] J. Hallas, K. Baker, J. Karp, E. Tremblay, and J. Ford, "Two-axis solar tracking accomplished through small lateral translations," *Appl. Opt.*, **51**, 6117-6124 (2012).

[13] M. F. Land, "Visual Acuity in Insects," *Annu. Rev. Entomol.*, **42**, 147-177 (1997).

[14] D. G. Stavenga and J. H. van Hateren, "Focusing by a high-power, low-Fresnel-number lens: the fly facet lens," *J. Opt. Soc. Am. A*, **8**, 14-19 (1991).

[15] J. H. van Hateren, " Photoreceptors optics, theory and practice," *in Facets of Vision*, D. G. Stavenga, R. C. Hardie, Eds., Springer-Verlag, 74-89 (1989).

[16] R. C. Hardie, K. Vogt, and A. Rudolph, “The compound eye of the tsetse fly (Glossina morsitans morsitans and Glossina palpalis palpalis),” *J. Insect Physiol.*, **35**, 423-431 (1989).

[17] J. Kim, K. H. Jeong, and L. P. Lee, "Artificial ommatidia by self-aligned microlenses and waveguides," *Opt. Lett.*, **30**, 5-7 (2005).

[18] K. H. Jeong, J. Kim, and L. P. Lee, “Biologically inspired artificial compound eyes,” *Science*, **312**, 557-561 (2006).

[19] Schott, Optical glass data sheet, [Online] Available: http://www.schott.com/advanced_optics/us/abbe_datasheets/schott_datasheet_all_us.pdf

[20] K. Gawlik, C. Kutscher, and F. Burkholder, “Optical Efficiency Measurements of the SkyTrough Solar Collector”, National Renewable Energy Laboratory, (2010)

[21] J. Lee and J. Kim, "Elastomeric microwire-based optical gas flowmeter with stretching-enabled tunability in measurement range," *Opt. Lett.*, **36**, 3789-3791 (2011).

[22] J. Lee and J. Kim, “Fabrication of strongly anchored, high aspect ratio elastomeric microwires for mechanical and optical applications.” *J. Micromech. Microeng.*, **21**, 085016 (2011).

[23] K. Lee, H. C. Lee, D.-S. Lee, and H. Jung, “Drawing Lithography: Three-Dimensional Fabrication of an Ultrahigh-Aspect-Ratio Microneedle.” *Adv. Mat.*, **22**, 483–486 (2010).

CHAPTER 3

ELASTOMER BASED OPTO-THERMO-MECHANICAL ACTUATION FOR AUTONOMOUS, SELF POWERED LIGHT LEVEL CONTROL

Modified from paper published in *Applied Optics*

Rabin Dhakal and Jaeyoun Kim

Abstract

We present easy to fabricate MEMS cantilever lightguides structure with paraffin wax actuator to produce an autonomous, self-powered solar light controller. Infrared portion of the solar light is focused into the microchamber containing paraffin to cause its volume expansion and produce the pneumatic force. This force is translated to close the cantilever against the lightguide operating in the guiding mode and the visible light in the lightguide is leaked into the cantilever using principles of *f-TIR*. In the linear region of working we could produce more stable output power varying only by 0.012 (*rms*) when the input power was varied by 0.018 (*rms*) from the reference.

Introduction

As a major area of electricity consumption in residential and commercial sectors [1], indoor lighting has been the main target of renewable energy technologies, especially those based on solar power. Current solar-powered indoor lighting, however, is a two-step process in which sunlight is first converted into electricity through the photovoltaic effect and then converted back into light for illumination. With each conversion step less than 20% efficient, the overall conversion efficiency is inherently low at ~4% [2]. Delivering sunlight directly to

overhead lamp fixtures can greatly improve indoor lighting efficiency. Several such schemes based on lens/mirror combinations [3] and optical fibers [4] have already been demonstrated.

Making solar indoor lighting comfortable to human eyes, however, requires additional processes, since the light level must be kept constant and uniform through active control. A number of light control schemes have been developed over the past few years, which were based on thermal [5], pneumatic [6,7], or electrokinetic [8] principles and actuated by electric fields [9], magnetic fields [10], optical trapping [11], or electrowetting [12] mechanisms. These existing actuators, however, all require externally supplied control and power for their operations. Eliminating such requirements can greatly facilitate the deployment and maintenance of the actuators and the light controller based on them. Reports on such autonomous, self-powered light control schemes, however, have been scarce to date. In this work, we aim to realize an autonomous, self-powered light-level controller that adaptively redirects a part of the guided light through frustrated total internal reflection (*f-TIR*) utilizing heat-induced volumetric expansion of a phase-change material and the force produced by it.

Phase change material such as paraffin wax have been extensively used for thermal microactuation [13-17]. Paraffin wax is a mixture of saturated alka- nes and hydrocarbons with general formula C_nH_{2n+2}. It is in solid phase at room temperature and the melting temperature depends on the length of the carbon chain. When heated beyond the phase transition the paraffin wax under goes large volume expansion of up to 30% [18]. When cooled, the paraffin melt starts to coagulate by packing the molecules close together in ordered form. This crystallization of the paraffin leads to overall decrease in it volume. This increase and decrease in volume is used to produce forward and reverse stroke to actuate the MEMS device.

The autonomous, self-powered operation can be realized by utilizing a fraction of the lightwave itself, rather than the more conventional electrical or chemical heaters, to induce the required temperature increase. It is well-known fact that the visible regime accounts only for 47% of the energy in the ambient solar radiation and almost 46% is in the infrared (IR) regime [19]. Since indoor lighting requires only the visible portion, using the energy-rich IR portion as the power source for the thermal actuator would not affect the illumination level.

Device Design and Fabrication

Device design

Figures 3.1(a) and 3.1(b) schematically show the opto- thermal light-level controller and its operation principle. There are two light paths, one through the main light guide, and the other through the branching light guide. Sunlight will only light up the former. In normal circumstances, the lightwave will stay within the main light guide, as shown in Fig. 3.1(a), because the separation between the main and branching light guides is set to be wide enough to prevent *f-TIR* based coupling. In our design, the separation can be controlled by the actuator installed right below the branching light guide.

As shown in Fig. 3.1(b), the increase in the overall light level directly results in a matching increase in the level of light impinging upon the paraffin wax and causes its volume to change. By confining the paraffin wax in an elastic structure, we can translate the volume increase into mechanical actuation that will push the branching light guide onto the main light guide and reduce the separation between them. Gradually, the impact of *f-TIR* will kick in, and an increasing fraction of the light in the main light guide will be outcoupled into the branching

light guide. Judicious setup of the feedback system would lead to the realization of autonomous, self-powered light-level regulation. Note that our light control scheme does not rely on absorption of the propagating light, and the outcoupled light can be further utilized for other purposes, such as lighting of a different area.

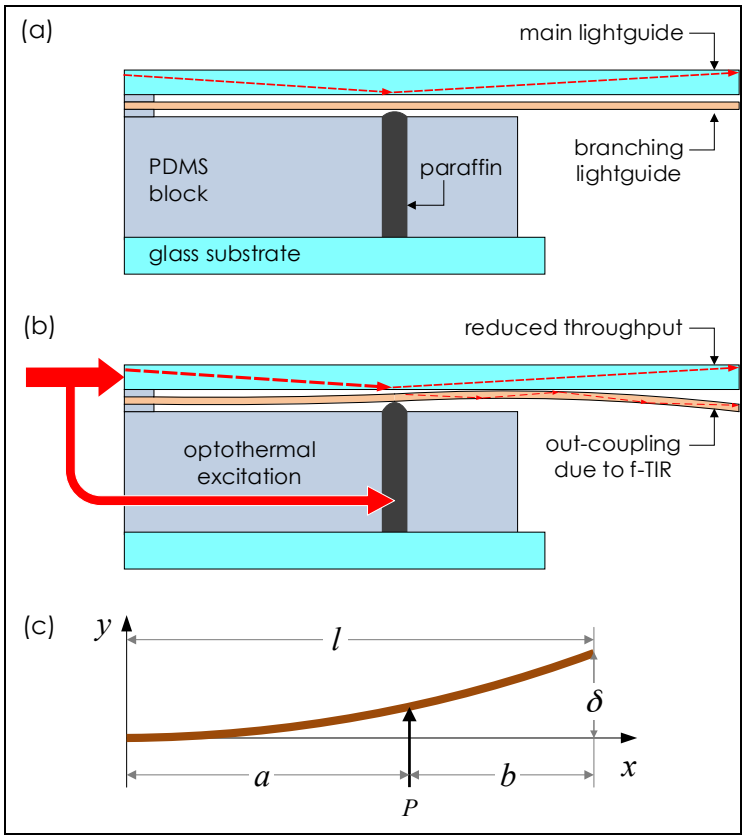

Fig. 3.1 Schematic diagram of the optothermal light-level control. (a) Normally, the branching lightguide is at its "open" position and the collected sunlight propagates only through the main lightguide. (b) Upon application of thermal excitation, the optothermal actuator pushes the branching lightguide towards the main lightguide, inducing frustrated total internal reflection (*f-TIR*) and out-coupling of light from the main lightguide into the branching lightguide. For autonomous, self-powered operation, the thermal excitation will be obtained from the collected sunlight itself. (c) Deflection of a cantilever upon application of force *P*.

We chose to implement the optothermal actuator using paraffin wax, which exhibits a relatively low melting point of 44°*C*-46°*C* (Sigma-Aldrich). To translate the volume change into actuation, we encased the material in a microchamber with its top opening covered with a thin elastomeric membrane. The excitation light will be focused onto the microchamber through a lens to simultaneously function as the control signal and actuation power source.

We made the main light guide with a 1 mm thick, 4×50 *mm*×4×50 *mm* microscope slide (n~1.49). The branching light guide was realized with a 65 *mm* long, 200 μm thick PET strip, so that it can function as an elastic cantilever. PET was chosen for its excellent transparency, high elasticity, and ease of machining. The two light guides are separated by 200 μm by a spacer made of poly(dimethylsiloxane) (PDMS), as shown in Figs. 3.1 and 3.3. By design, the two light guides maintain a "normally open" state with a 200 μm gap, as shown in Fig. 3.1(a). Under intense solar illumination, the paraffin wax undergoes thermal expansion, inflating the membrane to push the PET light guide toward the main light guide. We paid special attention to minimize the contact area between the two light guides, so that the light already outcoupled into the PET light guide would not be coupled back into the main light guide.

Modeling

To model the PET light guide, we adopted the Euler - Bernoulli beam model in which the total deflection δ of the cantilever depends on its geometry, the material's elasticity, and the applied force as [20].

$$\delta = \frac{Pa^2}{6EI}(3x - a) \tag{3.1}$$

where P is the actual force applied to the cantilever, E the elastic modulus of PET (~2.7 MPa [21]), I the moment of inertia, x the length of the cantilever at which the deflection is measured, and a the point of force application, as shown in Fig. 3.1(c). In our design, the cantilever has to undergo a 200 μm deflection to reach the main lightguide and initiate *f-TIR*. Therefore, from Eq. (3.1), the minimum force required to start the light-level control operation is ~0.04 N for $a > 5$ mm. This level of force can be readily provided by the paraffin actuator [26].

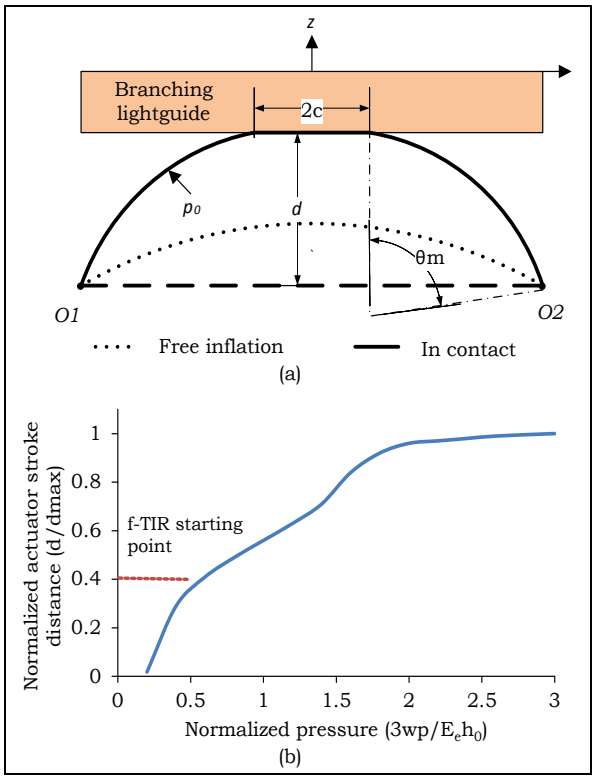

Fig. 3.2 (a) The change in the elastomeric membrane profile due to the expansion of the paraffin-wax inside the microchamber. (b) Normalized actuation stroke distance as a function of the normalized chamber pressure. The point at which the *f-TIR* process initiates is also marked.

Actuator contact point for our design is fixed at the middle of the main lightguide at a = 25 *mm*. With this actuation contact point, the minimum deflection of the branching lightguide for the *f-TIR* process to kick in is 0.4 times the maximum deflection at the end of main lightguide. This minimum deflection has to be covered by the paraffin actuator's stroke.

The expansion of the paraffin wax in the microchamber inflates the thin PDMS membrane as shown in Fig. 3.2(a). We used the nonlinear hyper-elastic theory to model the actuation [22]. A PDMS membrane (modulus of elasticity E_e ~2.05 *MPa* [23]) with a uniform thickness h_0 and width $2w$ is set at a distance d from the branching lightguide. Under a uniform excess pressure p_o, the membrane deforms showing a slope of θ_m at O1 and O2 as shown in Fig. 3.2(a). There are two phases. Initially, the membrane can be freely inflated. Then, it comes in contact with the lightguide. The height of the actuator stroke can simply be calculated from the simple geometry as:

$$d_z = w.\tan\frac{\theta_m}{2} \tag{3.2}$$

where the slope θ_m is dependent on the pressure p_o as:

$$p_0 = \frac{3h_0}{E_e w}\left[\theta_m - \frac{\sin^4\theta_m}{\theta_m^3}\right] \tag{3.3}$$

Figure 3.2(b) shows the change in the actuator's stroke distance as a function of the pressure p_o. The distance is normalized to the maximum distance d and the pressure is normalized as $3wp_o/E_eh_o$. The f-TIR kicks in when the normalized actuation stroke distance reaches 0.4 as indicated in Fig. 3.2(b). This minimum normalized pressure is the threshold limit for our design to work. The second phase arises when the membrane becomes in contact with the lightguide. The height of the actuator stroke is then fixed to d and any increase in pressure results in increase in the contact length c given as:

$$c = w - \frac{d}{\tan(\theta_m / 2)} \tag{3.4}$$

In this phase, the slope θ_m depends on p_o as:

$$p_0 = \frac{6h_0}{E_e d}\left[\lambda - \lambda^3\right]\sin^2\frac{\theta_m}{2} \tag{3.5}$$

where,

$$\lambda = 1 + \frac{d}{w}\left[\frac{\theta_m}{2\sin^2(\theta_m / 2)} - \frac{1}{\tan(\theta_m / 2)}\right] \tag{3.6}$$

The solution of Eqs. 3.4 and 3.6 suggests that the normalized contact area *c/w* reaches unity for the normalized pressure of 8.1. Since the actuation stroke distance attains the maximum value *d* at a much lower pressure, this increase in pressure can be utilized to reduce the distance between the two lightguide at microscale and to increase the *f-TIR* induced out-coupling. The out-coupling, however, saturates when the pressure reaches the upper limit as the two lightguide overlap each other over a long contact distance, allowing the light to be coupled back into the main lightguide.

Device fabrication

Figure 3.3 schematically shows the steps to fabricate the light-level controller. We first made a rectangular PDMS block and punched a 2×1 mm^2 hole into it to form the microchamber. The microchamber position corresponded to the required actuation contact point. Then we bonded the chamber to a glass substrate using oxygen plasma bonding. The supporting structure for the optothermal actuator was also made mainly of PDMS.

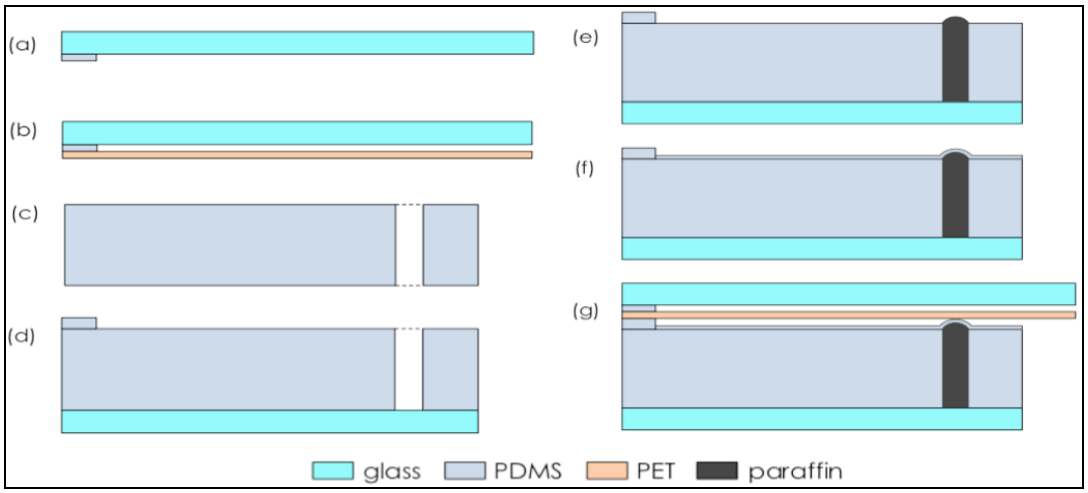

Fig. 3.3 Fabrication of the opto-thermo-mechanical light-level controller. (a) A PDMS spacer is attached to the main lightguide. (b) The PET branching lightguide is attached to the main lightguide to form a cantilever. (c) A hole is punched into a PDMS block to form a microchamber. (d) The PDMS block is plasma bonded to a glass substrate. A second PDMS spacer is attached on the top surface. (e) The microchamber is filled with paraffin composites. (f) A thin PDMS elastic membrane is attached to close the paraffin composite-filled microchamber. (g) Integration of the top and bottom parts.

Subsequently, we filled the microchamber with the optothermal material mix. We tested three different material compositions, as specified in Table 1, in terms of their suitability, response time, and device reliability. We confirmed that the melting point is at 44~46 *°C*. As an accelerant of the optothermal effect, we utilized graphite particles (Sigma Aldrich) as well. When filling the microchamber, we first heated the paraffin wax well beyond its melting point and then added the graphite particles to it, followed by a round of stirring. We then loaded the mixture in a syringe and injected it into the microchamber. Then the device was placed in vacuum for two hours to remove any possible air bubble. Then, we covered the microchamber's top opening with a 100 *μm*-thick PDMS membrane by pouring liquid PDMS over the top surface. Finally, the lightguide-cantilever structure was attached to the optothermal actuator using liquid-phase PDMS as an adhesive.

Table 3.1: Composition of phase change materials used in three different actuators

actuator type	phase-change material composition
A	pure paraffin
B	50:50 paraffin:PDMS
C	99:1 paraffin:graphite particle

Device Characterization

We characterized the performance of the optothermal actuator using two main performance metrics: actuation speed of the PET cantilever and outcoupling efficiency of the light from the main light guide. The actuation speed depends mainly on the temporal response of the paraffin wax to heating. We quantified it by measuring the time duration for the cantilever to fully close (closing time) or open up (opening time) the gap with the main light guide. The former was measured from the first application of heat to the moment the cantilever comes in contact with the main light guide. The latter was measured from the removal of heat to the complete cease of the out- coupling from the main light guide. For these measurements, we used the fastest actuators from the three groups in Table 1 as references.

For better estimation of temperature, we utilized a hot plate as the source of heat in this part. As the source of the input light to the main light guide and the heating light for the actuator, we used the NCL 150 variable light source with a 50 *W* halogen lamp. As shown in Fig. 3.4(a), the input light was delivered to the main light guide through a multimode optical fiber bundle and coupled into the main light guide with a microscope objective (Newport, M10×, 0.25 *NA*). The heating light was directly focused onto a 5 mm diameter spot on the sidewall of the PDMS microchamber using a biconvex lens (Newport), as shown in Fig. 3.4(b). Through preliminary

measurements, we confirmed that the light levels of the main light guide input and the heating light for the actuator change at the same rate. The output power was measured with an optical power meter (Newport, 2931-C).

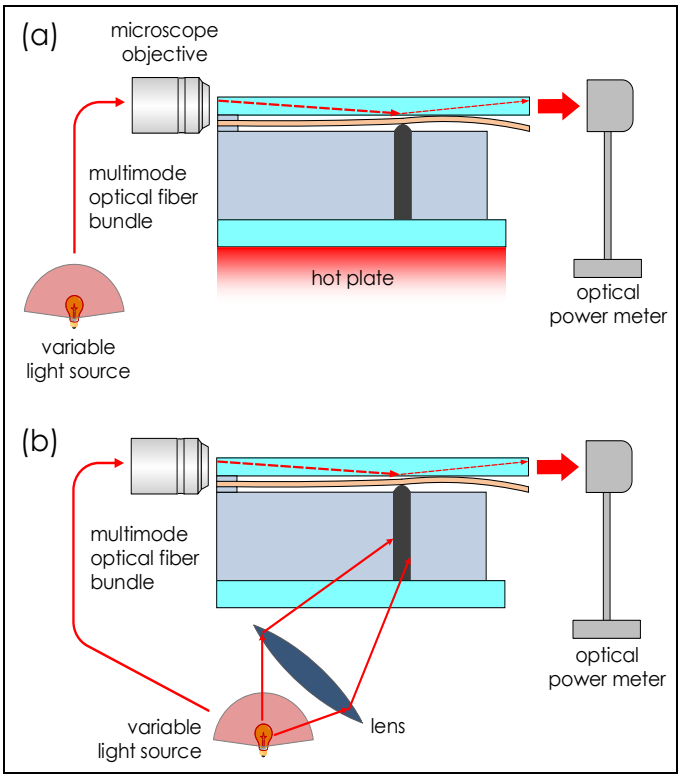

Fig. 3.4 Setups for (a) response time measurement and (b) autono- mous light-level control.

Device Characterization Results

Actuator response time

We measured the closing and opening time durations for all three actuator types in Table 1 as functions of the temperature. The results are given in Figs. 3.5(a) and (b). All three types of actuators were configured with the same actuation contact point (a = 25 *mm*). The temperature

values were directly read from the hot plate control panel. For all three actuator types, the opening and closing time values decreased monotonically as the applied temperature increased. Type C exhibited the fastest response. We attributed it to the graphite particles embedded in the paraffin matrix, which can function as an accelerator of heat conduction. Type B was the slowest due to the smaller volume fraction of paraffin. For the optical characterizations to follow, we mainly utilized Type C, the fastest one.

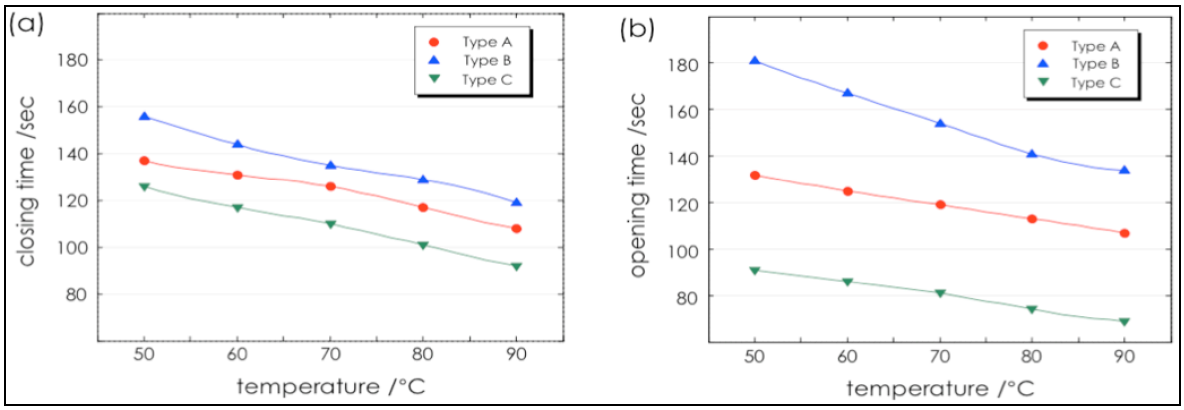

Fig. 3.5 Time durations required to (a) close and (b) open the cantilever in three different actuators.

Out-coupling characteristics under optical control

We then proceeded to characterize the impact of the optothermal actuation on the performance of the main light guide, both in terms of its through- put and response dynamics. Rather than directly applying heat with a hot plate, as in the previous subsection, we controlled the optothermal actuator optically, with the same light also used as the input light to the main light guide. In this subsection, however, the light levels of the input and the control lights were varied separately.

We first measured how the optothermal gap closing and the subsequent *f-TIR* affect the through- put of the main light guide by measuring the changes in the main light guide's output power as a function of the optical control power applied to the optothermal actuator. The fraction of the optical power out- coupled to the branching light guide was then estimated by comparing the light levels of input and output lights.

Figure 3.6(a) shows the results for a complete cycle. The fraction of the outcoupled light power started to increase as the control light power went beyond the threshold value of ~5 *mW*. Clearly the actuation process is not able to produce enough leverage at this stage. Then the interaction entered a quasi-linear regime. The increase in the control power produces an almost proportional change in the actuation force and leverage. This regime is essential as the operation point for the autonomous light level control. The saturation started as the control light power approached ~33 *mW*. This is due to the fact that the volume expansion of the paraffin wax is too small at this stage to produce any extra leverage. The out- coupling ratio reached ~17% at this point. A similar response is measured as the control light power de- creased from the saturation value to zero. When the temperature is decreased, the melted paraffin wax is generally supercooled and does not start to crystallize at the same temperature where the melting has started. This produces small hysteresis in the heating cooling cycle. The observed hysteresis was <0.4% at the center of the quasi-linear region. Note that the overall curve shape closely resembles the theoretical prediction in Fig. 3.2(b).

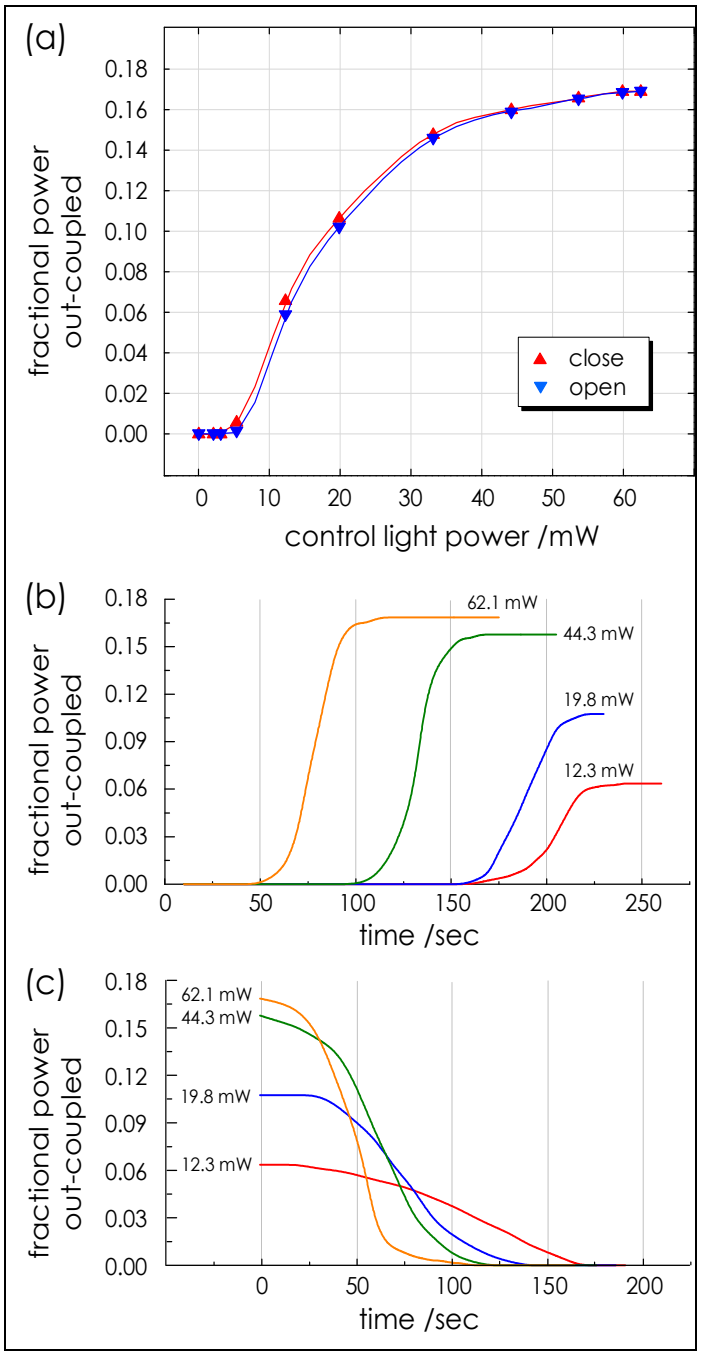

Fig. 3.6 (a) Fractional light power out-coupled from the main lightguide as a function of the optical control power. The measurement was taken over a complete cycle covering both closing and re-opening of the inter-lightguide gap. Note the curve's similarity to the theoretical prediction in Fig. 3.2(b). Temporal changes in the fractional out-coupled light power after (b) switch-on and (c) switch-off of the control light. Four different values of control light power were used.

We also measured the temporal responses of the throughput change upon switch-on and switch-off of the control light and plotted them in Figs. 3.6(b) and 3.6(c), respectively. The switch-on response exhibited three distinct operation regimes. The first is the initial flat region indicative of a thresholding. In this regime, the paraffin wax is not heated enough to start the actuation. It is followed by the quasi-linear regime in which the outcoupling increases with time. Eventually, the deflection of the branching light guide reaches its maximum, and the outcoupling begins to saturate, forming the third region. The switch-off response in Fig. 3.6(c) exhibits a similar set of three regimes. Beyond the initial flat regime below the threshold, the switch-on and switch-off responses exhibit similar time scales.

Autonomous light level control

Finally, we operated the device in the setup shown in Fig. 3.4(b) to test the feasibility of autonomous, self- powered light level control. We began by biasing the optothermal controller at the center of the quasi- linear region of the plot shown in Fig. 3.6(a), at which the controller exhibits the highest level of sensitivity and the ability to deal with the increase and decrease in the overall light level. Our bias point corresponds to 19.82 mW in the control light power in Fig. 3.6(a).

Then we varied the overall light level by 0.75% around the bias point and measured the changes in the main light guides' output light level to prove the feasibility of self-powered light level control. Such a small change in the input light level would lead to a slow actuator response because the resulting change in temperature and the heat transfer to and from the paraffin wax chamber become slower. Therefore we varied the input light by ~0.19% with a 12 min inter- val, as shown by the overall light level in Fig. 3.7. We measured the output light level at the end of

main light guide every 3 *min* to estimate the light outcoupling due to f-TIR, as shown in Fig. 3.7. The overall light level and the main light guide's output light level are normalized to their steady-state reference values.

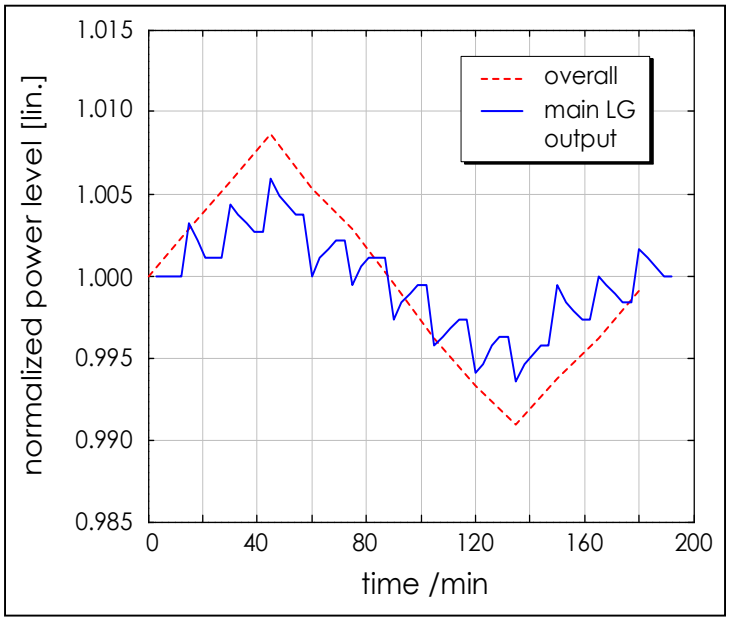

Fig. 3.7 Result of autonomous light-level control. The graph contrasts the level of the overall light, which was fed into the main lightguide (LG) and the optothermal controller, with that of the main LG's output. Both light-levels are normalized to its reference values to show that the controller continuously tries to bring the light-level back to its preset reference level.

The controller's output at the main light guide changes whenever the overall input light level changes. From the curves, it becomes evident that the controller continuously pushes the main light guide's output light level back to its reference level, even when the overall light level itself is in a gradual linear rise from the normal level. In the opposite situation, in which the overall light level dives below the reference level, the controller correctly tries to increase the main light guide's output light level as well. As a metric of the autonomous light level control,

we compared the root-mean-square (*rms*) changes of the two light levels. The input light level was at 0.999 (*rms*), and the corresponding output light level is at 0.992 (*rms*). We found that for the change in input light level by 0.018 (*rms*) from the reference, the corresponding change in the output light level at the steady state is only 0.012 (*rms*). The change in output light level is smaller due to the controlling action of our device.

Discussion

An autonomous self-powered light level controller can be realized using paraffin wax as the actuation material. The total actuator stroke and the response time of the controller turned out to depend strongly on the composition of the paraffin wax. In our case, we could attain an actuation stroke of ~200 μm using paraffin with its melting temperature in the range of 44°C–46°*C* and controlled by a focused sunlight. The response time of the actuator and the overall outcoupling of the light from the main light guide, however, can clearly be a technical issue.

A couple of factors turned out to affect the actuator in that aspect. First, the paraffin volume change- based actuation is often degraded by bubbles or voids in the microchamber, which reduce the total leverage produced by it. Second, the elastic membrane on top of the microchamber needs to get thinner through the development of a better sealing technique. The response time of the controller is directly dependent on the time required to elevate the temperature of the actuation material. This depends on the actuator design, control light level, and the total volume of paraffin. We have used 20 mm^3 of paraffin volume.

There are ample opportunities to reduce this paraffin volume and improve the response time of our controller with further structure optimizations. We ruled out the use of a longer polymer chain paraffin to produce increased volumetric expansion, as we need to compromise

the melting temperature and the response time. The light controller assembly can be housed indoors; therefore, the effect of ambient temperature on the performance of our device can be practically ignored.

Our device controls the light level when the input flux varies by 0.75% over the period of time at this stage. Instantaneous clouding on a typical day varies the ambient light level more than this within a short period of time. Therefore, the future work is to increase the scalability of our design. This can be employed by assembling a multiple number of the devices or by simply enlarging them.

Conclusion

In this work, we realized an opto-thermo-mechanical actuator and utilized it to control the power level of light being delivered through a light guide by translating the actuation into the frustration of total internal reflection. In accordance, we designed and implemented a light level controller consisting of two light guides, one main and the other branching, and configured an all-optical closed-loop control, so that a change in the overall light level would operate the actuator and counteract the change by adjusting the degree of frustrated total internal reflection. The opto-thermo-mechanical actuator exhibited a quasi- liner response regime, which is essential for realizing such a control scheme. Since the overall light functions as the heating light for the actuator as well, the controller can be deemed autonomous and self- powered. We demonstrated that the controller could level the output light level of the main light guide closer to the reference value. The change in input light level by 0.018 (*rms*) from the reference is leveled to more stable output by smaller change of 0.012 (*rms*) at the output.

Acknowledgement

This work was supported by the National Science Foundation through ECCS-1147413.

References

[1] http://www.eia.gov/tools/faqs/faq.cfm?id=99&t=3.

[2] J. D. Muhs, "Hybrid solar lighting doubles the efficiency and affordability of solar energy in commercial buildings," *CADDET Energy Efficiency Newsletters*, 6-9 (2000).

[3] L. M. Fraas, W. R. Pyle and P. R. Ryason, "Concentrated and piped sunlight for indoor illumination," *Applied Optics*, **22**, 578-582 (1983).

[4] M. A. Dugway and R. M Edgar , "Lighting with sunlight using sun tracking concentrators," *Applied Optics*, **16**, 1444 (1977).

[5] P. Domachuk, H. C. Nguyen, B. J. Eggleton, M. Straub, M. Gu, "Microfluidic tunable photonic band-gap device," *App. Phys. Let*t., **84**, 1838-1840 (2004).

[6] C. Grillet, P. Domachuk, V. Ta'eed, E. Magi, J. A. Bolger, B. J. Eggleton, L. E. Rodd, J. Cooper-White, "Compact tunable microfluidic interferometer," *Opt. Express*, **12**, 5440-5447 (2004).

[7] W. Song and D. Psaltis, "Pneumatically tunable optofluidic 2 × 2 switch for reconfigurable optical circuit, " *Lab Chip*, **11**, 2397-2402 (2011).

[8] P. Mach, T. Krupenkin, S. Yang, J. A. Rogers, "Dynamic tuning of optical waveguides with electrowetting pumps and recirculating fluid channels," *App. Phys. Lett.*, **81**, 202-204 (2002).

[9] M. W. Haakestad, T. T. Alkeskjold, M. D. Nielsen, L. Scolari, J. Riishede, H. E. Engan, A. Bjarklev, "Electrically tunable photonic bandgap guidance in a liquid-crystal filled photonic crystal fiber," *IEEE Photonics Technol Lett.*, **17**, 819-821 (2005).

[10] H. E. Hong, C. S. Chen, K. L. Fang, S. Y. Yang and J. J. Chieh, "Tunable optical switch using magnetic fluids,"*Appl. Phys. Lett.*, **85**,23, 5592-5594 (2004).

[11] P. Domachuk, M. Cronin-Golomb, B. J. Eggleton, S. Mutzenich, G. Rosengarten, A. Mitchell, "Application of optical trapping to beam manipulation in optofluidics," *Opt. Exp.*, **19**, 13, 19, 7265-7275 (2005).

[12] W. Song and D. Psaltis , "Electrically tunable optofluidic light switch for reconfigurable solar lighting, " *Lab Chip*, **13**, 2708-2713 (2013).

[13] R. H. Liu, J. Bonanno, J. Yang, R. Lenigk and P. Grodzinski, "Single use, thermally actuated paraffin valves for microfluidic applications," *Sens Actuators B Chem.*, **98**, 2–3, 328–336, (2004).

[14] J. M. Park, Y. K. Cho, B. S. Lee, J. G. C. Lee and C. Ko, "Multifunctional microvalves control by optical illumination and its application in centrifugal microfluidic devices" *Lab Chip*, **7**, 5, 557–564 (2007).

[15] J. S. Lee, S. Lucyszyn (2007a) "Design and pressure analysis for bulk micromachined electrothermal hydraulic microactuators using a PCM," *Sens. Actuators A Phys.*, **133**, 2, 294–300 (2007).

[16] S. Svensson, G. Sharma, S. Ogden, K. Hjort and L. Klintberg (2010) "High pressure peristaltic membrane micropump with temperature Control," *J. Microelectromech Syst.*, **19**, 6, 1462–1469 (2010).

[17] G. H. Feng and Y.C. Chou Y-C "Fabrication and characterization of thermally driven fast turn-on microvalve with adjustable backpressure design," *Microelectron Eng.*, **88**, 2, 187–194 (2011).

[18] E. T. Carlen, C. H. Mastrangelo, "Surface micromachined paraffin actuated microvalve," *J. Microelectromech. Sys.*, **11**, 5, 408-420 (2002).

[19] A. J. W. Whang, Y. Y. Chen, B. Y. Wu, "Innovative design of cassegrain solar concentrator system for indoor illumination utilizing chromatic aberration to filter out ultraviolet and infrared in sunlight," *Solar Energy*, **83**, 8, 1115–1122 (2009).

[20] http://www.matweb.com/reference/tensilestrength.aspx

[21] K. W. Oh and C. H. Ahn, " A review of microvalves," *J. Micromech. Microeng.*, **16**, 5, R13-R39 (2006).

[22] A. Srivastava, C-Y. Hui, "Large deformation contact mechanics of long rectangular membranes. I. Adhesionless contact," *Proc. R. Soc. A*, **469**, 0424, (2013).

[23] I. D. Johnston, D. K. McCluskey, C. K. L. Tan and M. C. Tracey, "Mechanical characterization of bulk Sylgard 184 for microfluidics and microengineering," *J. Micromech. Microeng.*, **24**, 35017-35024 (2014).

CHAPTER 4

TRANSFER MOLDING PROCESS FOR NANOSCALE PATTERNING OF POLY-L-LACTIC (PLLA) ACID FILMS

Modified from paper published in *Proc. of SPIE, Microfluidics, bioMEMS and medical microsystems XIV*

Rabin Dhakal, Akshit Peer, Rana Biswas and Jaeyoun Kim

Abstract

Nanoscale patterned structures made of biomaterials exhibit great potential in the fabrication of functional bio-structures. In this paper, we report cost-effective, rapid, and highly reproducible soft lithographic transfer-molding techniques for creating periodic micro and nano-scale textures on Poly (L-lactic acid) (PLLA) surface. These artificial textures can increase the overall available surface area, which is key attribute for several biological functions including cell growth, surface hydrophobicity and drug delivery. In this paper we describe nanoscale pattering of the PLLA films using double replication techniques, whereby the polycarbonate (PC) master pattern is first transferred to the PDMS mold and then the PDMS pattern is transferred to the PLLA films through drop-casting as well as nano-imprinting methods. The ensuing comparison studies revealed that the drop-cast PLLA allows pattern transfer at higher levels of fidelity, enabling the realization of nano-cup and nano-cone arrays with pitch down to ~700 *nm*. We also develop a drug loading method on the nano-patterned structures of PLLA film by coating it with *rapamycin* (sirolimus) and make biodegradable drug-eluting stents.

Introduction

Periodically patterned structures have imparted profound impacts to diverse scientific disciplines. In physics, chemistry, and material science, artificially engineered photonic crystals have demonstrated unprecedented abilities to control the propagation of photons. In the field of biomaterials, it is of great interest to explore how such periodically patterned structures control diverse biological functions, primarily by varying the available functional area and allowing the creation of controlled cellular environments, engineering of functional tissues and development of better drug delivery systems. This is very promising to address the therapeutic shortcomings in the treatment of diseased or damaged tissues and organs [1].

For clinical application, we need to recreate the biomimetic three-dimensional (3D) cell culture platforms and precisely control the temporal and spatial component of cell's microenvironment [2]. In vivo cellular microenvironment contains critical information rich cues embedded in the extracellular matrix [3], neighboring cells, soluble and tethered cytokines, and metabolites that regulate the cell survival, adhesion [4], migration [5] and differentiation [6]. Also, in the area of drug delivery, the size and shape of the drug carriers of micro and nanoscale can affect its circulation time, distribution and cellular internalization [7]. Therefore, the micro and nanoscale technologies have become the essential tool to address the existing challenge in tissue engineering and drug delivery system by fabricating functional polymeric material to control cell behaviors, develop improved scaffolds for tissue engineering and improve the drugs pharmacodynamics parameters.

Biocompatible and/or biodegradable materials are the preferred material choice for these biomedical applications. Most of the polymer biomaterials degrade through hydrolysis and can

be highly controlled [8]. Among them, the most widely used is poly (L-lactic acid) (PLLA) [9-11], poly (D,L-lactic acid) (PDLLA) [12-14], and poly (lactic-co-glycolic acid) (PLGA) [15- 17]. PLLA is a prototypical material actively in use to construct drug eluting coronary stents as well as templates for cell growth. Some examples includes, PLLA microgrooves with a spacing of 10-20 μm and depths of ~1.4 μm or greater were very effective in promoting cell adhesion and Schwann cell alignment within the grooves [13,14]. The findings are of great significance for regeneration of nerve cells on artificial scaffolds. Reactive ion beam etching along with compression molding and solvent casting were utilized to fabricate these microscale grooves [13]. In an analogous study, nano-scale pillars of 400 nm and 700 *nm* diameter, and pitch of ~700 *nm* and 1300 *nm*, respectively, were fabricated on PLLA substrates using the micro-transfer molding technique which utilizes lithographically patterned Si wafers as the master pattern [8]. Studies on human tissue growth on these patterned surfaces found that the fibroblast adhesion was enhanced on the patterned surfaces but its proliferation was greater on the smooth surface, especially after one day. The underlying complex mechanisms shaping the cell's interaction with nanoscale-textured surfaces are under active study [10,11].

In this work, we have been mainly motivated by the need to study the impact of nanoscale surface patterns made on biodegradable polymers for its potential application in drug eluting stents application. We have explored cost-effective, rapid, and highly reproducible ways to create nano-scale periodic textures on biodegradable surfaces. We chose PLLA as the main material and aimed to alter its surface properties by coating a layer of *rapamycin* (sirolimus), an immunosuppressant drug used to reduce rejection in organ transplantation. We demonstrate that micro-transfer-molding-based soft lithographic techniques can provide rapid and reproducible methods for nano-scale surface patterning for biodegradable polymers.

Experiment

Materials

We obtained the polycarbonate (PC) master patterns from Microcontinnum Inc. The PC master patterns are periodically patterned with nano- cups and nano-cones with pitch of ~750nm in triangular lattice. Such master patterns and imprint stamps at customizable pitch and feature size can also be commercially purchased from vendors [18] without the need of in-house nanofabrication. The polydimethylsiloxane (PDMS) pre-polymers (the elastomer base and the matching curing agent) were purchased from Dow Corning (Sylgard 184). The PLLA film was prepared by casting 5% solution of PLLA (Synthecon Inc., Houston, TX, MW 85,000-160,000) in chloroform. The PLLA surface was coated with 1% solution of sirolimus (LC Laboratories, Woburn, MA) in ethanol. All the solvents used were HPLC-grade and were procured from Fisher Scientific.

Fabrication

The fabrication process of nanoscale patterns on the PLLA films consists of double replication method. First, we transferred the patterns from the PC master to the PDMS using replica-molding techniques and second, we replicated PDMS mold on the PLLA surface using transfer-molding processes.

In the first step, we prepared the PDMS mold by mixing the elastomer base and curing agent in ratio of 10:1 (*w/w*). The mixture was thoroughly degassed in vacuum till all the air bubbles disappears and directly poured into the polycarbonate master on a petri-disc. The PDMS was left to cure at room temperature for ~48 *hours* followed by heating on a hotplate at 65°*C* for

~12 *hours*. The PDMS mold has the inverse of the PC patterns when peeled off from the PC master.

In the second step, we used the patterned PDMS mold as a master to imprint the PLLA film using transfer-molding techniques. Two different approaches were taken in the replication process. The first one, as shown in Fig. 4.1, is the drop- casting process used to replicate the nano cups on the PC master. Same technique was used to replicate the nano-cone. Here, 1% PLLA solution on chloroform was directly drop-cast on the PDMS pattern. The PLLA film was then solvent annealed at room temperature for ~12 *hours* and subsequently gently peeled off by the tweezers.

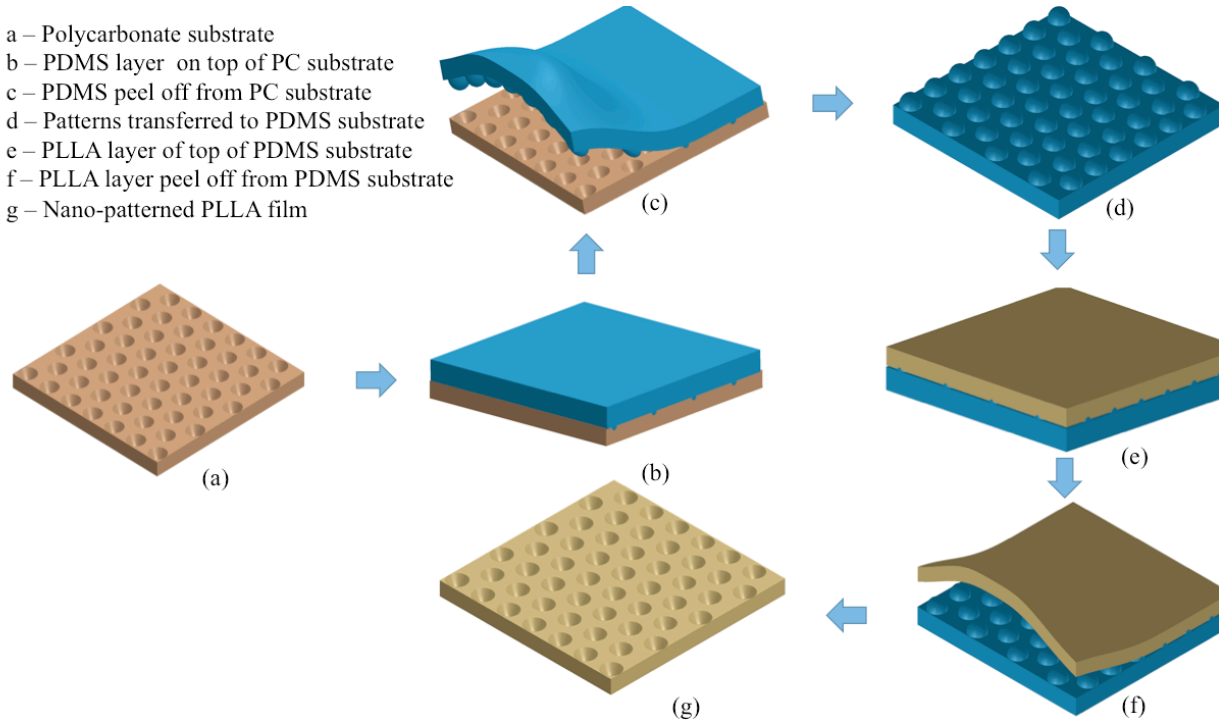

Fig. 4.1 Nanoscale patterning of PLLA film using drop casting process.

In the second approach, PDMS pattern was directly imprinted onto the PLLA film by nano imprinting process as shown in Fig. 4.2. For this, PLLA film was first prepared on the glass substrate by spin coating (at 500 *rpm* for 60 *seconds*) and dried in room temperature for ~12 *hours*. Then the PDMS mold (imprinter) was placed on the PLLA film with the pattern side facing the PLLA surface. Another glass substrate of same dimensions was used to cover the other side of PDMS. The two glass substrates were pressed against each other using two binder clips and the whole assembly was placed on a hot plate set at 100°*C* for 35 *minutes*. The glass transition temperature (T_g) for the PLLA film is ~60 °*C*. Therefore the patterns in the PDMS can be fully imprinted into the PLLA surface at a temperature (100°*C*) higher than T_g. Finally the PLLA film was gently peeled off from the glass substrate by the tweezers.

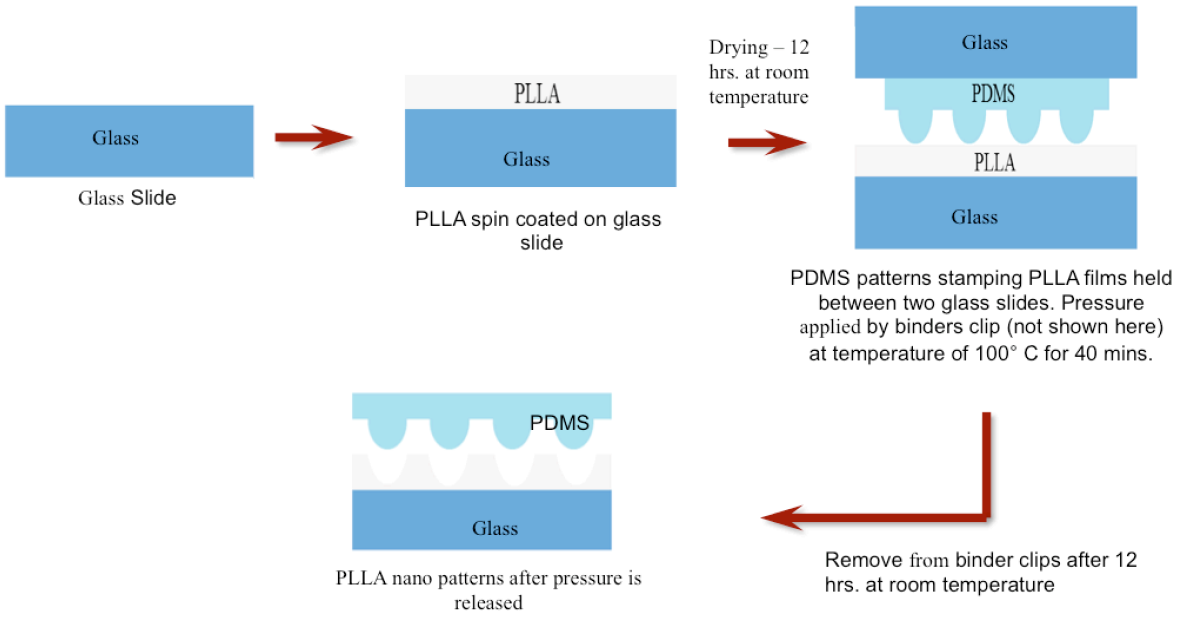

Fig. 4.2 Nanoscale patterning of PLLA film using nano imprinting process.

The nano-patterned PLLA film was coated with 125 $\mu g/cm^2$ of sirolimus. For this we first weighed the 2 cm x 1 cm PLLA film (*w1*) and then coated it with 1% sirolimus solution in ethanol. The final weight of PLLA film was maintained at (*w1* + 250 μg) after loading sirolimus. We employed five different coating methods to determine the optimum coating process and produce uniform, conformal coating of sirolimus as described below.

i. Drop casting: We directly drop casted 25 μl of 1% sirolimus solution on the 2 *cm* x 1 *cm* PLLA surface area. The film was dried at room temperature first and then air-dried using dry N_2 gas.

ii. Spin coating: We prepare the nano patterned PLLA film on the glass substrate. For this we placed a glass slide of same size as PLLA pattern immediately after drop casting PLLA solution on the PDMS mold. The glass substrate with PLLA patterns was then peeled off from the mold and weighed to take the initial weight. Sirolimus solution was spin coated (600 *rpm*, 40 *secs*) and dried at room temperature followed by N_2 blow. We then took the final weight and repeated the spin coating and drying process if necessary.

iii. Brush coating: We used gentle stroke of a paintbrush to coat the PLLA surface. The film was dried at room temperature, weighed and the coating process was repeated until we get the weight right.

iv. Spray coating: We used spray nozzle to make micron size sirolimus solution aerosols and brought the PLLA surface in front of the nozzle. The film was dried at room temperature, weighed and the coating process was repeated until we get the weight right.

v. Pre-coating: We drop casted 25 μl of 1% sirolimus solution on the PDMS mold and dried it at room temperature. The PLLA solution was drop casted on the sirolimus coated PDMS mold. Sirolimus is highly soluble in chloroform and when we peel off the PLLA film after drying, the sirolimus is coated on its surface.

Results and Discussion

Pattern replication

We verified the fidelity of the pattern transfer to PDMS and PLLA surface and sirolimus coating on the PLLA surface, using FEI Quanta 250 FE - scanning electron microscope (SEM) and nanoscope atomic force microscope (AFM).

Figures 4.3(a) and 4.3(b) shows the optical microscope image (Lecia) of the PC master and PDMS mold replicated from the PC master respectively. Figure 4.3(c) and 4.3(d) shows the AFM image of PC master showing triangular lattice of pitch ~700 *nm*, base radius of 250 *nm* and height/depth of ~ 240 *nm* for both nano-cups and cones. These values confirms with the company specifications. Figure 4.3(e) and 4.3(f) shows the SEM micrograph of the PDMS mold replicated from the PC master showing nano-cups and nano-cones respectively. We see some wrinkles on edges of the PDMS nano-cups and nano-cones surface in the SEM images. These wrinkles are caused by the electron beam damage during SEM imaging and increase with the exposure time. We confirmed this by taking the AFM images of the PDMS nano-cone as shown in Fig. 4.3(g). The section analysis of this AFM image in Fig. 4.3(h) shows the PDMS mold has triangular lattice with pitch of ~ 700 nm. The nano-cones has the base radius of 250 nm and height of ~190 *nm*. We achieved reproducible, rapid and high fidelity replication of nanoscale

patterns in the PDMS mold.

Figures 4.4(a) and (b) show the SEM micrograph of the PLLA nano-cups made by drop-casting and nano- imprinting methods, respectively. Similarly, Fig. 4.4(c) and (d) shows the SEM micrograph of the PLLA nano-cones made by drop-casting and nano-imprinting method respectively. All four images show regular triangular lattice arrays of nano-cups and nano-cones with a pitch of ~700 *nm* and base radius of ~250 *nm*. The PLLA films replicated by drop-casting process, as shown in Fig. 4.4(a), and Fig. 4.4(c) illustrate clearly resolved features with very high fidelity, preserving the shape and height of nano patterned features. The PLLA solution can straightforwardly enter the grooves of the PDMS nano patterns patterns to produce nearly exact replication.

The shallower and less-resolved features shown in Fig. 4.4(b) and 4(d) were produced by nano-imprinting method. The quality of nano-imprinting depends on the ability of film to redistribute itself within the grooves of the PDMS mold. Two crucial parameters for this is the imprinting temperature and pressure applied. We used improvised nano-imprinting setup using hot plate and binder clips. We can attribute this less resolved PLLA feature to the insufficient and non-uniform pressure applied from the binder clips and possible spatial temperature variation on the PLLA surface, which will redistribute material rather non-uniformly around the PDMS grooves. The probable solution for this problem is to use improved imprinting setup and low molecular weight PLLA that has low viscosity. The high pattern fidelity with drop casting method suggests that, this process can be extended to smaller feature sizes. Figure 4.4(e) and 4.4(f) are the AFM section analysis image of PLLA patterns fabricated by using drop-casting method. The triangular lattice array has the pitch of ~ 700 *nm*, base radius of ~ 250 *nm* and height/depth of ~ 185 *nm* and is same as the PDMS master mold.

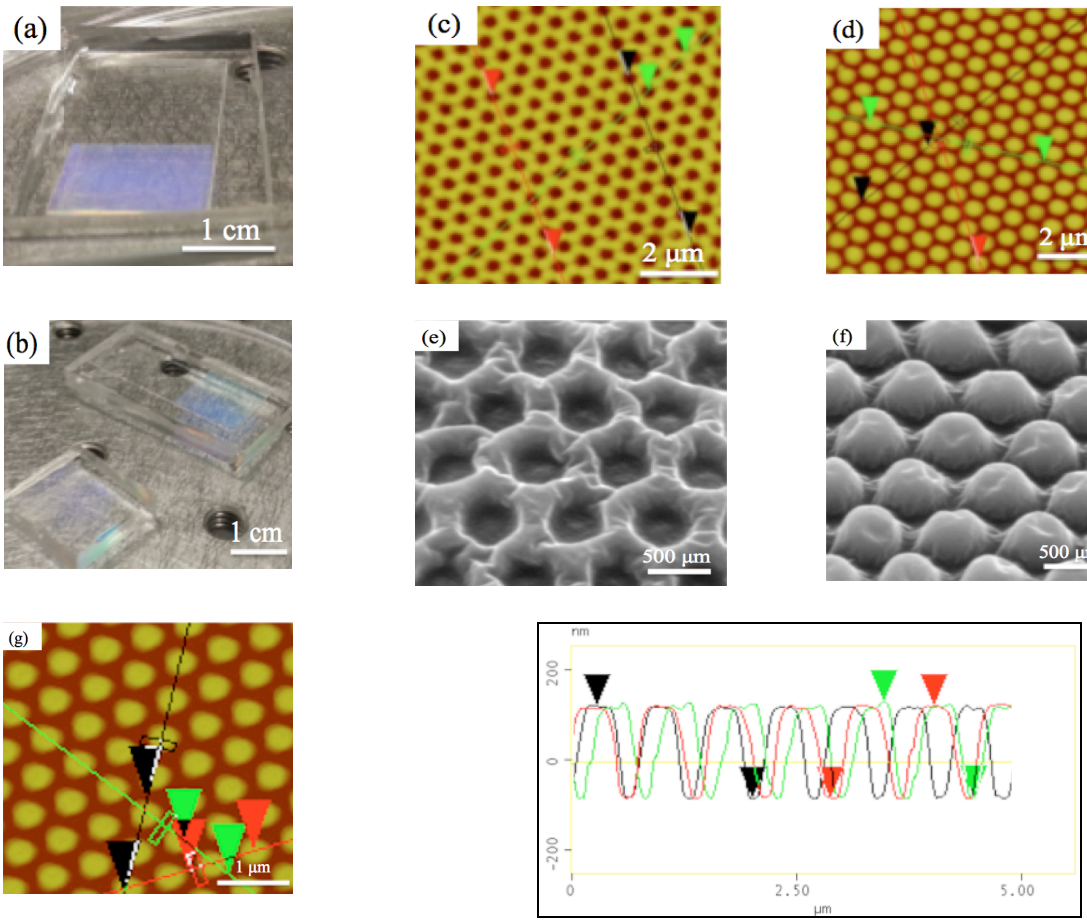

Fig. 4.3 Images of PDMS replication from PC master. (a) Optical image of the PC master and (b) Optical image of PDMS mold replicated from PC master. The optical image shows clear diffraction patterns confirming presence of patterns. (c) AFM image of the PC master with nano-cups and (d) AFM image of PC master with nano-cones. (e) SEM micrograph of PDMS mold with nano cups and (f) SEM micrograph of PDMS mold with nano-cones. Figure (e) and (f) are the inverse of Fig. (d) and (c) respectively. (g) AFM image of PDMS mold with nano-cones. (h) Section analysis of AFM image in Fig. (g) showing pitch ~ 700 *nm*, height of cone ~ 190 *nm* and base radius of the cone ~ 250 *nm*. Scale bar: 1 *cm* for Fig. (a) and (b), 2 *µm* for Fig. (c) and (d), 500 *nm* for Fig. (e) and (f) and 1 *µm* for Fig. (g).

Drug coating on nano-patterned PLLA

We coated the nano-patterned PLLA films with 125 $\mu g/cm^2$ of immunosuppressant drug, sirolimus, using five different coating techniques.

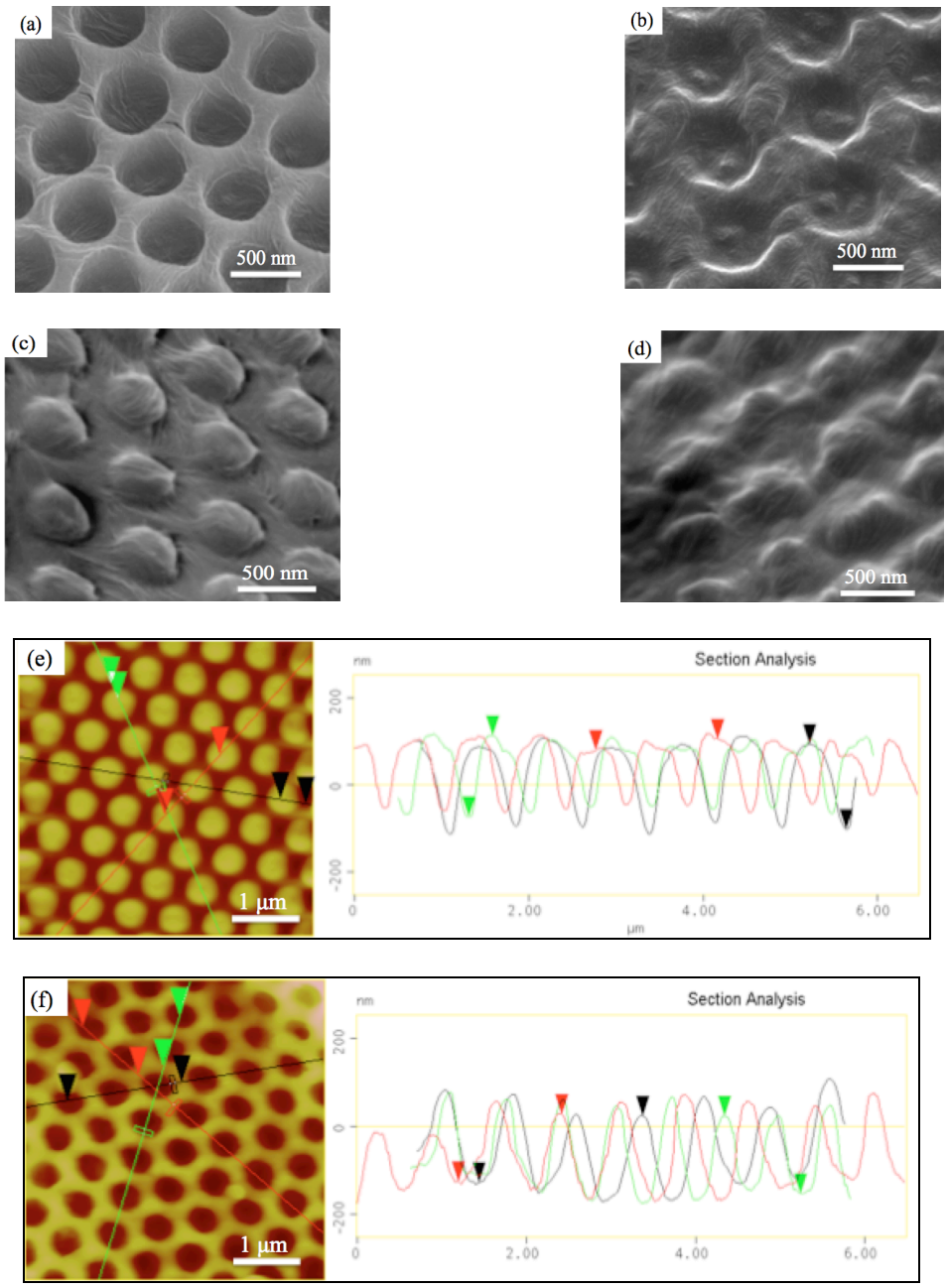

Fig. 4.4 PLLA replications form the PDMS mold. (a) SEM micrograph of the PLLA nano-cups from drop casting process and (b) SEM micrograph of the PLLA nano-cups from nano-imprinting method. (c) SEM micrograph of PLLA nano-cones from drop casting method and (d) SEM micrograph of PLLA nano-cones from nano-imprinting method. Drop casted process yield clearly resolved nano-patterns. AFM image and section analysis of PLLA nano-patterns using drop casting method for (e) nano-cones and (f) nano-cups. We can see triangular lattice nano-patterns with pitch of ~700 *nm*, base radius of ~ 250 *nm* and average height/depth of the feature ~ 185 *nm*. This value is same as the patterns in PDMS mold we saw in Fig. 4.3. Scale bar: 500 *nm* for Fig. (a), (b), (c) and (d) and 1 *µm* for Fig. (e) and (f).

The amount of drug was carefully measured using microbalance. Figure 4.5 shows the SEM micrographs of the PLLA nano-cups with same amount of drug coated using 1% sirolimus solution in ethanol by (a) drop casting, (b) spin coating, (c) brush coating, (d) spray coating and (e) pre-coating. Sirolimus is not chemically bonded to the PLLA surface, but it adheres to the surface with weak van der Walls interaction making it ideal for use in drug eluting devices. We observed that drop casting and spraying method produces micron size sirolimus balls on the surface as shown in Fig. 4.5(a) and (d) respectively. This is due to accumulation of run off of the sirolimus solution towards the center of the film during the drying process.

Similarly, the sirolimus coated using the spin coating process produced non-uniform coating over the patterns as shown in Fig. 4.5(b). We see uncoated patches in between heavily coated area due to uneven PLLA surface to begin with.

The brush coating produces shallow yet clearly visible depressions of nano-cups arrays as shown in Fig. 4.5(c). We confirmed this by the AFM section analysis image as shown in Fig. 4.5(f). We can clearly see the triangular lattice of pitch ~ 700 *nm*, the depth of the cups has significantly decreased to an average value of ~70 *nm*. The pre-coating produces clear patterns of sirolimus coated PLLA nano-cups as shown in Fig. 4.5(e).

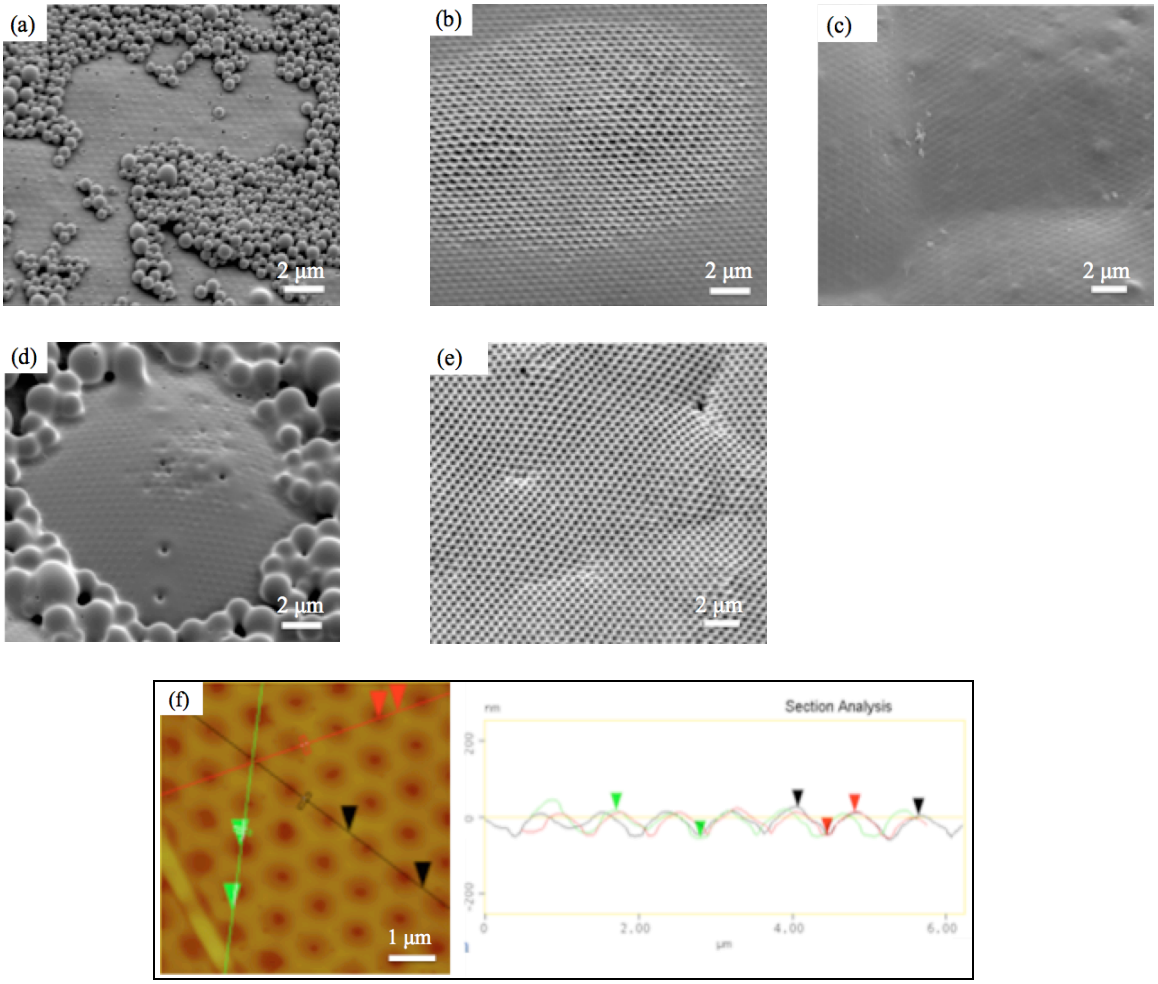

Fig. 4.5 Sirolimus coating on the PLLA nano-cups patterns using different coating process. (a) Drop casting, (b) Spin coating, (c) Brush coating, (d) Spraying and (e) Precoating. (f) AFM section analysis image of brush coated PLLA nano-cups patterns. Scale bar: 2 *µm* for Fig. (a), (b), (c), (d) and (e) and 1 *µm* for Fig. (f).

Hydrophobicity of patterned PLLA

The wetting behavior and effective contact area are critical factors to the interaction between the nano-patterned surface and its liquid-phase ambience. We investigated the changes in the surface characteristics of the PLLA due to the nano-patterning and drug coating by performing contact angle measurements on both the un-patterned and patterned PLLA samples before and after the *sirolimus* coating. We used a microliter syringe to position a droplet of

deionized water on the PLLA film on a glass slide and captured the frontal image using an optical microscope. The contact angle was acquired by processing the images using open source software *ImageJ*. The contact angle measurement results are summarized in Table 4.1.

Table 4.1: Contact angle measurements on control, nanocup, and nanocone patterned PLLA surfaces before and after *sirolimus* coating.

Pattern	Control	Nano cup	Nano cone
Uncoated	87°	106°	116°
Coated	77°	76°	76°

The contact angle has increased in the nano-patterned substrates (Table 4.1), imparting greater hydrophobic character to the patterned surfaces. The increase in the contact angle can be explained through Cassie-Baxter equation, which states that increasing the surface roughness increases the contact angle with the compound surface [18]. For a two-component liquid-air system, the Cassie-Baxter equation dictates that:

$$\cos\theta_c = f_1(\cos\theta_1 + 1) - 1 \tag{4.1}$$

where θ_c is the effective contact angle, and θ_1 the equilibrium contact angle of component 1 with area fraction f_1 of the liquid-air interface. Nano-patterning the PLLA surface will increase the area fraction f_1 of the liquid (water) with the film, thus inducing the patterned film to exhibit a higher level of hydrophobicity in comparison with the flat one. The contact angle for the coated PLLA surfaces is less than the uncoated surfaces because the conformal coating fills the nano-

cups and nano-cones to some extents, decreasing the depth (height) of the nano-cups (nano-cones).

PLLA tube fabrication

The nano-patterned PLLA films can easily be rolled into tubular forms. These PLLA tubes with patterns on the inner side can be used as scaffolding structures for cell culture and framework for fabricating coronary stents. For this, we wrapped the nano-patterned PLLA films around a cylindrical tube and joined the edges by dissolving it with chloroform using a fine brush. Figure 4.6(a) shows the optical microscope image of the PLLA tube with patterns on the inner side. The diameter of the tube was ~2 *mm* and the length was ~1 *cm*. We investigated the quality of the chloroform joint of the tube using SEM. Figure 4.6(b) shows that the joint region was limited to ~100 *μm* of the PLLA tube's inner surface. The chloroform vapors formed in ambience while joining the two areas has slightly degraded the pattern quality around the joint region.

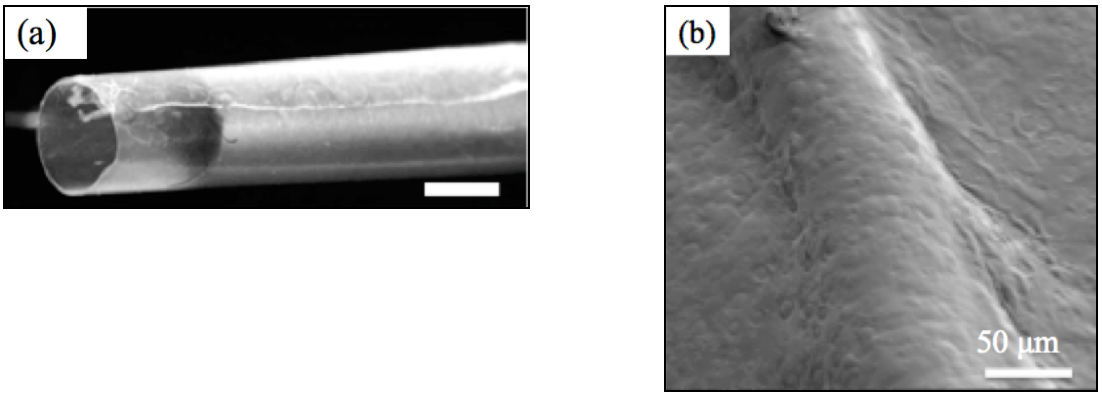

Fig. 4.6 (a) Optical microscope image of PLLA tube and (b) SEM micrograph of the nano-cups patterns in the tube joint area. Scale bar: 2 mm for (a) and 50 μm for (b)

Conclusion

We developed cost-effective, rapid, and highly reproducible ways to transfer periodic nano-patterns onto the surface of PLLA films. The patterned PLLA film can be easily rolled to produce PLLA tubes with nano-patterns on the inner surface. Micro-transfer molding techniques based on solution drop-casting can reliably produce nano-scale features on the PLLA surface. The contact angle measurement showed a 36° increase in contact angle for the nano-patterned surface in comparison to the un-patterned surface, showing that the patterned surface is more hydrophobic. The patterned surface was loaded with a therapeutic drug rapamycin using the brush-coating technique. We believe that all these new techniques will be of great use for future fabrication and utilization of nano-textured biocompatible polymer structures.

Acknowledgements

This research is supported by the National Science Foundation grants CMMI-1265844 and ECCS-0954845. We thank W. Straszheim from The Materials Analysis and Research Laboratory (MARL) of Iowa State University for assistance with scanning electron microscopy.

References

[1] R. Lange, J. P. Vacanti, "Tissue engineering," *Science*, **260**, 920-926 (1993).

[2] H. Naderi, M. M. Matin, A. R. Bahrami. "Review paper: Critical issues in tissue engineering: Biomaterials, cell sources, angiogenesis, and drug delivery systems," *J. Biomater. Appl.*, **26**, 383–417 (2011).

[3] R. O. Hynes, "The extracellular matrix: Nnot just pretty fibrils," *Science*, **326**,1216-1219 (2009).

[4] B. Geige, J. P. Spatz, A. D. Bershadsky, "Environmental sensing through focal adhesions," *Nat. Rev. Mol. Cell Bio.*, 10, 21-33 (2009.

[5] R. J. Petri, A. D. Doyle, K. M. Yamad, "Random versus directionally persistent cell migration," *Nat. Rev. Mol. Cell Bio.*, **10**, 538-549 (2009).

[6] A. Dolatshahi-Pirouz, M. Nikkhah, K. Kolind, M. R. Dokmeci, A. Khademhosseini, "Micro- and nanoengineering approaches to control stem cell-biomaterial interactions," *J. Funct. Biomater.*, **2**, 88-106 (2011).

[7] R. A. Petros, J. M. DeSimone, "Strategies in the design of nanoparticles for therapeutic applications," *Nat. Rev. Drug. Discov.*, **9**, 615-627 (2010).

[8] J. Borenstein, "Comprehensive Microsystems", *Elsevier*, **2**, 2, 2100-2105 (2007).

[9] K. R. Milner and C. A. Siedlecki, "Submicron poly (L-lactic acid) pillars affect fibroblast adhesion and proliferation," *J. Biomed. Mater. Res. A*, **82**, 1, 80-91 (2007).

[10] Y. Zhu, C. Gao, Y. Liu, and J. Shen, "Endothelial cell functions in vitro cultured on poly (L-lactic acid) membranes modified with different methods," *J Biomed. Mater. Res. A*, **69**, 3, 436-443 (2004).

[11] F. Badique, D. R. Stamov, P. M. Davidson, M. Veuillet, G. Reiter, J. N. Freund, C. M. Franz and K. Anselme, "Directing nuclear deformation on micropillared surfaces by substrate geometry and cytoskeleton organization," *Biomaterials*, **34**, 12, 2991-3001 (2013).

[12] P. M. Davidson, H. Özçelik, V. Hasirci, G. Reiter and K. Anselme, "Microstructured Surfaces Cause Severe but Non-Detrimental Deformation of the Cell Nucleus," *Adv. Mater.*, **21**, 35, 3586-3590 (2009).

[13] S. Shi, X. H. Wang, G. Guo, M. Fan, M. J. Huang and Z. Y. Qian, "Preparation and characterization of microporous poly (D, L-lactic acid) film for tissue engineering scaffold," *Int. J Nanomedicine*, **5**, 1049-1055 (2010).

[14] G. E. Rutkowski, C. A. Miller, S. Jeftinija and S. K. Mallapragada, "Synergistic effects of micropatterned biodegradable conduits and Schwann cells on sciatic nerve regeneration," *J. Neural Eng*., **1**, 3, 151-157 (2004).

[15] L. Moroni, and L. P. Lee, "Micropatterned hot-embossed polymeric surfaces influence cell proliferation and alignment," *J. Biomed. Mater. Res. A*, **88**, 3, 644-653 (2009).

[16] G. Vozzi, C. Flaim, A. Ahluwalia and S. Bhatia, "Fabrication of PLGA scaffolds using soft lithography and microsyringe deposition," *Biomaterials*, **24**, 14, 2533-2540 (2003).

[17] S. H. Hsu, C. Y. Chen, P. S. Lu, C. S. Lai and C. J. Chen, "Oriented Schwann cell growth on microgrooved surfaces," *Biotechnol. Bioeng.*, **92**, 5, 579-588 (2005).

[18] A. B. D. Cassie, S. Baxter, "Wettability of porous surfaces," *Trans. Faraday Soc.*, **40**, 546-551 (1944).

CHAPTER 5

NANOSCALE PATTERNING OF BIOPOLYMERS FOR FUNCTIONAL BIOSURFACE AND CONTROLLED DRUG RELEASE

Modified from paper submitted in *Nanoscale*

Rabin Dhakal, Akshit Peer, Jaeyoun Kim and Rana Biswas

Abstract

We compare the rates of drug release from nano-patterned and flat biodegradable polymer surfaces, and observe significantly lower release rates from the nano-patterned surfaces. Specifically, we nano-pattern poly (L-lactic acid) (PLLA), a biodegradable polymer frequently used for fabricating drug-eluting coronary stents, through micro-transfer molding and solvent casting and investigate the nano-pattern's impact on the release of *sirolimus*, an immunosuppressant agent, coated on the PLLA surface using high performance liquid chromatography/mass spectrometry. We find that PLLA surfaces nano-patterned with 700 *nm*-pitch nano-cup or nano-cone arrays exhibit drug release rates significantly lower (~25-30%) than that of the flat surface, which is counter-intuitive given the nano-pattern-induced increase in their surface areas. Based on diffusion and meniscus curvature minimization analyses, we attribute the decreased drug release rate to the incomplete wetting of the nano-patterned surface. These results provide new insights on how surface nano-patterning of biomaterials can functionalize the surface and tailor the release kinetics of therapeutic agents coated on it for controlled drug elution.

Introduction

Periodically patterned structures in biopolymers with controlled topography and surface chemistry have found applications in diverse biomedical applications. The periodic patterns form templates or scaffolds on the polymer surface and can be used to control the position, growth of cell and subsequent functions such as adhesion, orientation, migration differentiation, proliferation and protein synthesis [1-4]. We find several example of the cell growth and motility function in the field of biomedicine such as, migration of leukocytes mediates phagocytic and immune responses, migration of fibroblasts, vascular endothelial cells, and osteoblasts contributes to wound healing and tissue regeneration and tumor cell migration is essential to metastasis [5]. Also, tissue growing and engineering its shape with 3D scaffold will help replace painful transplant and/or autograft procedure.

Micro and nano-patterned biopolymer has also found application in the drug delivery system and control. The rate, time and location of the release of drugs inside the human body have great impact in the therapeutic efficacy as well as any unwanted local or systematic side effects. For optimal treatment result, we need to control the drug release profile by regulating the drug concentration inside the therapeutic window thereby preventing overdosing or no efficacy [6]. Patterned polymer surface can be used to design drug release profile using diffusion, forced bolus flow or continuous release process to have sustained or pulsatile drug release as shown in Fig. 5.1 [7, 8].

There is a great interest in nanoscale surface patterning of biodegradable polymers such as poly (L-lactic acid) (PLLA) [9-12], poly (D,L-lactic acid) (PDLLA) [13-15] or poly (lactic-co-glycolic acid) (PLGA) [16-17]. Recent studies have shown that such nano-patterned materials and their fabrication techniques are playing crucial roles in the development of biomedical

systems [9-10]. Human tissue growth experiments on these patterned surfaces revealed that the fibroblast adhesion was enhanced on the patterned surfaces although its proliferation was lower when compared with the smooth surfaces, especially after one day [15]. The underlying mechanisms of the cell-substrate interaction on nanoscale-patterned surfaces, including the characterization of the deformation of the cell nucleus, are under active study.

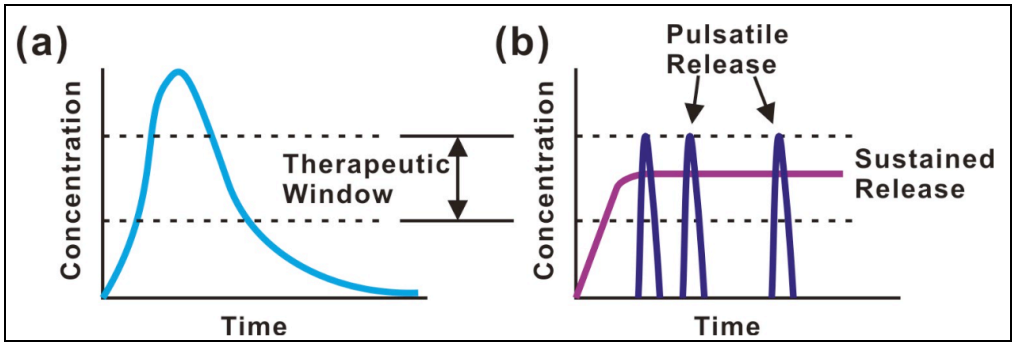

Fig. 5.1. Drug concentration as a function of release time showing (a) conventional drug release profile and (b) sustained release vs. pulsatile release (from Ref. [8])

PLLA has been frequently adopted for the realization of drug eluting stents in cardiac therapy. The stent is inserted into a blocked coronary artery through a balloon catheter and then subsequently expanded to re-open the artery. Stents provide mechanical framework in the artery and prevent its narrowing (stenosis) [18]. The major concerns of the metallic or plastic stents are that they might induce varying degree of thrombogenesis (blood clotting), fibrosis (formation of excess fibrous tissue) and hyperplasia (cell proliferation). Also, restenosis usually occur within 3-6 months after coronary intervention [19-21]. This limit the clinical need for stent after that time making biodegradable stents an ideal alternative [22]. To alleviate thrombosis, polymer-based stents loaded with anti-clotting drugs, to be eluted into the blood stream gradually, have

been introduced. The critical factor is the rate at which the coated drug is eluted. The ability to control and slow down the drug release rate has been in high demand. In this work, we show that we can lower the drug release rate through nano-patterning of the PLLA surface.

To evaluate the impact of nano-patterning, we first establish simple and reproducible ways to create periodic nanoscale textures on the PLLA surface. We then measured the drug release rate from these nano-patterned PLLA surfaces and compared the results with that of the flat, unpatterned control. The patterned surfaces show a remarkably slower release over a period of ten days in comparison to the control surfaces. We attribute the slower release to the nano-patterning-induced incomplete wetting of the surface, which demonstrates strong potential for morphological, not chemical, control of drug release rate.

Experimental

Nano-patterned PLLA film fabrication

We started with master pattern consisting of a periodic array of nano-cups or nano-cones with a sub-micron pitch of ~700 *nm* in a triangular lattice on a polycarbonate (PC) substrate (Microcontinnum Inc., MA). Each nano-cup (nano-cone) has radius of ~ 250 *nm* in and depth(height) of ~ 250 *nm*. The inverse of this pattern was transferred to a polydimethylsiloxane (PDMS) mold through replica molding. For this, we mixed the PDMS elastomer base and curing agent (Sylgard 184, Dow Corning) in 10:1 *w/w* ratio, degased and then poured it directly onto the nano-patterned master PC substrate. The PDMS mold was cured at room temperature for ~48 *hours* and subsequently heated on a hotplate at 65°*C* for ~12 *hours*, and finally peeled off from the master substrate. This PDMS mold was used to create surface nano-patterned PLLA films by

solvent casting. We prepared the PLLA solution by dissolving PLLA (Synthecon Inc., Houston, TX, MW 85,000-160,000) in HPLC grade chloroform. The PLLA solution was then directly drop-cast on the PDMS mold and the resulting film was dried at room temperature for 12 hours. The dried PLLA film was then peeled off from the PDMS mold. The details of the fabrication process are described in Chapter 4.

Drug coatings on PLLA

To study the drug elution characteristics we selected sirolimus (rapamycin) (LC Laboratories, MA) as the coating material since it is an immunosuppressant agent frequently used with coronary stents to prevent stent rejection by the human body. A solution of 1% sirolimus (by weight) was prepared in HPLC grade ethanol [23], which is an excellent solvent for sirolimus but does not affect the underlying PLLA substrate [24]. The nano-cup and nano-cone patterned PLLA surfaces were conformally coated with 125 $\mu g/cm^2$ of sirolimus with a fine brush and dried at room temperature. The samples were weighed in a microbalance before and after the coating process for measuring the same amount of drug (125 $\mu g/cm^2$) on all samples.

Drug release and measurement

The drug elution study was done for the control and patterned PLLA surfaces. The PLLA substrate has same surface area (2 *cm* x 1 *cm*) and coated equal amount of drug (250 μg). We immersed the one control and two patterned PLLA films in separate vials with 5.5 mL phosphate buffer solution (PBS) at room temperature. Sample solutions, 100 µL each, were drawn from the vials at a series of pre-determined times over an eight-day period with a syringe, resulting in 15 samples for each set or a total of 45 samples for one control and two patterned sets. Each sample

was stored in a separate vial, at 4°C until the measurement. The amount of phosphate buffer solution remaining in the vial decreases only < 2% for each sample drawn and thereby does not adversely affect the drug release kinetics.

High Performance Liquid Chromatography

High performance liquid chromatography is a technique to separate compounds in solution sample. This is achieved by passing the sample dissolved in solvent (the mobile phase) through a column packed with adsorbent material (stationary phase) under pressure. The rate of migration of the compounds depends on its interactions with the stationary and mobile phases as they move through the column. The most common interaction mechanism is dispersion, which contributes to hydrophobic interaction. We can broadly divide this into two separation modes based on polarity of the compound. Non-polar compounds are separated using normal phase chromatography. Here the stationary phase is highly polar (e.g. silica gel) and the mobile phase is non-polar (e.g. n-hexane), thereby the polar substances are retained for longer in the column. Reverse of this process is called reverse phase chromatography and applicable to separate polar compounds. In this case the stationary phase is non-polar (e.g. n-octadecylsylil-moieties) and the mobile phase is polar (e.g. methanol). Our compound of interest, sirolimus (shown in Fig. 5.2 [25]), is a polar organic compound and we have to use reverse phase chromatography for the efficient separation. We decided to use, mixture of methanol (80%) and water (20%) with a few drops of acetic acid for mobile phase.

HPLC system consists of mobile phase reservoir, pump, injector, separation column, detector and data acquisition system as shown in Fig. 5.3. The sample solution is injected into

the HPLC column along with continuous flow of the mobile phase. Eventually each component of the samples is eluted in narrow band on the recorder.

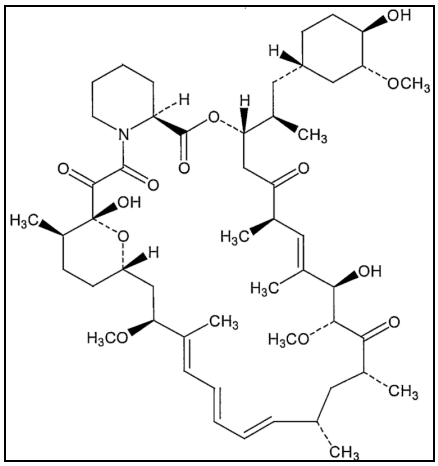

Fig. 5.2 Sirolimus compound structure (from Ref. [25])

We utilized the Agilent Technologies 1100 Series advanced high-performance liquid chromatography (HPLC) facility equipped with a SUPELCOSIL^{TM} LC-18 25 cm x 4.6 mm column (at the W.M. Keck Metabolomics Laboratory in Iowa State University), to measure the amount of *sirolimus* released. The 4-pump HPLC system was equipped with a thermostat-controlled auto-sampler/injector coupled to an Agilent Technologies Mass Selective Trap SL detector integrated with a nano-flow electrospray ion source and an atmospheric pressure chemical ionization source.

For our measurement, we used each test sample, 10 μL of the phosphate buffer solution and injected it into the HPLC column. The column separates the drug molecule and sends it to the electrospray ion source mass spectrometer (MS) to measure the concentration of *sirolimus* in the sample. We analyzed the entire batch of samples at the same time in the HPLC setup to

minimize calibration errors. To reduce statistical fluctuations and establish error bars for drug release, HPLC measurements for each sample were performed in triplicate. The sample vials were also kept at 4°C during the HPLC measurement.

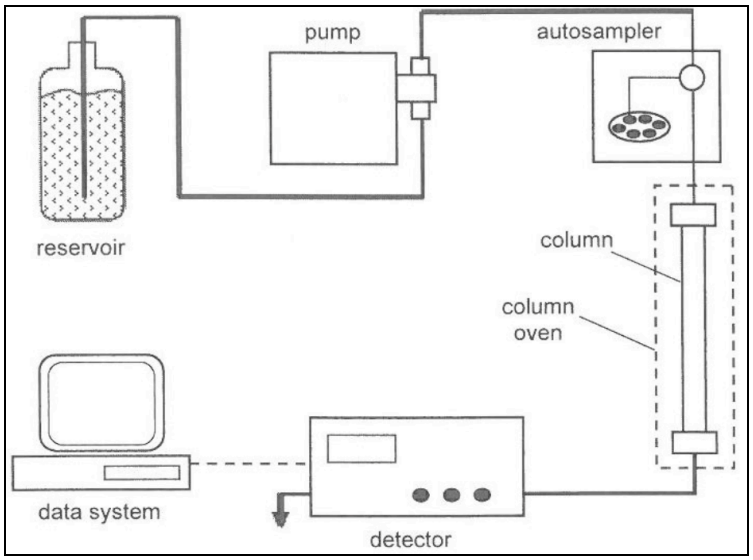

Fig. 5.3 HPLC system diagram (from Ref [26])

Results and Discussion

PLLA patterns replication and drug coating

We observe excellent fidelity of the nanoscale patterns on the PLLA film prepared by solvent casting process as shown in Fig. 5. 4 (a) and (b). The nano-cups (nano-cones) are arrayed in a triangular lattice with a ~700 *nm* pitch and base radius ~ 250 *nm*. To further confirm the fidelity of the solvent cast pattern transfer process, we performed atomic force microscopy (AFM) scans of the resulting PLLA nano-cup (Fig. 5.4(c)) and nano-cone (Fig. 5.4(d)) surfaces. The height/depth of ~ (180 -190) *nm* and shape of the PDMS patterns are very closely replicated

in the PLLA nano-patterns array which exhibits a similar depth/height. It implies that the PLLA solution directly cast on the PDMS mold has filled the grooves of the PDMS pattern almost completely, thus resulting in a total replication.

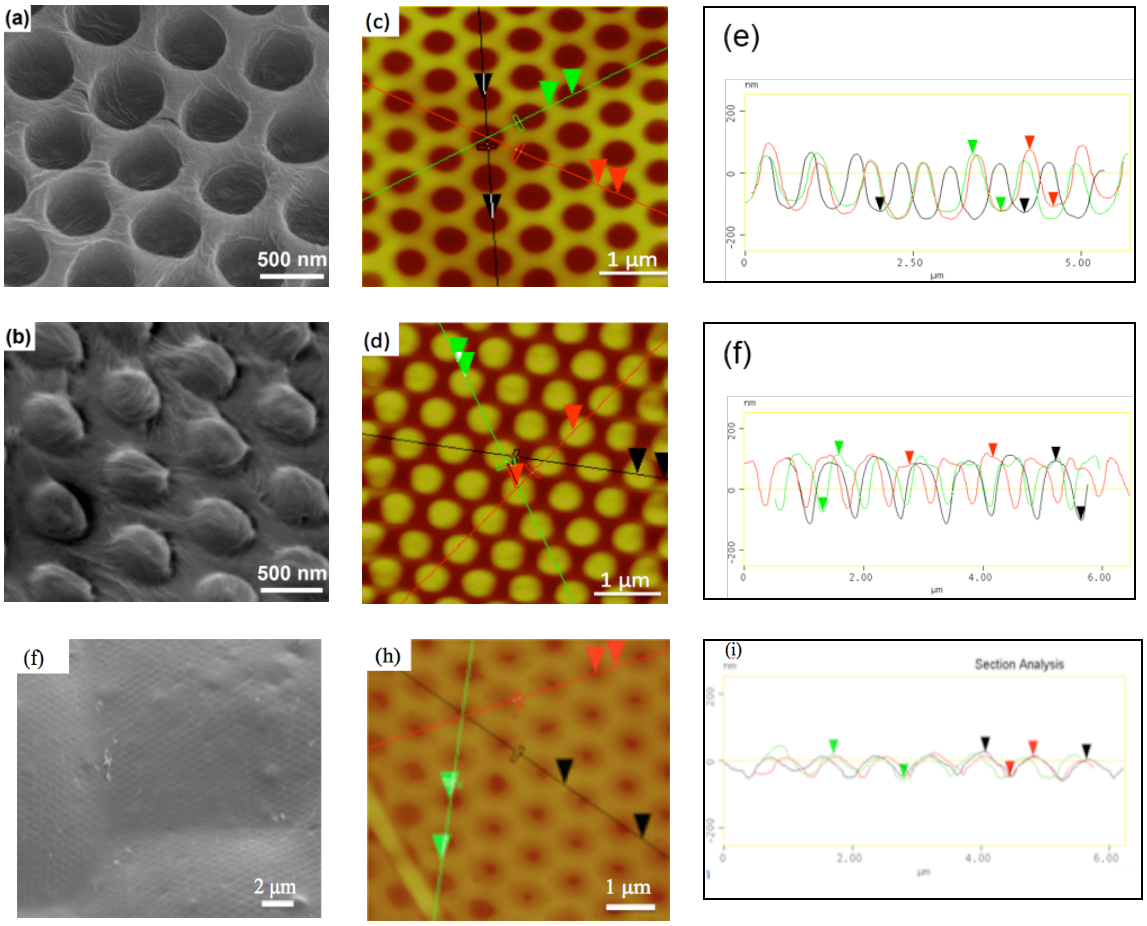

Figure 5.4. The surface of the PLLA films patterned with ~700 *nm*-pitch nanoscale arrays. SEM images of uncoated (a) nano-cups and (b) nano-cones are paired with AFM images (c) and (d) and the section profiles in (e) and (f), respectively. The nanocups exhibit an average depth of 182 *nm* and the nanocones an average height of 186 *nm*. Scale bar is 500 *nm* for (a) and (b) and 1 *µm* for (c) and (d). SEM images of sirolimus coated (a) nano-cups paired with AFM image (h) and section profiles in (i).

Figure 5.4 (f) shows the SEM image of the 1% PLLA nano-cups coated with 125 $\mu g/cm^2$ of sirolimus. Sirolimus is not chemically bonded to the PLLA surface, but it adheres to the surface with weak van der Walls interaction making it ideal for use in drug eluting devices. The brush coating produces shallow yet clearly visible depressions of nano-cups arrays. We confirmed this by the AFM section analysis image as shown in Fig. 5.4 (g) and (h). We can clearly see the triangular lattice of pitch ~ 700 *nm*, the depth of the cups has significantly decreased to an average value of ~70 *nm*.

Nanoscale patterning of the PLLA film increase its hydrophobicity due to change in its surface characteristics. This is because the nanoscale patterning will increase the area fraction of the liquid (water) with the film thus inducing the patterned film to exhibit a higher level of hydrophobicity in comparison with the flat one. The contact angle for the coated PLLA surfaces is less than the uncoated surfaces because the conformal coating fills the nano-cups and nanocones to a certain extent, decreasing the depth (height) of the nano-cups (nano-cones). The details of wetting behavior are presented in chapter 4.

Drug release measurements

We have established a robust process for measuring the drug released from the PLLA surfaces using HPLC-MS system. HPLC elutes the sirolimus compound into narrow band and MS measures the molecular weight of sirolimus derivatives in the PBS. The molecular weight (MW) of sirolimus (S) is 914. Due to the interaction of mobile phase liquid (methanol) with sodium glass, we can always see a hydrated sodium complex having MW of 952.

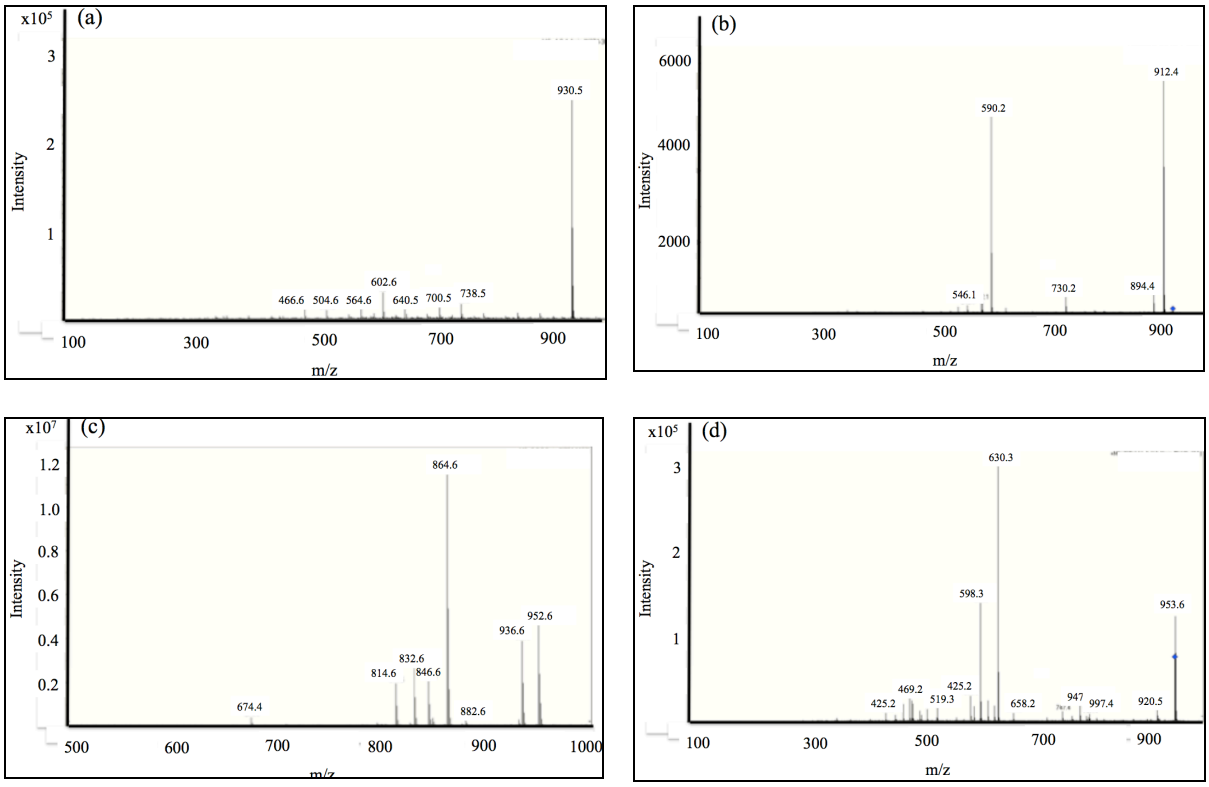

Fig. 5.3 MS/MS breakdown of the sirolimus peak (a) negative ionization mode having peak at 930, (b) MS/MS breakdond the peak at 930 gives its dehydrated version of 912. (c) Positive ionization mode with primary peaks at 952, 936 and 864 and (d) MS/MS breakdown of primary peak 952.

To confirm this we systematically analyzed the MS/MS breakdown of the principle peaks in the negative and positive ionization modes as shown in Fig. 5.5. The primary peak at the negative ionization mode is at the m/z ratio of 930 (Fig. 5.5(a)). This peaks breaks down to 912 (Fig. 5.5(b)), which is sirolimus with loss of two protons. Similarly, one of the primary peaks at the positive ionization mode is 952 (Fig. 5.5(c)). This is hydrated sodium complex and difficult to break. We can see a portion of it attracted a proton to become 953 and has much higher intensity count in comparison to the negative mode as shown in Fig. 5.5(d). We thereby confirm

that the hydrate sodium complex we observe is sirolimus. Also, since the intensity count is much higher for the positive ionization mode, we will use this mode for all our measurements.

The rates of sirolimus release from the flat (control), nano-cone, and nano-cup patterned surfaces have been measured over an ~8-*day* period (see *Experimental Section*) as shown in Fig. 5.6. Very counter-intuitively, the nano-patterned surfaces exhibited markedly slower drug release rates when compared with the flat control, even though they have wider surface areas. In the initial 32-*hour* period, the nano-cup samples exhibited 25~30% lower drug release in comparison to the flat control sample. The drug release from the nano-cone patterned sample was higher than that of the nano-cup patterned one but still lower than that of the flat control. The lower release rate implies that the drug coating has adhered to the nano-patterned surfaces for a longer period of time – a highly desired attribute for coronary stents. Even over longer time periods (2-8 days), the drug release rates of the nano-cup and nano-cone patterned surfaces remained below that of the control by ~20% and 7-10%, respectively.

The most significant result is that the nano-patterned substrates release drugs far more slowly than the flat substrates, as observed in a number of independent experiments. This is counter-intuitive since the drug release rate is expected to increase with the contact area. The periodically patterned surfaces have substantially larger surface area than the flat surface. In our nano-cup (nano-cone) pattern with ~250 *nm* base radius, 150-250 *nm* depth (height), and ~ 700 *nm* pitch, we estimated a 7-20% increase in the surface area. In spite of the large area increase, the observed drug release rates were lower. Such a slower drug release from the patterned materials involving hydrophobic surfaces (e.g. electrospun fiber meshes, nanoporous templates) has also been reported by others [27-29].

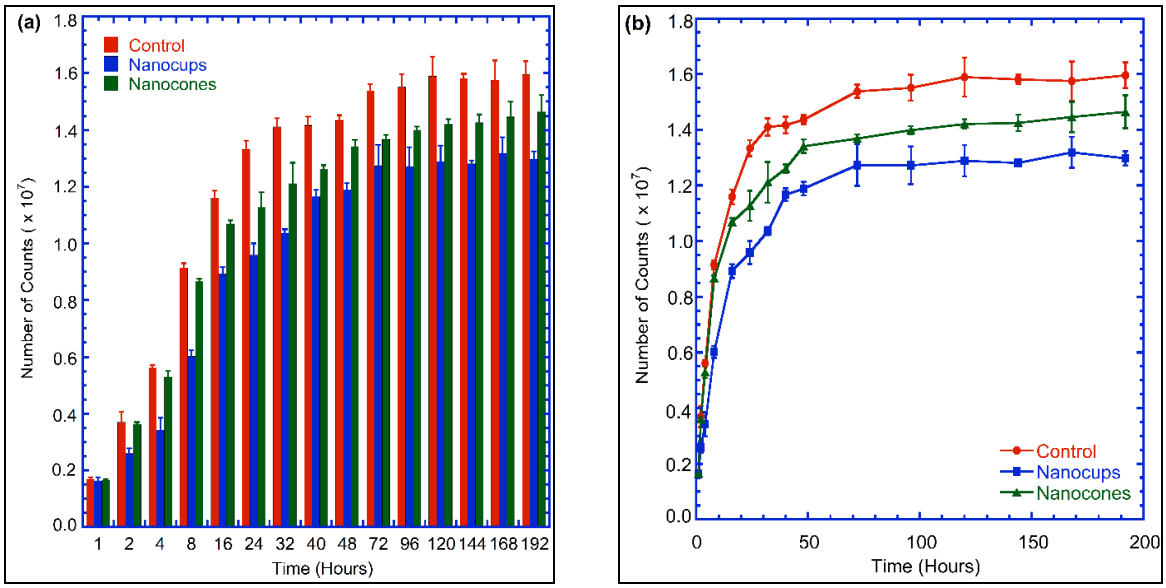

Fig. 5.6 (a) Histogram of HPLC-measured quantities of the sirolimus-derived species as a function of time. The results from the control (flat), nano-cup patterned, and nano-cone patterned surfaces are superimposed to facilitate comparison. (b) The quantity of sirolimus-derived species plotted on a linear scale time axis.

We find that the release rate N_s exhibits an approximate asymptotic power-law behavior of $N_s \sim t^{\alpha}$ at shorter times, with $\alpha \sim 0.63$ (flat) and $\alpha \sim 0.53$ (nano-cup) and $\alpha \sim 0.66$ (nano-cone). This is similar to the square root dependence $N_s \sim \sqrt{t}$ frequently observed in diffusive processes. In accordance, we modeled the release kinetics using the diffusion equation-based model. As is customary, we adopt the separation of variables approach, which leads to the power series solution of the amount of material released. Mathematical modeling of controlled drug release from the plane sheet has been widely reported in literature [30-33]. The release of sirolimus coated on the PLLA surface into the phosphate buffer solution can be thought of as the drug diffusing from a plane sheet into the solution. For our case, the drug is homogenously coated on the PLLA film and there is no physical barrier separating the drug layer and the polymer. It thus constitutes a monolithic system [23]. We solve the Fick's second law of diffusion

$$\frac{\partial N}{\partial t} = D\frac{\partial^2 N}{\partial x^2} \tag{5.1}$$

by separating the space and time variables with appropriate boundary conditions [34].

We can express the total amount of drug (M_t) leaving the film as a fraction of the corresponding amount after infinite time (M_∞) by the power series relation:

$$\frac{M_t}{M_\infty} = 1 - \frac{8}{\pi^2}\sum_{n=0}^{\infty}\frac{1}{(2n+1)^2}\exp\left(-\frac{(2n+1)^2\pi^2}{4L^2}Dt\right), \tag{5.2}$$

where D is the diffusion coefficient and $2L$ is the thickness of the film. It is to be noted that the above mathematical solution for drug release from both the surfaces of the film can be adapted directly for our case where the release is coming only from one surface. This is because for the case of nearly uniform release, the values of M_t and M_∞ will be reduced by the same factor (~0.5) leaving the resultant ratio M_t/M_∞ unchanged.

We fit the experimental data points for the release to the above equation (3) by minimizing the root mean square errors for the experimentally determined PLLA film thickness $L \sim 15$ μm. Equation (3) was solved for the series with $n = 100$ terms, though it was found that the results do not differ for $n > 100$. To determine M_∞, we extrapolated the number of counts for long time periods. The best fit was used to extract the value of D for different patterns – control, nano-cones, and nano-cups. We can see from Fig. 5.7 (a)-(c) that the theoretical fit agrees well with the experimental data, except for the case of nano-cones where a slight deviation from the experimental data is evident. For the best fit, we tabulate the corresponding values of D in Table 5.1. In practice, the diffusive drug release is three-dimensional, which can create considerable

modeling complexity. Since the drug elution is primarily in a single Cartesian direction, the use of one-dimensional diffusion analysis is justified.

Table 5.1: Diffusion coefficients for different pattern types extracted from data fit.

Pattern	**Diffusion Coefficient (D) (10^{-12} cm^2/s)**	**$D_{pattern}/D_{control}$**
Control	3.95	1.00
Nano-cups	2.92	0.74
Nano-cones	3.67	0.93

The fact that the nano-cups exhibits the smallest value of *D* indicates that the release is slowest in the nano-cups among all the three patterned surfaces, even though the surface area has increased after nano-patterning. This is the result of the nano-patterning, which renders it hydrophobic, making it difficult for the solution to wet the PLLA surface. From Table 1, the value of *D* for the control is the highest followed by the nano-cones and nano-cups. Since the diffusion of drug from PLLA into the surrounding solution is proportional to the area of the liquid actually in contact with the patterns, we infer that the liquid is able to wet only a part of the area in nano-cones and nano-cups when compared with the control. We support this incomplete wetting hypothesis by calculating the wetting area in the next section.

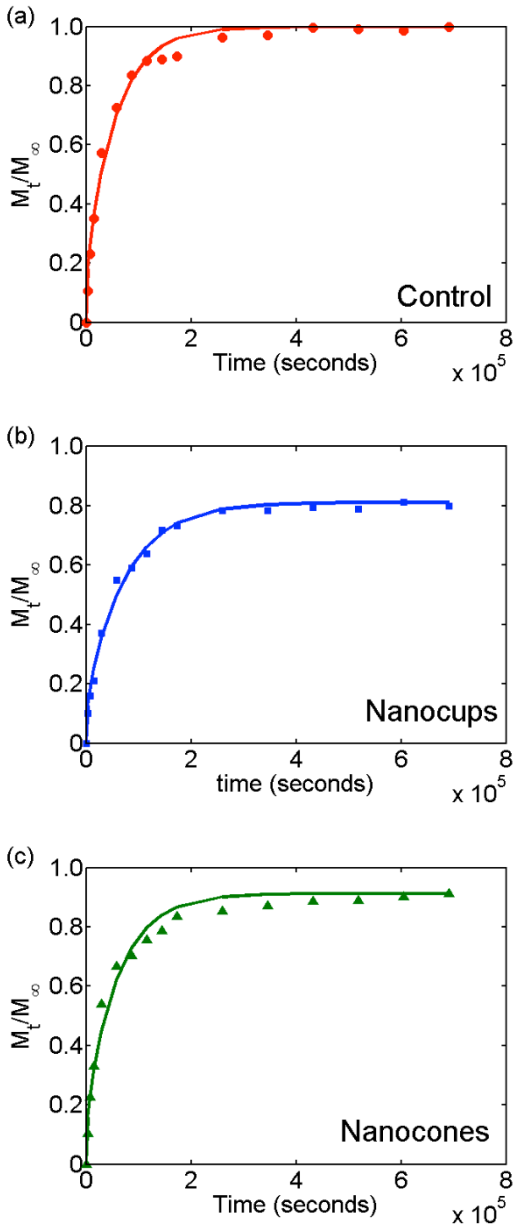

Fig. 5.7 Experimental results fitted to the model and plotted as a function of time for (a) control, (b) nano-cup, and (c) nano-cone arrays.

Incomplete wetting due to nano-patterning

We attribute the slowed drug release from the nano-patterned PLLA surface to the morphologically induced incomplete wetting, which has been observed in a variety of configurations [35]. As the theoretical framework, we have adopted the curvature minimization-

based approach of Berthier *et al*. [36] according to which the area of the nano-patterned, sirolimus-coated PLLA surface in contact with the buffer solution depends strongly on the nano-pattern's cross-sectional shape and the wetting properties of the constituent materials. Through judicious structural design and material selection, the nano-patterned surface can be made not only to impede its total wetting but also to support multiple wetting states, enabling stepwise control of the contact area and drug release rate.

Fig. 5.8 (a) shows the model structure of one individual nano-cup. The grey region represents the sirolimus-covered PLLA with its intrinsic contact angle θ at 77°. We assumed that the nano-cup's cavity was originally filled with air. The radius of curvature (r) and diameter (d) of the nano-cup aperture's edge were set to 100 and 400 nm, respectively, which closely match the fabricated nano-cup geometry. Due to the rounding of the edge with a finite r, the outermost diameter h becomes $h = d + 2r$. From the nano-cup configuration in Figure 5.7, we found two wetting states shown in Fig. 5.8a and 5.8b respectively.

As shown in Figure 5.8(a), the first wetting state sets its three-phase interface on the curved portion of the nano-cup's edge. To find the position (ϕ_1) and radius of curvature (R_1) of the convex meniscus, we modified the formulas in Ref. 35 as:

$$\phi_1 = \theta + \cos^{-1}\frac{r\cdot\sin\theta}{h/2} \tag{5.3}$$

$$R_1 = \frac{\frac{h}{2} - r\cdot\sin\phi_1}{\sin(\phi_1 - \theta)} \tag{5.4}$$

The calculated ϕ_1 and R_1 are 147° and 260 nm, respectively.

The analysis has found another wetting state that has its three-phase interface on the onset of the nanocup's straight edge as shown in Figure 5.8(b). Based on the formula in Ref. 36,

$$R_2 = \frac{d/2}{\sin(\theta - \alpha)} \tag{5.5}$$

where α is the edge slope angle as defined in Figure 5.8(b). We set a to 100° in accordance with the SEM image analysis. The calculated second state radius R_2 is 515 nm at $\phi_2 = \alpha$. Similar nanoscale meniscus formation has been observed in other configurations, such as nanofluidic channels, as well [37].

In either state, the area in contact with the liquid is smaller than that of the flat surface. In the present nano-cup geometry, the contact area for the flat surface is $\pi(h/2)^2 = 0.283\ \mu m^2$. The contact areas for the wetting states 1 and 2, calculated from the torus surface integration, are 0.098 and 0.211 μm^2, which correspond to only 35% and 75% of that of the control, respectively. Such a partial wetting, in turn, would result in a severe reduction in contact area and a markedly lower drug release. Indeed, the experimental observations in previous section indicate that the nano-patterning has resulted in approximately 25-30% lower sirolimus release rates. Such reductions are consistent with the incomplete wetting model. As indicated by Figure 5.8(b), however, even the second state does not lead to a full wetting of the nano-patterned surface. It leads to the possibility of observing un-dissolved *sirolimus* at the bottom of the nano-cup even after a long-term release, which is confirmed by the SEM image in Fig. 5.8(c) taken after 12 days of release. The residual sirolimus also explains why the total amount of drug released from the

two nano-patterned substrates could not converge to that of the control within the observation period.

Owing to the availability of two wetting states, it becomes also probable that the meniscus was originally pinned on the curved edge with its radius at R_1 but moved to R_2 as the result of a certain perturbation, such as the change in the edge shape due to the dissolution of *xi*or mechanical agitation in the liquid body. The resulting increase in the surface area would have increased the sirolimus release rate, causing an abrupt change in the measurement. Although we have not extended the curvature minimization approach to the nano-cone array due to the concerns over its axis-asymmetry, we expect the incomplete wetting would also arise near the waist of the nano-cone where the radius of curvature changes rapidly.

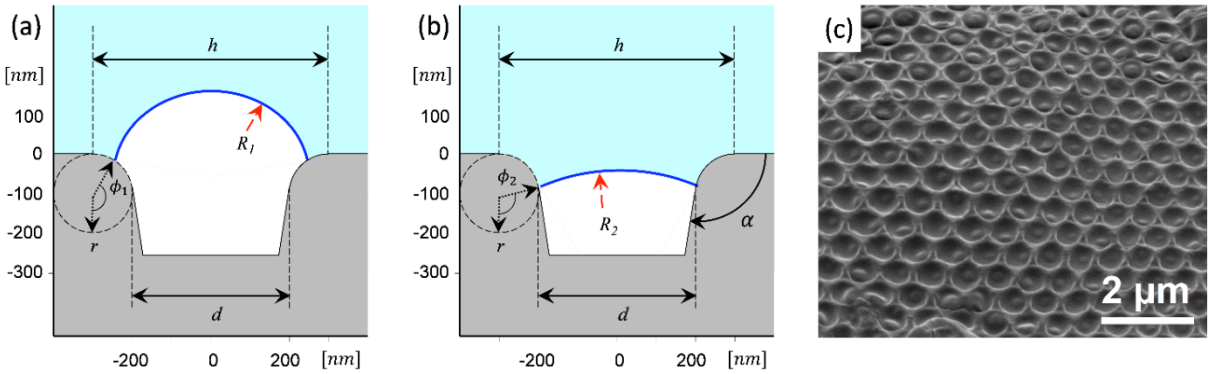

Fig. 5.8 The calculated wetting behaviors of water at the sirolimus-coated PLLA nano-cup structure (r = 100 *nm*, d= 400 *nm*). Two wetting states have been found. The first state (a) is pinned at the round edge with the radius of curvature R_1 at 260 *nm*. The second state (b) is pinned at the starting point of the straight edge with R_2 = 515 *nm*. (c) SEM image of the nano-patterned PLLA surface after 12 *days* of drug release experiment. The image clearly shows the existence of the un-dissolved, residual sirolimus at the bottom of the nano-cups. Scale bar = 2 *μm*.

We quantitatively estimated the drug delivery rate by measuring the depth profile of the sirolimus coated PLLA surfaces with AFM scan. Six sirolimus-coated, nano-cup patterned PLLA samples were placed in the saline buffer solution over time periods up to 10 *days* and then retrieved one by one after 1, 2, 4, 6, 8 and 10 days of immersion. Then the samples were dried and characterized by AFM scans. The gradual release of the drug leads to an increased exposure of the nano-patterned PLLA surface, which, in turn, makes the surface more hydrophobic and further, slows down the release as shown in Fig. 5.9. Figure 5.9(a) shows that the AFM-measured average depth of the nano-cups increases nearly linear with the drug release duration. The AFM scans in Fig. 5.9(b-d) also show that the nano-cup profiles become deeper as the drug release progresses. After the 10-day release experiment the resulting depth of the nano-cup array was 154 *nm*, which is significantly less than that of the uncoated PLLA surface (182 *nm*), indicating the existence of the residual *sirolimus* at the bottom of the nanocup.

We also confirmed that the *sirolimus*-coated patterned PLLA surfaces become more hydrophobic as the drug release progresses, since the nanostructure gets increasingly exposed. For this, we measured the contact angle of a water drop on the nanocup-patterned surface in parallel with the drug-release experiment described above. Each time a *sirolimus*-coated, nanocup-patterned PLLA sample was retrieved from the saline buffer solution, we performed contact angle measurements on it. Figures 5.10(a) and 5.10(b) show that as more *sirolimus* is released, the surface becomes more hydrophobic, with the contact angle starting at 76° and approaching that of the uncoated surface (106°) as shown in Table 5.2. The water droplet picture after 1 day and 10 day release is shown in Figure 5.10(a) and the corresponding change in contact angle over a period of 10 days is plotted in Figure 5.10(b). The plot in Fig. 5.10(b) also indicates that the rate of the contact angle increase begins to saturate from the 8-*day* point. There

is still hydrophobicity in the drug-coated patterned surface at the beginning of the experiment, indicated by larger contact angle, which indeed changes the interaction of drug with the medium and results in different drug release profiles.

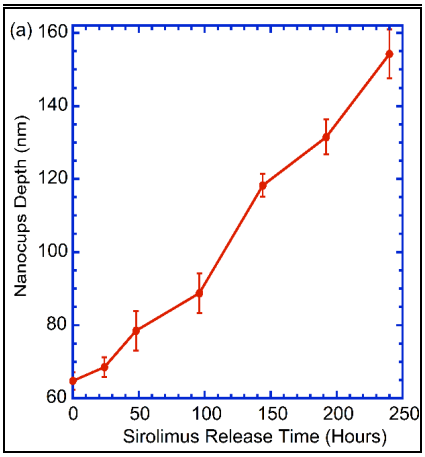

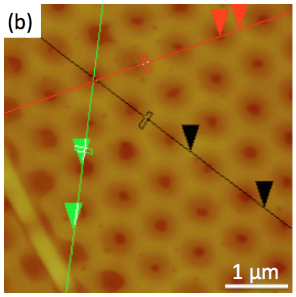

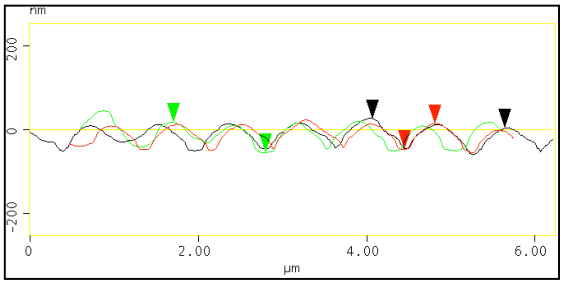

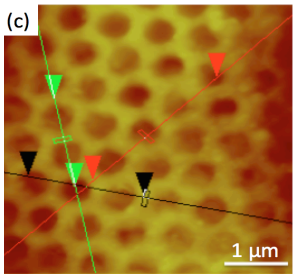

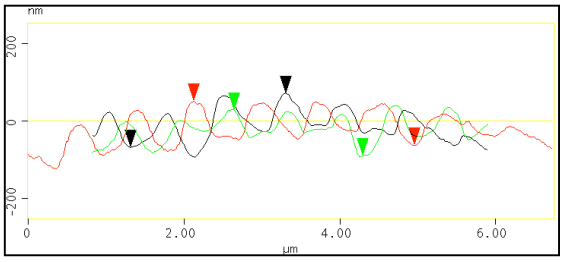

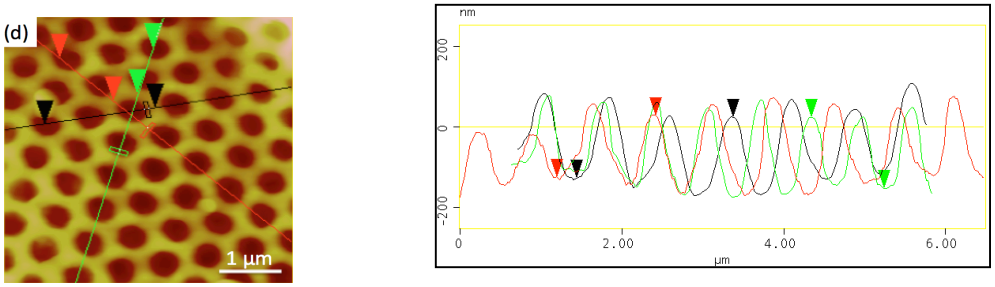

Figure 5.9 (a) The AFM-measured nano-cup depth as a function of the *sirolimus* release time. The AFM images and depth profiles of the *sirolimus*-coated PLLA nano-cups (b) before the release, (c) after 6 days of release, and (d) after 10 *days* of release. The corresponding average depths are 65, 118, and 154 *nm*, respectively. (Scale bars: 1 *µm*)

Table 5.2. Average contact angle for the nano-cup surface coated with sirolimus, as a function of time (in days) during which the drug release measurements were carried out. The patterned substrate was dried after each drug release period and the contact angle for the water drop was measured.

Days	Avg. Contact Angle (degree)
0	76
1	77
2	79
4	83
6	96
8	102
10	104

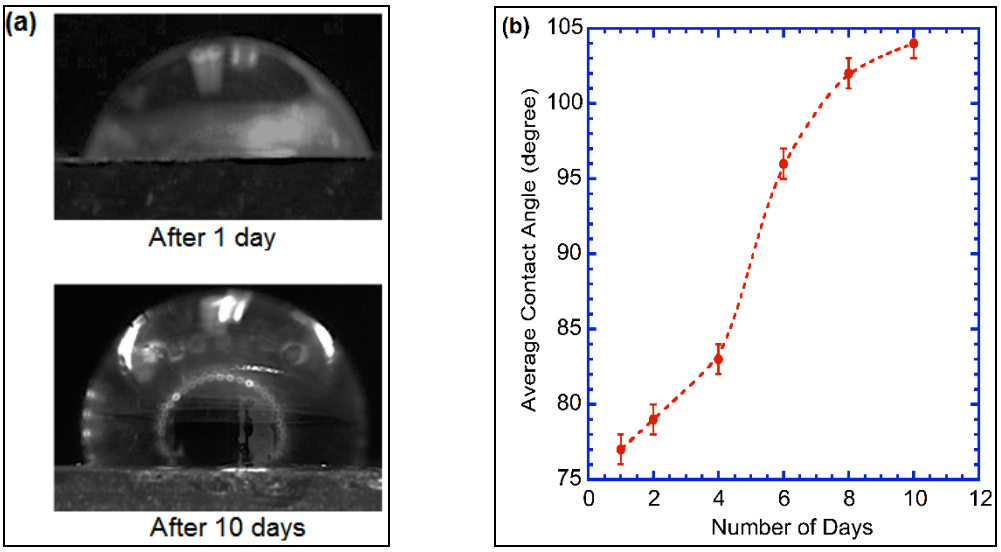

Fig. 5.10 (a) Photograph of water droplet on nanocup patterned surface after 1 and 10 days. (b) Graph of average contact angle versus time in days.

Conclusion

We have measured the rates of drug elution from the nanopatterned PLLA surfaces, prepared by a simple and reproducible technique developed for this work, and compared the results with that of the flat control surface. The nanopatterned surfaces exhibit a 25-30% slower release over a period of eight days when compared with the flat, unpatterned surfaces. The slower release is attributed to the nanopattern-induced incomplete wetting of the PLLA surface. We envisage that the geometry and pitch of the nanostructure can be further controlled to provide more refined tailoring of the drug release rate. These are promising directions for improving the performance of drug-eluting stents in cardiac therapies.

Acknowledgements

This research was supported by the National Science Foundation through Grant CMMI-1265844. We thank Dr. W. Straszheim from the Materials Analysis and Research Laboratory (MARL) of Iowa State University for assistance with scanning electron microscopy. This research used the resources of W.M. Keck Metabolomics Laboratory at Iowa State University. We thank Dr. M. A. Perera from W.M. Keck Metabolomics Laboratory, E. Manna from Ames Laboratory, and members of the Ames Laboratory Photonic Systems group for stimulating discussions.

References

[1] E. P. Childers, M. O. Wang, M. L. Becker, J. P. Fisher, D. Dean, "3D printing of resorbable poly(propylene fumarate) tissue engineering scaffolds," *MRS Bull.*, **40**, 119-126 (2015).

[2] M. J. Choi, K. J. Cha, H. W. Kim, M. H. Na, B. K. Lee, W. Hwang, D. S. Kim, "Microchamber/nanodimple polystyrene surfaces constructing cell aggregates fabricated by thermoset mold-based hot embossing," *Microelectron. Eng.*, **110**, 340-345 (2013).

[3] H. Jeon, H. Hidai, D. J. Hwang, K. E. Healy and C. P. Grigoropoulos, "Effect of micronscale cross patterns on fibroblast migration," *Biomaterials*, **31**, 4286-4295 (2010).

[4] A. Bandyopadhyay, S. Bose and S. Das, "3D printing of biomaterials," *MRS Bulletin*, **40**, 108-115 (2015).

[5] D. A. Lauffenburger, A. F. Horwitz, "Cell migration: a physically integrated molecular process," *Cell*, **84**, 3, 359-369 (1996).

[6] E. E. Bakken and K. Heruth, "Temporal Control of Drugs," *Annals of the New York Academy of Sciences*, vol. 618, pp. 422-427, 1991

[7] K. K. Jain, "Drug Delivery System," in *Methods in Molecular Biology*, vol. 437, J. M. Walker, Ed. Totowa, NJ: Humana Press, 2008

[8] P.Y. Li, "Implantable bioMEMS drug delivery systems," PhD dissertation, University of Southern California, CA (2009).

[9] K. R. Milner and C. A. Siedlecki, "Submicron poly (L-lactic acid) pillars affect fibroblast adhesion and proliferation," *J. Biomed. Mater. Res. A*, **82**, 1, 80-91 (2007).

[10] Y. Zhu, C. Gao, Y. Liu, and J. Shen, "Endothelial cell functions in vitro cultured on poly (L-lactic acid) membranes modified with different methods," *J Biomed. Mater. Res. A*, **69**, 3, 436-443 (2004).

[11] F. Badique, D. R. Stamov, P. M. Davidson, M. Veuillet, G. Reiter, J. N. Freund, C. M. Franz and K. Anselme, "Directing nuclear deformation on micropillared surfaces by substrate geometry and cytoskeleton organization," *Biomaterials*, **34**, 12, 2991-3001 (2013).

[12] P. M. Davidson, H. Özçelik, V. Hasirci, G. Reiter and K. Anselme, "Microstructured Surfaces Cause Severe but Non-Detrimental Deformation of the Cell Nucleus," *Adv. Mater.*, **21**, 35, 3586-3590 (2009).

[13] S. Shi, X. H. Wang, G. Guo, M. Fan, M. J. Huang and Z. Y. Qian, "Preparation and characterization of microporous poly (D, L-lactic acid) film for tissue engineering scaffold," *Int. J Nanomedicine*, **5**, 1049-1055 (2010).

[14] G. E. Rutkowski, C. A. Miller, S. Jeftinija and S. K. Mallapragada, "Synergistic effects of micropatterned biodegradable conduits and Schwann cells on sciatic nerve regeneration," *J. Neural Eng*., **1**, 3, 151-157 (2004).

[15] L. Moroni, and L. P. Lee, "Micropatterned hot-embossed polymeric surfaces influence cell proliferation and alignment," *J. Biomed. Mater. Res. A*, **88**, 3, 644-653 (2009).

[16] G. Vozzi, C. Flaim, A. Ahluwalia and S. Bhatia, "Fabrication of PLGA scaffolds using soft lithography and microsyringe deposition," *Biomaterials*, **24**, 14, 2533-2540 (2003).

[17] S. H. Hsu, C. Y. Chen, P. S. Lu, C. S. Lai and C. J. Chen, "Oriented Schwann cell growth on microgrooved surfaces," *Biotechnol. Bioeng.*, **92**, 5, 579-588 (2005).

[18] U. Sigwar, J. Puel, V. Mirkovitch, et al., "Intravascular stents to prevent occlusion and restenosis after transluminal angioplasty," *N. Engl. J. Med.,* **316**, 701-706 (1987).

[19] P. W. Serruys, P. de Jaegere, F. Kiemeneij, et al., "A comparison of balloon-expandable-stent implantation with balloon angioplasty in patients with coronary artery disease", *N. Engl. J. Med*., **331**, 489-495 (1994).

[20] P. W. Serruys, H. E. Luijten, K. J. Beatt, et al., "Incidence of restenosis after successful coronary angioplasty: a time-related phenomenon: a quanti- tative angiographic study in 342 consecutive patients at 1, 2, 3, and 4 months," *Circulation*, **77**, 361-371 (1988).

[21] T. Kimura, H. Yokoi, Y. Nakagaw, et al., "Three- year follow-up after implantation of metallic coronary-artery stents," *N Engl J Med*., **334**, 561-566 (1996).

[22] H. Tamai, K. Igaki, T. Tsuji, et al., "A biodegradable poly-*l*-lactic acid coronary stent in porcine coronary artery," *J. Interv. Cardiol*., **12**, 443-450 **(**1999).

[23] P. J. Gandhi, Z. V. P. Murthy, "Solubility and crystal Ssize of sirolimus in different organic solvents," *J. Chem. Eng. Data*, **55**, 5050-5054 (2010).

[24] S. Sato, D. Gondo, T. Wada, S. Kanehashi, K. Nagai, "Effects of various liquid organic solvents on solvent-induced crystallization of amorphous poly(lactic acid) film" *J. Appl. Polym. Sci.*, **129**, 1607-1617 (2013).

[25] https://en.wikipedia.org/wiki/Sirolimus

[26] L. R. Snyder, J. J. Kirkland, & J. W. Dolan, (Editors), "Introduction to Modern Liquid Chromatography," Third edition, New Jersey, USA: John Wiley & Sons, Inc. (2010).

[27] H. Xu, H. Li, J. Chang, "Controlled drug release from a polymer matrix by patterned electrospun nanofibers with controllable hydrophobicity," *J. Mater. Chem. B*, **1**, 4182-4188 (2013).

[28] S. T. Yohe, Y. L. Colson, M. W. Grinstaff, "Superhydrophobic Materials for Tunable Drug Release: Using Displacement of Air To Control Delivery Rates," *J. Am. Chem. Soc.*, **134**, 2016-2019 (2012).

[29] K. H. Lo, M. C. Chen, R. M. Ho, H. W. Sung, "Pore-Filling Nanoporous Templates from Degradable Block Copolymers for Nanoscale Drug Delivery," *ACS Nano*, **3**, 2660-2666 (2009).

[30] J. Siepmann, F. Siepmann, "Modeling of diffusion controlled drug delivery," *J. Control. Release*, **161**, 351-362 (2012).

[31] X. Wang, S. S. Venkatraman, F. Y. Boey, J. S. Loo, L. P. Tan, "Controlled release of sirolimus from a multilayered PLGA stent matrix," *Biomaterials*, **27**, 5588-5595 (2006).

[32] F. Alexis, S. S. Venkatraman, S. K. Rath, F. Boey, "In vitro study of release mechanisms of paclitaxel and rapamycin from drug-incorporated biodegradable stent matrices," *J. Control. Release*, **98**, 67-74 (2004).

[33] J. Siepmann, F. Lecomte, R. Bodmeier, "Diffusion-controlled drug delivery systems: calculation of the required composition to achieve desired release profiles," *J. Control. Release*, **60**, 379-389 (1999).

[34] J.-M. Vergnaud, *Controlled Drug Release of Oral Dosage Forms,* CRC Press, Boca Raton, 1993.

[35] E. Martines, K. Seunarine, H. Morgan, N. Gadegaard, C. D. Wilkinson, M. O. Riehle, "Superhydrophobicity and Superhydrophilicity of Regular Nanopatterns," *Nano Lett.*, **5**, 2097-2103 (2005).

[36] J. Berthier, F. Loe-Mie, V. M. Tran, S. Schoumacker, F. Mittler, G. Marchand, N. Sarrut, "On the pinning of interfaces on micropillar edges," *J. Colloid Interface Sci.*, **338**, 296-303 (2009).

[37] P. Kim, H. Y. Kim, J. K. Kim, G. Reiter, K. Y. Suh, "Multi-curvature liquid meniscus in a nanochannel: Evidence of interplay between intermolecular and surface forces," *Lab Chip*, **9**, 3255-3260 (2009).

CHAPTER 6

SUMMARY

I have used the polymer based biomimetic MEMS and micro/nanofabrication techniques to solve four key challenges in optics and biomedicine. For optical applications, I developed novel design and fabrication schemes for thin and flat concentrator and autonomous light level controller fabrication for miniaturization of solar concentrator and direct indoor lighting. Similarly for biomedical application, I designed a novel fabrication scheme to make nano-scale patterns in the PLLA films, which is essential for platform technologies in biomedicine. I finally used this platform to make biodegradable coronary stents for controlled drug delivery application.

First, I developed bio-inspired thin and flat miniaturized solar concentrator (TFSC) design for its potential household applications. Conventional solar concentrators need to track the path of sun daily and seasonally and requires expensive two axis tracking system. This is expensive as well and not convenient for miniaturized design. I took inspiration from wide field of view compound eye of an insect to increase the acceptance angle significantly. I combined the lens and lightguide pair similar as in ommatadium (vision unit of compound eye) and extruded the lens along one direction making it more like cylindrical lens. I optimized the lens F/number, clear aperture, angle of lightguide for maximum angle of solar radiation. The lightguide is curved and joined with a flat bottom plate where the light collected vertically is redirected laterally to make it TFSC. The curved lightguide design is very advantageous to the light redirection elements design we have seen in literature (including metallic reflector, gratings) in increasing the acceptance angle of the design. With judicious choice of lens, lightguide design and Monte

Carlo based simulation I could design 20 cm long solar concentration with total concentration of ~40 and acceptance angle of 15° in azimuthal direction.

As an extension of concentrator design, we took challenge to deliver sunlight directly for indoor illumination. The efficiency of converting sunlight to electricity using PV and back to light using LED is very un-efficient process, with overall efficiency falling to ~4% range. One of the main requirements for this scheme is design of light switch for efficient control of the illumination level. Several actuation methods have been developed in years to design the light switch. We decided the use the energy in solar light as an actuation power source. Solar light consists of more than 50% of energy in IR region. We used this energy to heat the phase change material paraffin wax and produce a actuation stroke in MEMS design. We employed novel design of the light switch employing one fixed and one flexible cantilever lightguides. The flexible lightguide make of PET when actuated by paraffin collapse to the main lightguide and frustrated the light guided by TIR. Thus a portion of light is leaked into the flexible lightguide. We used closed loop control scheme whereby the MEMS is biased for a fixed illumination and light switch controls the illumination level with increase or decrease in total incident light.

The third challenge we took was nano-scale fabrication of PLLA film for application biomedicine and bioengineering. Nano and micro scale patterning of bio polymers like PLLA creates the templates at its surface and is crucial in creating and controlling a defined cell growth microenvironments, controlled drug release and implantable devices in human medicine. There exists several nanofabrication technology employing advanced lithography techniques and have been used by different research groups. We designed rapid, inexpensive and highly reproducible nano-patterning techniques using replica-molding techniques. We used commercially available polycarbonate master patterns to pattern PDMS mold at first and replicated the PDMS mold into

PLLA thin films. We developed two techniques, drop casting and nano-imprinting to make the nano-scale patterns. We saw high fidelity replication patterns by the drop casting process preserving the pitch, diameter and depth/profile of nano-cups and cones preserved completely. The nano-patterning change the surface properties of the PLLA film from hydrophilic to hydrophobic. We used contact angle measurement to verify this and observed that nano-patterned PLLA film have contact angle of 108° in comparison to 77° for flat control. We also developed efficient drug coating process on these nano-patterned films using brush-coating techniques. We got shallow and yet very conformal drug coating on the PLLA surface.

Finally, as an extension of this nano-patterning PLLA work, we studied the controlled drug release for potential application in drug eluting stents. The nano-patterned PLLA film we developed can be easily rolled into a tubular structure making it ideal design for biodegradable stents. Main function of stent is to provide mechanical support in opening the artery during angioplasty. Usually the side effects of this invasion are stenosis (closure of artery) within 4-6 months, blood clotting (thrombosis), excessive fibrous tissue accumulation (fibrosis). Immunosuppressant drugs like sirolimus is used to prevent this and the dissolving drug eluting stents is an ideal choice. The nano-patterned PLLA surface on the stents gives us better flexibility in designing the controlled drug release kinetics for maximum therapeutic efficacy. We loaded our nano patterns and control with same amount of drug and released the drug in phosphate buffer saline for 10 days. We then analyzed the samples collected at the predetermined time using HPLC-MS system to determine the amount of drug released. We found that, despite of increase of overall function surface area, the patterned surface release the drug 25-30% slower in comparison to control.